Transfer-free Fabrication and Assessment of Transparent Multilayer CVD Graphene MEAs for in-vitro Optogenetic Studies

Master of Science in Biomedical Engineering
February 2024

Gonzalo León González

Delft University of Technology

TU Delft

Transfer-free Fabrication and Assessment of Transparent Multilayer CVD Graphene MEAs for in-vitro Optogenetic Studies

by

Gonzalo León González

to obtain the degree of Master of Science in
Biomedical Engineering

at Delft University of Technology,
to be defenced publicly on Thursday, February 29, 2024 at 10:30 AM.

Student Number:	5634768	
Project Duration:	September, 2022 - February, 2023	
Thesis committee:	Dr. Vasiliki Giagka,	TU Delft, supervisor
	Dr. ir. Sten Vollebregt,	TU Delft, supervisor
	Dr. Massimo Mastrangeli,	TU Delft
	Angelo Accardo,	TU Delft

TU Delft

Abstract

Electronic interfaces, particularly microelectrode arrays (MEAs), are crucial for studying electrophysiological processes in the body, with applications ranging from implants to deep brain simulators. In neuroscience, they play a vital role in exploring neuronal cell distribution and behaviour, as well as disorders like epilepsy and Alzheimer's disease. However, electrophysiological recordings have limitations, that have led to the exploration of optical approaches like calcium imaging. To address the shortcomings, a promising strategy involves integrating electrophysiology and optical methods for simultaneous cellular activity measurement, capitalising on their combined temporal and spatial resolution. The challenge lies in developing fully transparent MEAs to overcome the limitations of traditional opaque electrodes.

Graphene's versatile properties, spanning from electrical conductivity to mechanical flexibility, position it as an ideal material for transparent and flexible electronics, particularly in neural recording and stimulation. Due to these properties, graphene MEAs (gMEAs) allow integration with various optical techniques, overcoming limitations associated with traditional opaque MEAs.

In this project, we designed and fabricated a transparent gMEA, intended to perform electrical signal recordings and optical voltage mappings simultaneously from photostimulated optogenetic cell lines. The design allows for photostimulation from a source beneath the gMEA, while enabling unobstructed optical measurements from above. The electrodes were crafted from multilayer chemical vapour deposition (CVD) graphene, chosen for its transparency and favourable electrical properties. Quartz and sapphire were evaluated as potential substrates for the device. After demonstrating the synthesis of multilayer graphene was possible on both substrates, quartz was selected as the preferred material due to its resistance to graphene delamination.

Characterisation of the gMEAs was done using various techniques, including optical transmittance (OT), electrochemical impedance spectroscopy (EIS), and measurements of the signal-to-noise ratio (SNR). The stability of the gMEAs was also assessed by immersing the devices in cell culture medium and with ageing tests performed in PBS. Initial electrochemical characterisation of the gMEAs exhibited promising signal detection despite a relatively high baseline noise of $\sim$ 23 μV. In comparison, commercially available MultiChannel Systems MEA (60MEA200/30iR-Ti), showed a lower baseline noise ($\sim$ 4 μV), but gMEAs achieved comparable signal sensitivity. EIS of gMEAs revealed an impedance at 1 kHz ranging from 3.2 to 9.89 $M\Omega$, largely surpassing values in other studies. However, when area normalised, the impedance remained comparable to reported values. Stability tests identified issues related to the permeability of the encapsulation layer and degradation of molybdenum structures, causing large variations in the SNR and EIS measurements after exposure to liquid media.

Acknowledgements

First, I would like to extend my special thanks to Vasso and Sten, for guiding me through my master's project, answering my questions and helping me reach my objectives. This project has not been short of issues and I really appreciate your help in finding ways around the obstacles. I am so grateful to have had such knowledgeable and passionate supervisors in my project, thank you.

Special recognition goes to Shanliang and Gandhi for your patience in addressing my numerous questions and consistently providing answers and advice. Not to forget the EKL staff for your unwavering support and teachings that surpassed my expectations. I am particularly grateful to Hande, Francesco, Paolo, and Daniel, whose kindness and willingness to help have been instrumental in my journey. To the staff at the Laboratory of Experimental Cardiology of Leiden University Medical Center, including Shangliang, for performing the soaking test and the cell culture, for your guidance and for allowing me to use your setup to carry out electrical recordings. And to the Bioelectronics group, thank you for fostering a supportive environment that made our office feel like a second home.

I would also like to praise my dear friend and all-time favourite advisor for all sorts of projects, Doctor Jaime Lazúen, whose encouragement, guidance, and willingness to entertain even my wildest ideas have been invaluable throughout this journey.

I am deeply appreciative of the staunch support of my friends, in Delft and miles away. Eduardo and Ramon, in particular, have been constant companions, engaging in countless brainstorming sessions and uplifting me during challenging times. And to 'Party at Jumbo' for soothing rough times with good laughs. Thank you to all of you for being there for me.

Last but not least, I want to express my gratitude to my family for always being there for me and supporting me through the highs and lows of life. Thank you for believing in me and always encouraging me to reach higher. There are not enough words to express my gratitude and I hope to make you as proud as you make me happy. I would not have been able to do it without you.

This past year and a half has been a journey filled with experiences, challenges, and achievements, and I am deeply grateful to all those who have played a significant role in shaping my growth, both academically and personally.

Gonzalo León González
Delft, February 2024

Contents

List of Figures

List of Tables

1 Introduction

Electronic interfaces serve as essential tools in investigating electrophysiological processes taking place across the body (in-vitro and in-vivo), particularly for electrogenic cells. Microelectrode arrays (MEAs), a common form of this technology, facilitate the high temporal resolution recording of cell activity and the electric stimulation of cells [1–3]. Some applications of this technology include cochlear and retinal implants, pacemakers, and deep brain stimulators. It is widely used in the field of neuroscience for studying the distribution and behaviour of neuronal cells, and neurological disorders such as epilepsy and Alzheimer's disease [3, 4]. Nonetheless, electrophysiological recordings are limited to discrete regions of neurons [5].

An alternative approach is the use of optical means, such as calcium imaging, to measure cellular activity over a larger number of cells. Yet, this method lacks the necessary temporal resolution for capturing fast processes. To overcome this limitation, a promising strategy involves integrating electrophysiology and optical methods into platforms to simultaneously measure cellular activity. This synergistic approach capitalises on the high temporal and spatial resolution offered by combining both procedures. Despite its potential, traditional MEAs with opaque electrodes cannot be used as they limit the field of view and generate optical shadows. Thus, the challenge lies in the development of completely transparent MEAs for these applications [3, 5, 6].

1.1. Optogenetics

Optogenetics is an innovative method that combines optics and genetics to precisely control cell behaviour. This technique allows for the stimulation or inhibition of cells, activation of genes, modulation of intracellular signalling, and influence of cell migration [7, 8]. Central to optogenetics for stimulation and inhibition, is the genetic modification of cells for the expression of opsins, which are light-sensitive ion channels. Among the various opsins, Channelrhodopsin-2 (ChR2) is frequently used and enables the activation of neural and muscle cells with high temporal precision, through its activation by blue light (wavelengths between 440-500 nm). Conversely, Halorhodopsin (HpHR), another type of opsin activated by yellow light (wavelengths $\sim$ 570 nm), can silence active cells and offers a way to exert bidirectional control over cellular activity when expressed alongside ChR2 [7, 9]. Figure 1.1 depicts a simple diagram illustrating the method for optogenetic stimulation.

The selective expression of opsins allows for targeted stimulation or inhibition of cells, ensuring that only genetically modified cells are affected, thereby achieving high cellular specificity combined with the high temporal resolution of this technique. Furthermore, due to the nature of photostimulation, a large spatial resolution for the activation of cells can be achieved. In comparison, traditional electrical stimulation is not cell-specific, affecting all cells in a targeted area indiscriminately, and requires a high density of electrodes to achieve high spatial resolutions [7, 8].

Optogenetics is emerging as a revolutionary tool in research and therapeutic applications, offering significant benefits over traditional stimulation methods. For example, optogenetic technologies have gained importance in the field of neurobiology research, particularly in the study of the distribution and function of different types of neuronal cells [7, 8]. Depending on the requirements of each application different approaches may be taken to stimulate the cells ranging from optrode arrays integrated within

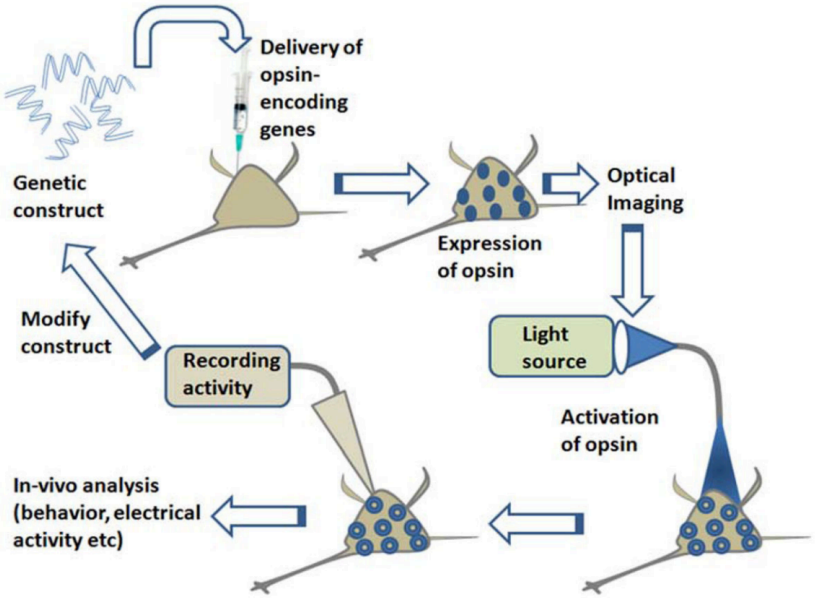

Figure 1.1: Diagram depicting optogenetic stimulation approach. From [7].

MEAs for in-vitro applications or in neural probes for in-vivo applications [7, 9, 10].

1.2. Optical Bioimaging Techniques

Optical monitoring methods for capturing cellular activity, especially action potentials, offer significant advantages over traditional electrophysiological techniques such as MEAs [7, 11]. As discussed earlier, MEAs require a high electrode density to achieve high spatial resolutions. This is often accompanied by a reduction in the electrode size, typically causing larger impedances, which can reduce their sensitivity and signal quality [11, 12]. Optical approaches, in contrast, attain high-throughput monitoring of cellular activity across large populations of cells simultaneously. These methods take advantage of the sensitivity and specificity of light-sensitive proteins and fluorescent indicators to monitor cellular events, enabling detailed assessment of neural and muscle cell activity and behaviour with minimal perturbation to the cells [7, 13].

Among the various optical methods for monitoring cellular activity, voltage-sensitive dyes (VSDs) are particularly notable for their versatility and wide applicability. VSDs, which include a diverse array of organic molecules and proteins, respond to changes in voltage or ionic movements across cell membranes by altering their optical properties. This change often causes the emission of fluorescent light with a good temporal resolution that enables cellular activity detection with minimal delay ($< 10\mu s$). A common use of VSDs is in calcium imaging, where calcium-sensitive VSDs (e.g., Ca-orange) detect fluctuations in intracellular Ca^{2+} concentrations [7, 14]. However, VSDs are not without drawbacks, such as potential phototoxicity and background interference. As an alternative, genetically encoded voltage indicators (GEVIs) offer a less cytotoxic option by genetically modifying cells to express protein sensors, thereby achieving high cell specificity. An example of this is GCaMP, a genetically encoded calcium indicator [7, 15]. Other markers, including fluorescent biosensors and bioluminescence enzymes, such as green fluorescent protein (GFP) and luciferases, respectively, allow the detection of additional biochemical events that may be used to monitor cell activity [16, 17]. Alternatively, label-free imaging represents an emerging field that seeks to eliminate the need for dyes or genetic voltage/ion indicators altogether. Techniques such as phase-sensitive optical coherence tomography (PSFD-OCT) are being explored to achieve this goal [7, 18, 19].

The detection of fluorescent signals requires the use of microscopy techniques that enhance the contrast, resolution and specificity of fluorescent signals. Some examples include confocal and two-photon microscopy, although the choice of recording method varies based on the types of specimens and the research objectives. These methods are highly reliant on the unobstructed view of the cells, either from above or below, and as such require the use of transparent substrates. An example of this

is with total internal reflection fluorescence microscopy, which illuminates the sample through the substrate [20]. The fluorescent signal is optically recorded with highly sensitive sub-millisecond temporal resolutions, often requiring CCD cameras [14].

1.3. Transparent Electronics

Transparent electronics represent a growing field, particularly in the biomedical sector and for display technologies [21, 22]. The integration of transparent electronic devices with optical technologies, such as optogenetics and fluorescent indicators, presents a significant advantage, allowing researchers to manipulate and monitor cellular processes in real time with a clear visual of the cells being studied. This compatibility enables the combination of electrophysiological and optical assessment techniques simultaneously, a very useful tool for the study of neural and muscular function, disease progression, and response to therapies, among others [11, 23].

The field of transparent electronics is populated with a variety of materials and components, each contributing unique properties to the field. Transparent conductive oxides (TCOs) like indium tin oxide (ITO) are widely used for their excellent conductivity and high optical transparency, serving as the foundation for many transparent electronic devices. Conductive polymers, carbon-based materials (e.g., carbon nanotubes and graphene), and ultra-thin metal films also play significant roles, offering flexibility and stretchability that TCOs lack. However, these materials come with trade-offs. For instance, while conductive polymers and graphene provide flexibility, their conductivity might not match that of traditional metallic conductors. Similarly, issues such as long-term durability and integration into complex electronic systems continue posing challenges [11, 21, 22].

1.4. Objectives of the Project

This chapter introduces innovative optical stimulation and recording methodologies for cell electrophysiology research, highlighting their advantages over traditional MEAs in terms of spatial resolution and specificity. A growing trend is the development of optically compatible, transparent MEAs, achieved by substituting opaque conductors with transparent alternatives. This advancement seeks to facilitate cell stimulation through optogenetics while enabling concurrent electrophysiological recording using both electrical and optical methods, thereby leveraging the strengths of each approach.

The objective of this thesis is to design, fabricate, and characterise a transparent MEA for in-vitro experiments. This array should be compatible with optogenetic stimulation and optical bioimaging techniques, allowing for simultaneous electrophysiological recordings. Building upon previous research, the MEA will use multilayer CVD graphene, produced using a transfer-free method, as the electrode material [24]. To achieve this, the thesis will address several research questions: Can high-quality multilayer CVD graphene be synthesised on transparent substrates using the transfer-free approach? And, is this type of transfer-free graphene biocompatible?

The project will adapt the MEA to fit the setup at the Laboratory of Experimental Cardiology of Leiden University Medical Center (LUMC). This setup includes a MultiChannel Systems (MCS) amplifier for electrophysiological recordings and a SciMedia optical voltage mapping system for optical recordings, that illuminates the sample from above while optogenetically stimulating from below. The project will proceed through the following phases:

1. Synthesis and characterisation of graphene on transparent substrates.
2. Design of the MEA.
3. Development of a process flow for fabricating the transparent MEA.
4. Microfabrication of the MEA.
5. Characterisation of the MEA's electrochemical properties and stability assessment.
6. Evaluation of the MEA's biocompatibility, optogenetic compatibility, and recording efficacy using optogenetic cardiomyocyte cell lines in-vitro.

1.5. Outline of the Report

This thesis is structured into six chapters, including this introductory chapter. Chapter 2 delves into a comprehensive literature review, scrutinising the latest advancements and trends in MEA, the unique

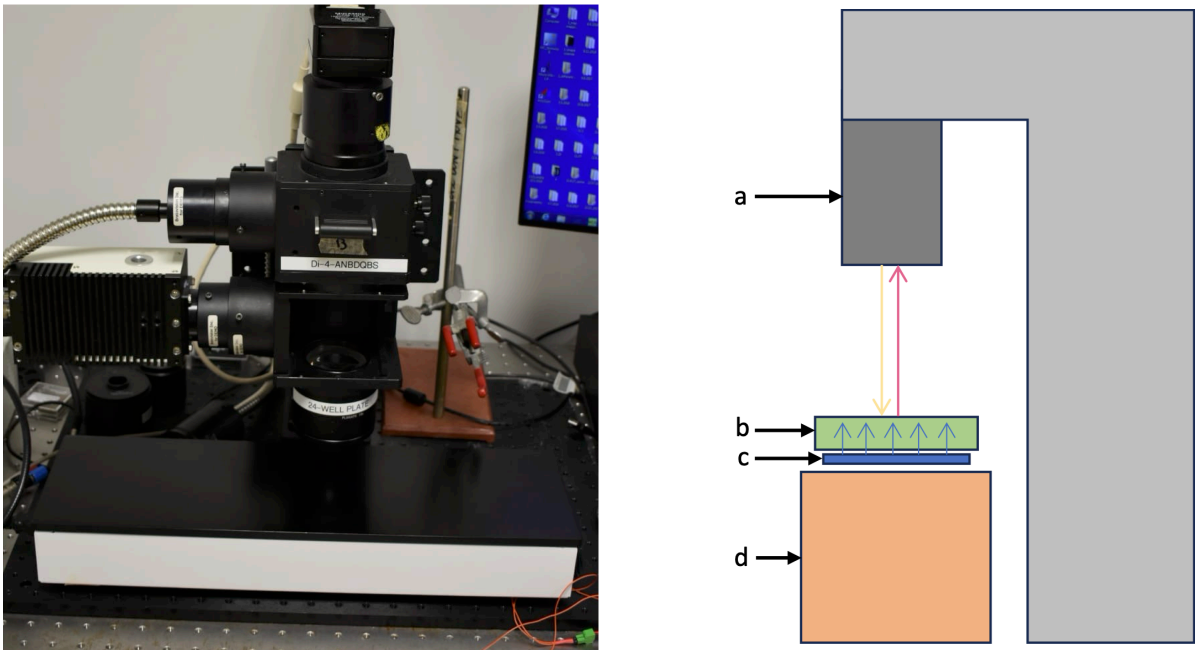

Figure 1.2: LUMC setup for simultaneous electrophysiology recordings and optical voltage mapping during optogenetic stimulation. **Left**: SciMEdia optical voltage mapping system with hot plate. **Right**: Diagram of LUMC setup with: **a**) Optical voltage mapping system. MEA is illuminated at a specific wavelength to activate optical dye and dye fluorescence is detected back. **b**) MCS amplifier with transparent MEA mounted in it (not visible in the diagram). **c**) Micro-LED array for optogenetic cell stimulation. Light emitted from the micro-LED array will go through the MEA substrate to reach the cells. **d**) Hot plate used to maintain the cell cultures at 37ºC during voltage mapping.

properties and potential applications of graphene, and the characterisation of recording electrodes via electrochemical impedance spectroscopy (EIS), stability evaluations, and signal-to-noise ratio (SNR) assessments. Chapter 3 focuses on the meticulous design and fabrication processes of the graphene MEA (gMEA), with an emphasis on material selection to optimise performance.

Chapter 4 details the methodologies employed for characterising the gMEA devices. This includes the procedure for selecting the optimal substrate for the gMEA, as well as the assessment of electrochemical, stability, and biocompatibility properties, which are crucial for the device's intended applications. The chapter also outlines the general experimental procedures undertaken during the characterisation process.

The findings from both the graphene and device characterisations are thoroughly analysed and discussed in Chapter 5. Finally, building on these insights, Chapter 6 draws a series of conclusions from the study, proposes future research aimed at enhancing the project's outcomes, and offers a compilation of practical recommendations to guide subsequent work.

2

Literature Review

Chapter 2 offers an in-depth literature review, exploring recent developments and emerging trends in the field of MEAs. It examines the distinctive qualities and possible uses of graphene, along with methods for analysing recording electrodes, including EIS, stability evaluations, and SNR assessments.

2.1. Microelectrode Arrays

MEAs are devices capable of electrically stimulating and recording the bioelectric activity of muscle and neural cells, both in-vitro and in-vivo [Fig. 2.1 (L.A)]. These devices find application in a range of clinical and research settings, including drug development, diagnostics, and the creation of simplified organ models [25–27].

Constructed using microfabrication technology, MEAs comprise three key components: a base layer that serves as the foundation for the device, a patterned conductive layer that transduces bioelectric signals from cells into electrical signals (and vice versa), and an insulating layer that protects the conductive structures while also defining the electrode dimensions [25, 26].

The choice of materials for MEA construction varies according to specific requirements. Traditionally, rigid materials have been preferred for the base layer; however, there is a growing shift towards flexible materials like parylene, polyimide, polydimethylsiloxane (PDMS), and hydrogels. These materials better match the mechanical properties of tissues and can conform to their topology. While gold (Au), platinum (Pt), indium tin oxide (ITO), and titanium nitride (TiN) remain standard choices for the conductive layer, emerging non-metallic materials, such as graphene, are showing promise, offering improved signal detection and stimulation precision. This is critical, as traditional metals sometimes fall short in these areas. Insulation has traditionally been provided by materials such as silicon-dioxide (SiO_2) and silicon nitride (Si_3N_4), but recent trends lean towards polymers like SU-8, PDMS, parylene, and polyurethane, highlighting an ongoing innovation in insulation materials [25–27].

To enhance microelectrode performance, one approach under exploration is nanomaterial surface modification. This technique involves altering the electrode surfaces with nanomaterials to improve their bioelectric sensing and stimulation capabilities, while also reducing the foreign body response. Although promising, this method has been challenged by issues of repeatability. Various nanomaterials, including organic polymers (such as conducting polymer coatings like PEDOT:PSS), metal materials (nanoscale metal features, e.g., Au and Pt), inorganic non-metallic materials (primarily carbon-based materials like carbon nanofibers (CNFs), carbon nanotubes (CNTs), and graphene), and nanocomposite materials, have been employed. However, not all nanomaterials have proven equally effective, with concerns over fragility, wear, and cytotoxicity in some cases. To date, modifications using carbon-based nanomaterials, particularly CNTs and graphene, have demonstrated superior performance and have become the benchmark for certain MEA applications [25, 26].

The second approach to enhancing MEAs involves the creation of 3D structured micro-electrodes. These structures are designed to form more efficient electrical interfaces with cells, thereby improving signal detection sensitivity. The capability of these structures to be engulfed by cells allows for the detection of both intracellular and extracellular signals. A notable innovation in this area is the development of mushroom-shaped Au microelectrodes [28], which have been particularly successful.

Additionally, the integration of structures such as nanotubes into these electrodes has been explored for applications in drug delivery and chemical stimulation [25, 26, 29].

MEAs have achieved remarkable advancements, including high densities of microelectrodes (over 3000 electrodes per mm^2), the resolution to detect single cell action potentials, and microelectrode diameters ranging from a few to tens of micrometres [25, 26, 30]. A significant trend in MEA development is the integration with microfluidic devices to establish neural chip platforms, or ”organs on a chip” [Fig. 2.1 (L)]. This innovation addresses the challenge of replicating the complex architecture of neural networks found in the brain, which is difficult to achieve with in vitro neuron cultures on traditional MEAs. By growing neurons on microfluidic devices, researchers can mimic the brain’s neural architectures more accurately, facilitating studies on neural networks and their structure-function relationships without the need for in vivo experiments [25, 30–32].

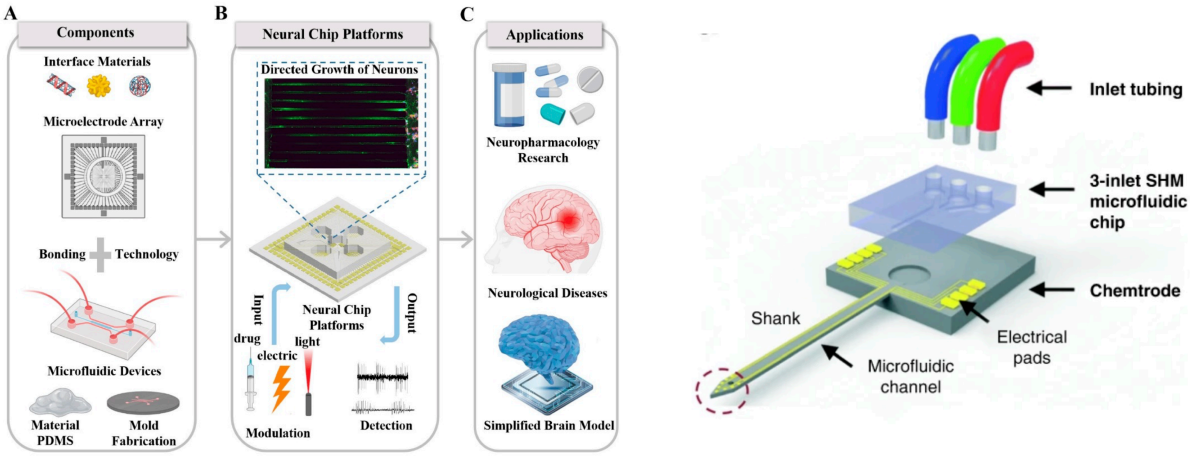

Figure 2.1: Microelectrode arrays reported in literature. **Left**: Diagram depicting the fabrication, usage and applications of neural chip platforms. From [25]. **Right**: Schematic of a multifunctional neural probe with integrated microfluidic chips. From [33].

In parallel, neural probes are also being utilised to study the neural networks in ex-vivo and in-vivo experiments. They have traditionally consisted of electrodes, sometimes with other structures such as drug delivery systems, mounted on rigid probes and inserted in tissues to record and stimulate the surrounding cells [Fig. 2.1 (R)]. Recently, a transition from rigid to soft substrates has emerged. This change enhances tissue integration, minimises damage and inflammatory responses, and supports the long-term recording of stable neural signals [34].

Another trend is the shift from electrical to photostimulation. The miniaturisation of microelectrodes increases impedance, which, combined with the need to reduce charge injection limits, can lead to damaging Faradaic reactions to the electrode and adjacent tissue. Electrical stimulation, being non-selective, affects all surrounding tissue, limiting its use in long-term applications. Photostimulation, however, offers a promising alternative, enabling high spatial resolution and selectivity. Techniques such as optogenetics, and direct and indirect photothermal stimulation, alongside optical recording methods like calcium- and voltage-sensitive imaging, demonstrate the potential of light-based stimulation and recording [27, 34].

The implementation of these techniques often requires transparent devices. For MEAs, materials such as glass or transparent polymers (e.g., PDMS, SU-8) for substrates, and ITO or ZnO for conductive layers have been standard, although innovations like gold mesh electrodes and alternative flexible, transparent materials (e.g., CNTs, silver nano-wires, graphene) are being explored [35]. These developments not only allow for optogenetic stimulation and observation of cell growth but also accommodate the integration of light delivery systems, such as optical fibre, in neural probes, further expanding the possibilities for research and clinical applications [25–27, 34].

2.2. Graphene

2.2.1. Characteristics and Types

Graphene is a carbon allotrope in the form of a one-atom thick 2D crystal lattice, equivalent to a single layer of graphite. Each carbon atom is sp^2 hybridised to three of its neighbours in a plane, through a covalent (σ) bond. This configuration results in a hexagonal pattern that is both strong and flexible. A schematic of the graphene structure is depicted in figure 2.2. The fourth electron of each carbon atom remains free in a p-orbital, perpendicular to the plane, which contributes to the formation of π bonds. These bonds create delocalised electrons that move freely across the graphene sheet, giving graphene its exceptional electrical conductivity. In the context of multilayer graphene, the layers are held together by van der Waals forces. This multilayered structure, while still strong, has different properties from the single-layer graphene due to the interactions between the layers.[36–39].

The distinctive structure of graphene imparts it with a series of exceptional properties. The σ bonds provide the lattice with significant strength, evidenced by a Young's modulus $\sim$ 1 TPa [38, 40]. Its half-filled π band, populated with delocalised electrons, accounts for the material's remarkably high thermal conductivity, $\sim$ 5000 $Wm^{-1}K^{-1}$ at room temperature, and superior charge carrier mobility, reaching up to 200,000 $cm^2V^{-1}s^{-1}$ in freely suspended forms [37–40]. Graphene is not only flexible, capable of bending and returning to its original shape without losing electrical properties, but it also demonstrates high optical transmittance (OT), absorbing $\sim$ 2.3% of visible light, alongside a theorised high surface area of $\sim$ 2630 m^2g^{-1}. However, these properties can be influenced by the material's quality, the production method employed, and the specific arrangement and number of graphene layers [37, 38].

Graphene's adaptability is showcased in its various forms, each with distinct compositions, layer counts, and sizes. Graphene oxide (GO), for example, is notable for its hydrophilic nature and lower electrical conductivity [41], while the electrical properties of reduced graphene oxide (rGO) can approximate those of pristine graphene, contingent on the residual oxygen content post-reduction [42]. The number of graphene layers also significantly impacts its properties; as graphene transitions from monolayer to multilayer forms, its electronic structure and hence its properties evolve. For example, multilayer graphene exhibits a higher electrochemical capacitance alongside a lower sheet resistance and OT, compared to its monolayer form [40, 43]. Additionally, the size of graphene pieces, ranging from nanoparticles to centimetre-scale sheets, influences their specific properties, with edge effects and surface area to volume ratios playing significant roles in defining their characteristics and suitability for various applications [40].

2.2.2. Graphene Fabrication

Graphene fabrication techniques fall into two primary categories: top-down and bottom-up methods [Fig. 2.2]. The top-down method involves separating layers from graphite or graphite derivatives to produce graphene or modified graphene layers. This category includes well-known processes like exfoliation, which itself comes in various forms such as micromechanical, electrochemical, and solvent-based methods. Conversely, bottom-up approaches synthesise graphene layers directly from carbon-based precursors, with Chemical Vapour Deposition (CVD) and epitaxial growth on silicon carbide SiC being the most significant.

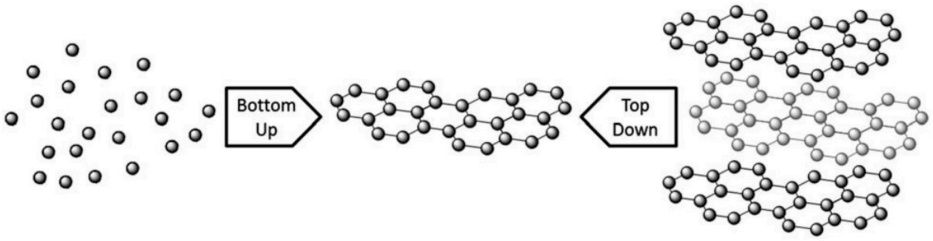

Figure 2.2: Schematic representation of the approaches for graphene synthesis. From [38].

Top-Down Approaches

Exfoliation, as noted, is a prevalent method for isolating individual graphene layers from graphite. This technique was famously employed by Novoselov and colleagues in 2004 [44] to first isolate graphene,

using adhesive tape for micromechanical cleavage of graphite layers. This method is known for yielding high-quality mono, bi-, and few-layer graphene, though its labour-intensive nature limits its scalability for commercial production [36–38]. Electrochemical exfoliation offers an alternative by using graphite as a sacrificial electrode in an electrolyte solution, often with a surfactant added to prevent the re-agglomeration of graphene sheets, and in some cases assisted by sonication. This approach can produce graphene flakes of varying thicknesses, with isolation of few-layer graphene possible through centrifugation. However, the challenge lies in the removal of surfactants, which can adversely affect graphene's electrical properties [37, 38, 45].

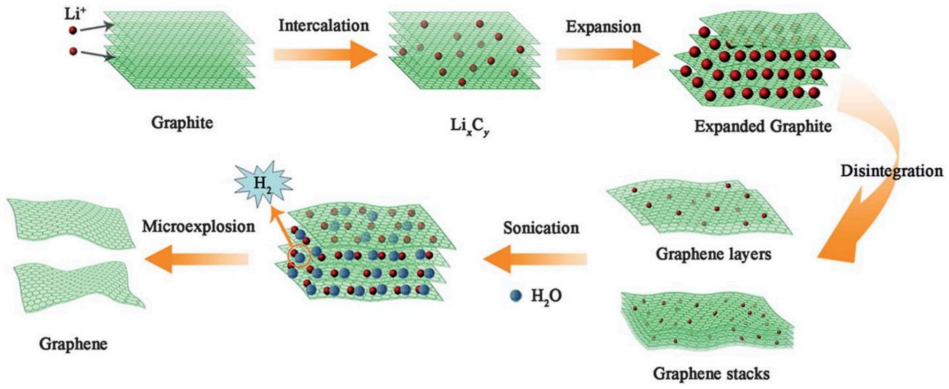

Figure 2.3: Diagram depicting exfoliation of graphite into graphene sheets using intercalation compounds. From [45].

Solvent-based exfoliation leverages specific solvents to disperse graphite flakes or few-layer graphene into mono or few-layers, using sonication. Despite its effectiveness, this method's drawback is the requirement for potentially hazardous and costly solvents. Additionally, the removal of these chemicals is often difficult, limiting the purity of graphene obtained [36, 37]. Beyond graphite, other starting materials like graphite intercalation compounds and graphite oxide are also used for exfoliation. Graphite intercalation compounds can be separated into graphene layers either through solvent-based exfoliation or thermal exfoliation [Fig. 2.3], where heating causes the thermal decomposition of the compounds, expanding and separating the layers [37, 38, 45]. For graphite oxide, the introduction of oxygen-containing groups increases the inter-layer distance, facilitating separation into graphene oxide through either thermal exfoliation or sonication in water. A similar example with intercalation compounds is depicted in figure 2.3. Graphene oxide can then be chemically reduced to produce reduced graphene oxide (rGO), which, while hydrophilic and electrically conductive, does not fully replicate the properties of pristine graphene due to incomplete reduction [37, 38].

Bottom-Up Approaches

CVD is renowned for generating high-quality graphene, making it a preferred choice for large-scale production. In CVD, a transition metal substrate is typically heated to around 1000°C within a reactor. Initially, the metal is exposed to hydrogen to remove any oxide layer, followed by the introduction of hydrocarbon gas, which provides the carbon atoms necessary for graphene synthesis. The ratio of hydrocarbon to hydrogen gas is crucial as it influences graphene growth [36, 38]. Nickel (Ni) and Copper (Cu) are commonly used metals for large-scale production, though other transition metals may also be employed, requiring adjustments to growth parameters such as pressure, temperature, and carbon exposure [36–38]. Graphene forms through either surface catalysis, resulting in monolayer graphene, segregation, where carbon dissolves in the metal, diffusing to its surface upon cooling, potentially forming multiple layers, or a combination of both [38]. Post-synthesis, the metal is typically etched away to transfer the graphene onto a target substrate, often by means of a polymer support [Fig. 2.4]. However, this transfer process can damage the graphene, introducing physical defects and contamination [24, 36, 38]. A novel CVD approach involves depositing a Molybdenum (Mo) coating on the desired substrate before growth, allowing direct pattern control of graphene without the need for a post-synthesis transfer, simplifying the process and preserving graphene quality. The produced graphene is released using H_2O_2 solution [24, 46].

Figure 2.4: Schematic representation of graphene growth and removal from metal surfaces. From [38].

Plasma Enhanced CVD (PECVD), introduces a twist to the conventional process by utilising plasma sources like microwaves or radio frequencies. This adaptation allows for graphene film growth at lower temperatures (500-800°C) and shorter times (< 5min), making it compatible with temperature-sensitive substrates. Though PECVD graphene may be of lower quality compared to traditional thermal CVD, its ability to accommodate delicate materials without additional transfers makes it valuable for certain applications [36, 38]. Additionally, PECVD enables the growth of graphene powder [36] or nanosheets [38] via a substrate-free method achieved through the decomposition of ethanol.

Further diversifying the toolkit for graphene production, Laser-Based CVD employs a continuous wave laser to selectively grow graphene on substrate areas exposed to the laser, offering precise control over the growth process within extremely short timescales (nanoseconds to picoseconds) [36]. Similarly, Physical Vapor Deposition (PVD), uses the principles of CVD but operates in an ultrahigh vacuum, evaporating graphite with a laser, and depositing it as graphene on a transition metal substrate. While capable of producing high-quality graphene, this method requires high temperatures, making it less practical for some applications [36].

Epitaxial Growth on SiC offers another route to high-quality graphene by heating SiC to sublime silicon, leaving behind carbon atoms that form graphene. This process can be achieved using various techniques, including high-temperature (> 1000ºC) sublimation in ultrahigh vacuum [37, 38], pulsed electron irradiation in a moderate vacuum level at temperatures between 260 and 530ºC [47], or CO_2 laser heating in an atmospheric pressure argon gas flow, reaching temperatures as high as 2400K (2126.85ºC) [48]. The characteristics of the SiC, such as its phase (hexagonal or cubic) and the exposed side (silicon or carbon-rich), impact the quality and properties of the resulting graphene. Coating SiC with Ni can reduce the temperature required for graphene formation but typically necessitates a transfer step to another substrate, while SiC itself can be directly used in electronic applications. Nonetheless, this method has several drawbacks including the high cost of the SiC substrate, and the difficulty for the removal of graphene from its surface [38].

2.2.3. Graphene Characterisation

Raman Spectroscopy

Raman spectroscopy serves as a non-destructive and versatile tool in the characterisation of graphene and its derivatives across various conditions, widely employed in both research and commercial contexts [49]. This technique involves illuminating the target material, typically with a laser, and analysing the scattered light to reveal insights about the material's properties. The interaction of incident photons with the material's vibrational modes results in both elastic (Rayleigh scattering) and inelastic scattering (Raman scattering). In Rayleigh scattering, the scattered photons retain the incident photons' energy. In contrast, inelastic scattering leads to photons losing or gaining (Stokes or anti-Stokes scattering, respectively) some energy, providing a measure of the vibrational energy modes of the material. This interaction is captured in a Raman spectrum, which plots the intensity of scattered light against its frequency shift with respect to the incident light, offering a detailed profile of the material's characteristics [49–52].

For graphene, the Raman spectrum prominently features three main peaks. The features are depicted in figure 2.5 [49–51]:

- The **G Band** ($\sim$ 1582 cm^{-1}), indicative of the graphene's quality and structural order. This band reflects the in-plane vibrations of sp^2-bonded carbon atoms and is a hallmark of graphitic materials.
- The **2D Band** (or G' Band, $\sim$ 2700 cm^{-1}), significant for its sensitivity to the layers within the graphene sample. The shape and intensity of this band can help determine the number of graphene layers, making it a crucial metric for assessing sample structure.

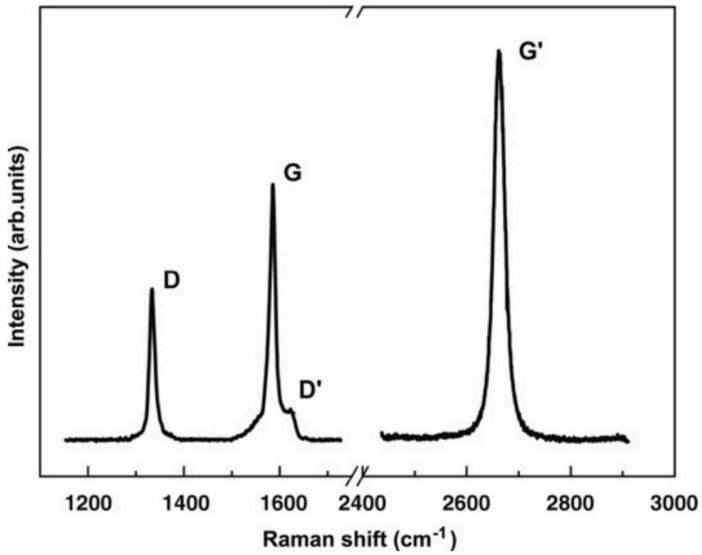

Figure 2.5: Raman spectrum showcasing the main Raman features, the D, G, and G' peaks. From [50].

- The **D Band** ($\sim$ 1350 cm^{-1}), associated with defects or disorder within the graphene lattice. The presence and intensity of the D band serve as indicators of sample quality, with higher values suggesting increased disorder or defects.

When analysing the Raman spectrum, significant attention is paid to the peaks' shape, intensity, position, and full width at half maximum (FWHM), as well as the ratios between these features. Key metrics in graphene characterisation include the intensity ratios of the 2D to G band and the D to G band [50, 51]. A 2D to G band ratio greater than 1 typically signifies monolayer graphene, whereas a ratio less than 1 suggests multilayer graphene [53]. The D to G band ratio, on the other hand, provides an estimate of the degree of defects, with higher values indicating a greater number of defects [49–51].

Optical Transmittance

OT is a critical metric for evaluating the percentage of light that passes through a sample at various wavelengths. For graphene, this measurement is particularly insightful since the transmittance is significantly affected by the sample's layers. Notably, OT has been found to offer more accurate estimates of the number of graphene layers compared to Raman spectroscopy. Reports in literature indicate that a single layer of graphene has an absorbance $\sim$2.3% of visible light, with OT measurements typically conducted at $\sim$ 550 nm. This wavelength is chosen because the transmittance at this point is independent of the stacking order of the graphene layers [54, 55].

A straightforward method to estimate the layer count in a graphene sample is through the equation:

$$N_{Layers} = \frac{(100 - \%T_{550})}{\%A_{Monolayer}} \tag{2.1}$$

Where N_{Layers} represents the sample's layer count, $\%T_{550}$ is the % OT at 550nm, and $\%A_{Monolayer}$ is the % Absorbance rate of a single graphene layer [56].

A refined approach, as detailed in the literature [54], models the OT based on layer count with the equation:

$$T = (1 + 1.13\pi\alpha N/2)^{-2} \tag{2.2}$$

Here T stands for the OT in decimal representation, N is the number of layers, and α represents the fine-structure constant, approximately $\frac{1}{137}$. This equation can be reformulated to solve for$N$, providing the formula to accurately determine the number of layers in a graphene sample:

$$N = \frac{2(\sqrt{T^{-1}} - 1)}{1.13\pi\alpha} \tag{2.3}$$

It's important to adjust the OT measurements for any absorbance attributed to the substrate, ensuring accurate layer estimation. This more nuanced approach allows for the precise characterisation of graphene samples.

2.2.4. Graphene Microelectrode Arrays

Graphene's remarkable properties have driven its adoption across a broad spectrum of applications, ranging from transistors and energy storage devices to electrodes, polymer composites, and sensors [38, 57]. In the healthcare domain, graphene's unique structure supports tissue engineering for specific cell types [57–59], and its surface can be functionalised for biosensing purposes [57, 60–62]. Its extensive surface area is advantageous for delivering drugs or gene therapies [57, 63–66], while its superior electrical, mechanical, and optical qualities position it as an ideal material for developing flexible and transparent electronics [37, 43, 57, 67, 68].

Despite graphene's widespread use, concerns regarding the biocompatibility of graphene-family nanoparticles have been raised, citing potential toxicity linked to their physical and chemical characteristics [69–71]. However, graphene sheets, used as substrates or surfaces interacting with cells, have demonstrated no cytotoxic effects, ensuring their safety in biomedical applications [4, 23, 68].

A notable area of graphene's application is in the development of transparent and flexible electronics, especially for neural recording and stimulation [Fig. 2.6 (a and b)]. Graphene MEAs stand out for their flexibility and transparency, which make them ideal for in-vivo applications [5, 43, 57, 67, 72, 73]. These devices not only support traditional neural recording and stimulation but also enable the integration of optical techniques like calcium imaging, fluorescence imaging, optogenetics, and even magnetic resonance imaging (MRI), overcoming the limitations of traditional MEAs which are often opaque, photostimulation sensitive, and MRI incompatible. This integration significantly improves the spatio-temporal resolution achievable, surpassing that of conventional methods [23, 29, 43, 74]. While ITO offers a transparent alternative, its rigidity restricts implant applications. In contrast, the flexibility of graphene implants minimises tissue damage and inflammation, attributed to its compatibility with the mechanical properties of tissue [4, 25–27, 35, 57, 75].

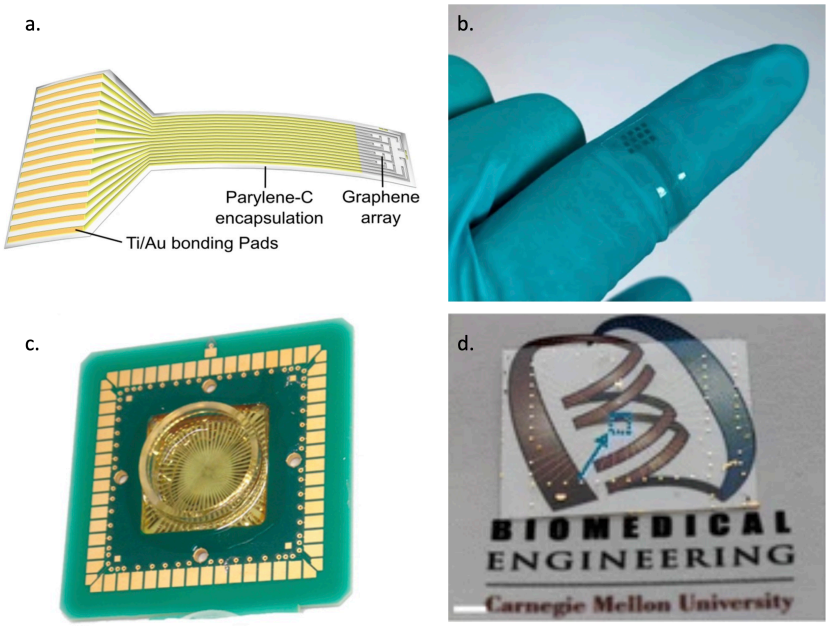

Figure 2.6: Graphene microelectrode arrays reported in literature. **a.** Diagram of flexible and transparent μECoG device. From [3]. **b.** Suspended graphene electrode with PDMS substrate. From [43]. **c.** Flexible MEA soldered to a carrier and encapsulated for in-vitro stability. From [4]. **d.** Graphene MEA fabricated on a glass coverslip. The blue arrow points to area with electrodes. From [23]

Graphene has also been employed in the creation of rigid transparent MEAs, predominantly used for in-vitro studies of neural and muscle cells [Fig. 2.6 (c and d)]. These transparent electrodes facilitate optical imaging and optogenetic stimulation, presenting a versatile tool for scientific research [1, 23,

76–78].

A review of the characteristics of various graphene devices reveals the predominant use of CVD for graphene production and different graphene layer counts across studies. Table 2.1 summarises the principal characteristics of the reviewed graphene devices. Compared to traditional electrode materials like Au and Pt, graphene exhibits higher impedance for electrodes with identical geometries and surface areas, which might lead to a lower SNR. Nonetheless, graphene-based devices have proven effective for recording neural activity [23, 43, 57, 76, 78, 79]. Moreover, graphene's stability in biological environments outperforms materials like Au, maintaining consistent impedance over exposure to cell culture environments of multiple weeks. This stability underscores graphene's potential as a reliable alternative for signal acquisition in medical devices [76].

2.3. Characterisation Methods of Recording Electrodes

2.3.1. Electrochemical Impedance Spectroscopy

EIS stands as a pivotal technique for characterising recording electrodes. This approach involves perturbing the electrochemical system with a low-amplitude alternating (sinusoidal) signal, typically ranging from 10 to 100 mV. This choice of amplitude aims to avoid Faradaic reactions at the electrode-electrolyte interface, thereby ensuring linearity in the response. The frequency of this signal spans from 1 mHz to 1 MHz, enabling the analysis of electrochemical processes at varying speeds — slow processes at lower frequencies and faster ones at higher frequencies [85, 86].

The typical experimental setup for EIS consists of a three-electrode setup [Fig. 2.7] immersed in an electrolyte solution, such as PBS for biological research. This system comprises a working electrode (WE) under investigation, a counter electrode (CE) serving as the circuit's ground and positioned away from the WE, and a reference electrode (RE), which provides a stable potential for accurate measurements. The RE is placed near the WE but without contact, ensuring precise potential difference readings between the WE and RE, while the stimulation is applied between the WE and the CE [85, 86].

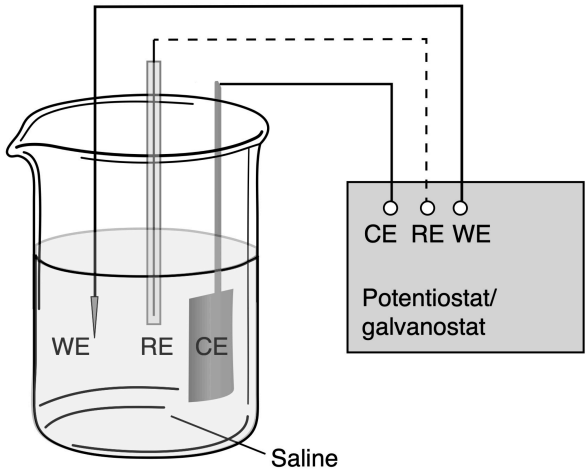

Figure 2.7: Simple diagram depicting the three-electrode setup used commonly for electrochemical characterisation. In it, you can visualise the working electrode (WE), counter electrode (CE), and reference electrode (RE). From [85].

The electrochemical impedance **(Z)** of the system is derived from the combined effects of resistance (the real component, **Z'**) and reactance (the imaginary component, **Z"**), formulated as:

$$Z = Z' + jZ'' \tag{2.4}$$

Here, **Z'** reflects the in-phase relationship between voltage and current, indicative of the system's resistive aspects, while **Z"** represents the out-of-phase components, capturing the system's capacitive and inductive behaviour. The relationships are mathematically represented as:

$$Z' = \frac{V_0}{I_0} \cos(\phi) \tag{2.5}$$

$$Z'' = \frac{V_0}{I_0} \sin(\phi) \tag{2.6}$$

where V_0 and I_0 denote the amplitudes of the applied voltage and resulting current, respectively, and ϕ is the phase shift between them [86].

Data from EIS measurements can be visualised in a Nyquist plot, which plots **Z"** against **Z'**, offering insights into the resistive and capacitive behaviours of the system. This plot is instrumental in identifying phenomena such as charge transfer resistance and mass transfer processes [86].

Alternatively, data representation in a Bode plot contrasts the amplitude and phase shift of the stimulus with the response, quantifying the impedance magnitude and phase angle as:

$$|Z| = \sqrt{Z'^2 + Z''^2} \tag{2.7}$$

$$\phi = \arctan\left(\frac{Z''}{Z'}\right) \tag{2.8}$$

Where $|Z|$ is the magnitude of the impedance. The Bode plot displays the impedance over the frequencies (both in logarithmic scale), and the phase shift in linear scale over the frequencies in logarithmic scale. Together they provide information about the electrochemical system's dynamics including the behaviour of the electrode electrolyte interface, and the systems' overall capacitive and resistive properties [85, 86].

2.3.2. Stability Assessment

When characterising electrodes intended to interface with biological tissue, their durability is a critical factor. These devices will be exposed to harsh biological environments for extended periods of time and must withstand swelling, delamination, dissolution, and corrosion. This is particularly important for implantable devices, which are not easily replaced and require surgical intervention for removal or replacement. Ageing tests are essential in assessing durability in an accelerated ageing environment. This environment attempts to replicate the long-term effects of exposure to biological conditions in a shorter period of time. These tests, alongside other characterisation techniques including EIS and optical microscopy, provide insight into the device's stability and potential failure mechanisms, highlighting areas for improvement [85, 87, 88].

Typically, ageing tests involve immersing the device in a solution that emulates a biological medium (e.g., PBS) at elevated temperatures. The rationale is that higher temperatures increase the system's kinetic energy, accelerating degradation reactions. Modifications to the ageing test, such as adding H_2O_2 or altering the pH, can further emulate the immune system's response to the presence of the device, a critical consideration for implantable devices, as such responses can significantly shorten the device's lifespan [85, 87, 88].

It is important to tailor the ageing test to the specific materials used in the device. For instance, most polymers are susceptible to degradation under high temperatures. Thus, to ensure the study accurately reflects how the device ages in biological conditions, the test temperature must be carefully selected to prevent unrepresentative damage to these materials [87, 88].

2.3.3. Signal-to-Noise Ratio

The SNR is a key measurement used to evaluate the performance of sensing electronics, for instance, interfacing with biological tissues. It is calculated as the ratio of the strength of the desired signal to the level of baseline noise [2, 89]. Despite its widespread application, there is no standard approach to the quantification of the signal and baseline noise, due to the varied origins and characteristics of signals and the specific purposes of different studies.

For example, in neural recording studies, SNR is often calculated by comparing the amplitude of the highest peaks during active periods to the standard deviation of the background signal during quiet periods [89]. The way baseline noise is quantified can vary significantly, employing methods such as standard deviation (SD), root mean square (RMS), and maximum absolute deviation (MAD), sometimes in combination or modified forms (e.g., $MAD(SD(noise))$, or $2 \cdot RMS(noise)$). The duration of recordings used to establish baseline noise also differs among studies. Similarly, the methods for quantifying peak amplitudes are diverse, ranging from peak-to-peak amplitude to RMS, with measurements taken

over single or multiple peaks and varying signal lengths [2, 5, 89–92]. More elaborate methods exist, but those tend to be used for very specific applications [3, 12].

However, relying solely on peak values to calculate SNR has its limitations, as it only assesses device performance at the frequency of recorded events, offering a narrow view of the device's overall behaviour [89]. Alternative approaches may also be used depending on the purpose of the studies. For instance, an investigation into the optimal electrode size for recording from neuronal assemblies, accounted for the influence of electrode size on three key parameters in the SNR calculation [12].

In another study, they investigated the influence of stimulation frequency and signal amplitude on SNR. The signals were generated experimentally through an electrode in PBS, and detected by the recording electrodes of a MEA. A continuous sinusoidal signal at different frequencies was used to stimulate the electrodes, and the complete recorded signal was quantified based on the power spectral density at the stimulation signal frequency. Similarly, baseline noise was determined through the power spectral density at the same frequency from a zero-volt stimulation. This quantification approach produces values equivalent to the RMS of the signal and baseline noise [2].

In summary, calculating SNR requires a flexible approach tailored to the specific requirements of each study. There is no universal method, underscoring the need for clear documentation of the chosen methodology to facilitate comparison between different studies.

Device	Flexible	Transparent	Electrode material	Additional information	Substrate	Encapsulation	Electrode Area μm^2	Impedance at 1kHz $k\Omega$	Area Normalised Impedance Ωcm^2	Optical Transmittance at 550nm (%)	Reference
Neural interface	yes	yes	Multilayer CVD Graphene	Transfer free	Parylene C $10\mu m$	Parylene C $10\mu m$	68320	27.4±7.5	18.72±5.1	83.5	Bakhshaee [43]
Neural interface	no	no	Multilayer CVD Graphene	Transfer free	Silicon	Photoresist	68320	31.45±5.88	21.49±4.0		Bakhshaee [80]
				Transfer free & 40% Pt nanoparticles				7.26±0.90	4.96±0.6	>92	
Spinal cord implant	yes	yes	Multilayer CVD Graphene	Transfer free	PDMS	PDMS $50\mu m$	68320	8.2	5.6	78.3	Velea [67]
Electrophysiology and neuroimaging	yes	Yellow tone	CVD Monolayer Graphene	Doped with HNO_3	Polyimide	SU-8	2500	541	13.5	>80	Kuzum [5]
Neural interface	yes	yes	Two staked CVD Monolayer Graphene	Doped with HNO_3	Parylene C $4\mu m$	Parylene C $4\mu m$	2500	908±488	22.7±12.2	∼90	Driscoll [3]
Neural interface	yes	yes	Four stacked CVD Monolayer Graphene		Parylene C	Parylene C	31416	215.7±120.4	67.76±37.8		Park [72]
Neural interface	yes	yes	Four stacked CVD Monolayer Graphene		Parylene C	Parylene C	unclear	243.5±5.9		∼90	Park [81]
Neural interface	yes	yes	Monolayer CVD Graphene		PET film $25\mu m$	SU-8 $8\mu m$	2500	1400	35	>80	Liu [82]
Neural interface	yes	yes	Monolayer CVD Graphene		PET	SU-8	10000	872.9	87.29	>90	Lu [73]
Neural interface	yes	yes	Graphene		PET $50\mu m$	SU-8	10000	963	96.3	>80	Thunemann [74]
Neural interface	yes	yes	Monolayer CVD Graphene		SU-8 + additional layers	SU-8	15394	200	30.79	∼90	Park [83]
Neural interface	yes	yes	Monolayer CVD Graphene		PET	SU-8 $5\mu m$	10000	200	20		Lyu [84]
Neural interface	yes	yes	Two staked CVD Monolayer Graphene	Doped with HNO_3	Parylene C $14\mu m$	Parylene C $2\mu m$	314	5400	16.96	90	Ramezani [6]
Electrophysiology	yes	Yellow tone	Graphene + metal lines		Polyimide film $10\mu m$	Polyimide $3\mu m$	314	100±50	0.31±0.16		Kireev [4]
Neural interface	no	yes	Few layers CVD Graphene		Borosilicate glass	SU-8	707	2650±260	18.73±1.84	>85	Korbitzer [76]
Electro- and Optophysiology	no	yes	Monolayer CVD Graphene		Float Glass	SU-8	707	3000	21.21	>85	Kshirsagar [77]
Neural electrophysiology	no	yes	Stacked Multilayer CVD Graphene + metal lines		Quartz 1mm	Polyimide $1\mu m$	314	170±11.1	0.53±0.03	∼90	Du [1]
Electro- and Optophysiology	no	yes	CVD Graphene + metal lines	Bare graphene electrodes	Float Glass	SU-8	707	700	5.0	∼90	Kshirsagar [78]
				Electrode with deposited PEDOT:PSS				50	0.36	∼ 55	
Electro- and Optophysiology	no	yes	Monolayer CVD Graphene	Bare graphene electrodes	Glass	SU-8	2500	2100±300	52.5±7.5	97.7	Rastogi [23]
				Doped with HNO_3				1500±200	37.5±5.0		

Table 2.1: Summary of outcomes from reviewed studies on graphene MEAs.

3

Device Design and Fabrication

In this project, a transparent gMEA was fabricated, intended to perform electrical signal recordings and optical voltage mappings simultaneously, from photostimulated optogenetic cell lines. The design aimed to enable photostimulation of the cells from a source beneath the gMEA while permitting unobstructed optical measurements from above the gMEA. The electrodes were crafted from multilayer CVD graphene, chosen for its transparency and beneficial electrical properties. In this chapter, the device design, including the choice of materials and fabrication process within and outside the cleanroom is presented.

3.1. Device Design

The device's primary purpose was to record electrical signals from optogenetic cell lines. To align closely with existing equipment at LUMC, the gMEA was modelled after a commercial Multichannel Systems MEA (MCS-MEA) (60MEA200/30iR-Ti) with titanium electrodes and tracks. This design ensured compatibility with the available amplifier (FM60-AMP Rev.B SerNo. 047) and enabled a realistic performance comparison between the MCS-MEA and the gMEA. A detailed diagram of the gMEA design is presented in figure 3.1.

The gMEA features 60 microelectrodes (59 working electrodes and 1 large return electrode) with a 30 μm diameter in an 8x8 array (no electrodes on the corners of the array), spaced 200 μm apart (centre-to-centre) [Fig. 3.1 (b and c)]. Each electrode connects to a pad near the device's edges, enabling a connection with the amplifier. The overall device measures 49x49 mm, and a well surrounding the electrodes allows for cell line cultivation. Note that figure 3.1 does not show the 49x49 PCB extension, which is covered in Section 3.3.1.

Two electrode designs were implemented, one with a solid surface, replicating those in commercial MEAs, and a second one incorporating 12 2x2 μm openings on its surface, creating a net-like structure [Fig. 3.1 (d and e)]. The openings are intended to facilitate the adhesion of metal layers on the electrode surface by offering an anchor point to the substrate [67]. In contrast, the purpose of the solid surface electrodes was to test if improved adhesion is necessary for these small structures. The outcomes are briefly discussed in Section 6.3.

3.2. Device Materials

A key characteristic of the device is its transparency, crucial for allowing optogenetic stimulation of cells via a light source positioned beneath them. Therefore, all materials selected for the device need to be transparent. Another important consideration is the compatibility of these materials with microfabrication processes, particularly those involving graphene, which is the chosen material for the electrodes. The device's construction will involve four primary materials, each corresponding to a different component of the gMEA: the substrate, electrodes, contact pads and tracks, and encapsulation layer.

Given the choice of graphene for the electrodes, this selection imposes certain material constraints on the other components. Graphene synthesis at EKL is carried out using the AIXTRON Black Magic Pro furnace, which employs CVD to create layers of graphene on a surface. This process also requires

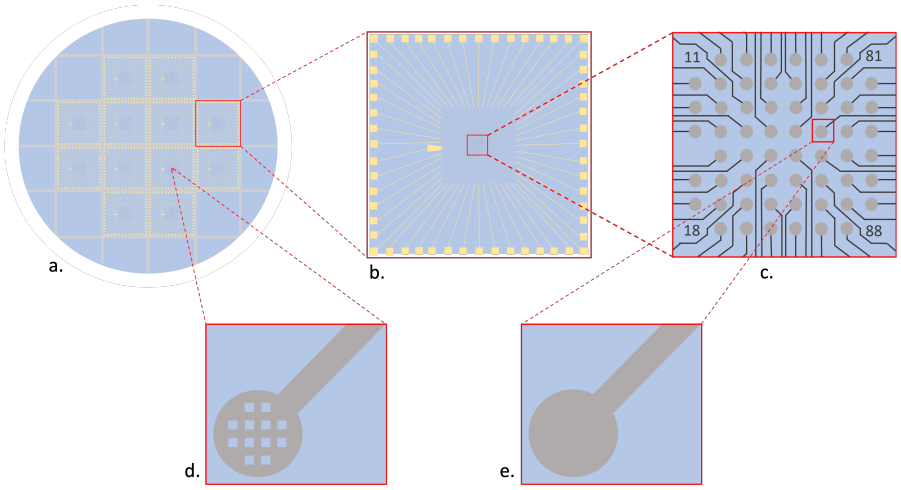

Figure 3.1: gMEA design: **a**: Full wafer view with 12 gMEA devices; **b**: Overview of a single gMEA device (without openings); **c**: Zoomed-in view of the electrode array and tracks; **d**: Zoomed-in view of a single electrode with openings; **e**: Zoomed in view of a single electrode with no openings

high temperatures, up to 1050ºC, which must be considered when selecting compatible materials for the other components of the gMEA.

3.2.1. Substrate Selection

The substrate forms the base on which all device components are constructed, making it crucial for the substrate to withstand all microfabrication processes used in device fabrication. Several transparent materials are suitable, including glass, quartz or fused silica (SiO_2), and sapphire (Al_2O_3). However, only quartz and sapphire can endure the high temperatures involved in graphene growth. Furthermore, since the properties of the substrate material can influence the quality of graphene grown on it, the optimal graphene growth parameters were determined for each substrate and the one yielding the best graphene properties was selected.

The methodology for this experiment is elaborated in the graphene characterisation Section [4.1]. Comparative analysis showed severe graphene delamination on sapphire substrates during fabrication. Consequently, quartz was chosen as the preferred substrate. Additionally, quartz or fused silica, being composed of SiO_2, share the same composition as the passivating layer on silicon wafers. This similarity is advantageous as graphene has previously been grown on SiO_2 with satisfactory adherence, further supporting the selection of quartz as the substrate material [43, 56, 80].

3.2.2. Contact Pads and Tracks Material Selection

The material for the contact pads and tracks of the device needs to be conductive with low impedance and favourable wire bonding properties. Additionally, in this specific device, the selected material will also be used for the return electrode, which differs from the working electrodes in having a larger surface area and being relatively distant from the measurement region.

The electrical recordings are based on the potential difference between the working and the return electrodes. Several materials are suitable for this purpose, including pure aluminium, gold, and platinum. Platinum was initially ruled out due to its non-bondable nature, poor electrical contact with graphene, and low adhesion to quartz [93–95]. Among the remaining candidates, gold and pure aluminium both present viable options. Gold is a noble metal offering excellent biocompatibility and biostability [96]. Pure aluminium also exhibits good biocompatibility, thanks to its surface oxide layer, but it is less biostable and some of its ions are considered cytotoxic [96, 97].

The decision between gold and pure aluminium was influenced by anticipated future tests. For instance, conducting cyclic voltammetry (CV) on a device with a pure aluminium return electrode might trigger electrochemical reactions, leading to electrode degradation and aluminium ion formation. Consequently, gold was chosen for the contact pads, tracks, and the return electrode. Its major limitation, especially in optogenetics, is its photosensitivity, which could result in photoinduced artifacts [43, 82].

To mitigate this issue, the gold structures will be positioned away from the light-exposed area, ensuring the light stimulus does not directly interact with the gold-containing regions of the device [Fig. 3.1 (b)].

3.2.3. Encapsulation Selection

In selecting an encapsulator for the device, transparency and biocompatibility are paramount, as the device is intended for optogenetic stimulation from a light source beneath the cells. The best candidates possessing these qualities are SU-8, PDMS, and parylene C, all commonly utilised in biomedical applications [98–101].

SU-8 was initially considered due to its transparency, biocompatibility, and ease of processing through conventional microfabrication techniques [102–105]. However, reports of crack formation in SU-8 structures, indicating material instability, led to its exclusion as a potential insulator [87]. Both PDMS and parylene C are highly stable and biocompatible, further endorsed by USP as class VI materials suitable for long-term implants [98, 101, 106–109]. These insulators have been previously used by TU Delft for graphene electrode encapsulation [43, 67], showing their suitability for this application.

Between PDMS and parylene C, PDMS is potentially more suitable for future applications in implantable flexible devices due to its low Young's modulus, which is more compatible with the mechanical properties of soft biological tissues, thus promoting long-term biointegration [75, 99, 101]. However, for this rigid device, the higher Young's modulus of parylene C (2.76 GPa) is not a concern [110]. Parylene C's uniformity and conformity, controlled accurately through CVD, give it an edge over PDMS, which is applied through spin-coating and lacks conformal layering [99]. Additionally, parylene C's excellent barrier properties, including low gas and moisture permeability, and dielectric properties, outweigh PDMS's high permeability, making it a more effective device barrier. Nonetheless, both materials show some degree of gas and vapour permeability, that will eventually lead to short-circuits or delamination [98–100].

Despite parylene C's advantages, some studies indicate its potential degradation during long-term (> 6 months) in-vivo experiments, but this is not a concern for this project as the gMEA is only required to be operational for about 12 days [88, 100, 111–114]. Therefore, parylene C is preferred over PDMS, particularly due to better control over layer thickness via CVD. This factor is crucial as the cell-electrode cleft gap in cell cultures significantly affects recorded signals. Although there is no consensus in literature on the ideal cleft gap, it is agreed that it should be minimised [29, 43, 67, 115–117].

Considering heart cells' size (10-20 μm in diameter, 50-100 μm in length) [118] relative to the gMEA's 30 μm electrode diameter, a few micrometres thick insulator layer is adequate. However, given the cells' large diameter compared to the electrode openings, a thinner encapsulation layer would be beneficial. A 1 μm thick layer of parylene C should create a small cell-electrode cleft gap, thus enhancing cell integration with the electrodes.

3.3. Device Fabrication

The device fabrication process involves a series of steps to create the desired gMEA. This section focuses solely on the microfabrication procedures within the cleanroom. For detailed steps of the microfabrication process, refer to the flowchart in the Appendix A of this thesis. The fabrication steps are grouped into four main stages: Graphene Growth, Metallisation, Encapsulation, and Final Steps.

3.3.1. Mask Design

Previously, we discussed the gMEA's general design and intended materials. To realise these designs via microfabrication, lithography will be employed. Lithography uses masks, which consist of a glass plate with a chrome pattern corresponding to the desired design. This mask, in conjunction with photosensitive polymers, imprints the design onto a surface (in our case, a quartz wafer). Subsequent treatments add or remove material from areas unprotected by the polymer. This technique allows for the creation of very small features with high resolution. Each material layer in the design requires a distinct mask, totalling four masks for our design. These include:

1. **GRAPHENE** mask for the working electrodes and tracks [Fig. 3.2 (b)].
2. **METAL ELECTRODES** mask for the protective metal layer above the electrodes [Fig. 3.2 (c)].
3. **METAL PADS** mask for the return electrode, metal tracks, and contact pads [Fig. 3.2 (d)].

4. **OPENINGS** mask for apertures above the electrodes on the insulating material [Fig. 3.2 (e)].

The final device size is 49x49 mm to fit the recording device. However, such a size would necessitate a full 100 mm wafer for a single device. To optimise production, the design was scaled down to 20x20 mm, incorporating the gMEA and space for the attachment of a cell culture well. This small die will later be wire-bonded to a PCB, acting as an adapter between the gMEA and the amplifier. This approach enables the production of 12 gMEAs (6 with and 6 without electrode openings) from a single wafer [Fig. 3.1 (a)]. The masks were designed using L-Edit and manufactured by Compugraphics. The mask model 8160A1 is suitable for the SUSS MicroTec MA/BA8 contact aligner that was used, which imprints the surface with the design's exact size.

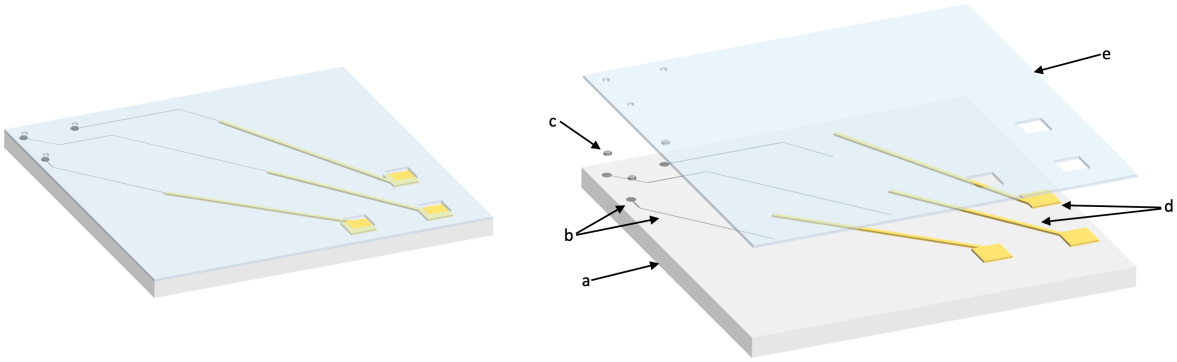

Figure 3.2: Diagram representation of the principal material layers used in the production of gMEAs, but not all materials are kept in the final device. gMEA material layers: **a**: Quartz substrate; **b**: Graphene electrodes and tracks grown above a Mo pattern; **c**: Pure aluminium (pAl/Ti) protection pads over graphene electrodes; **d**: Gold (Au/Ti) tracks and contact pads; **e**: Parylene C encapsulation layer with electrode and contact pad openings.

3.3.2. Graphene Growth

Alignment markers were not initially added to the wafer, due to its transparency. Instead, mask alignment was manually performed on the contact aligner using the alignment markers from the first used mask (GRAPHENE).

Graphene was grown using a transfer-free method [24] via CVD in the AIXTRON Black Magic Pro furnace. This process involves using Mo as a catalyst in the graphene growth process. The Mo is patterned to create a graphene layer in the desired pattern. Once the microfabrication steps are complete, the Mo layer beneath the graphene is removed using hydrogen peroxide (H_2O_2), allowing the graphene to adhere to the substrate via van der Waals forces.

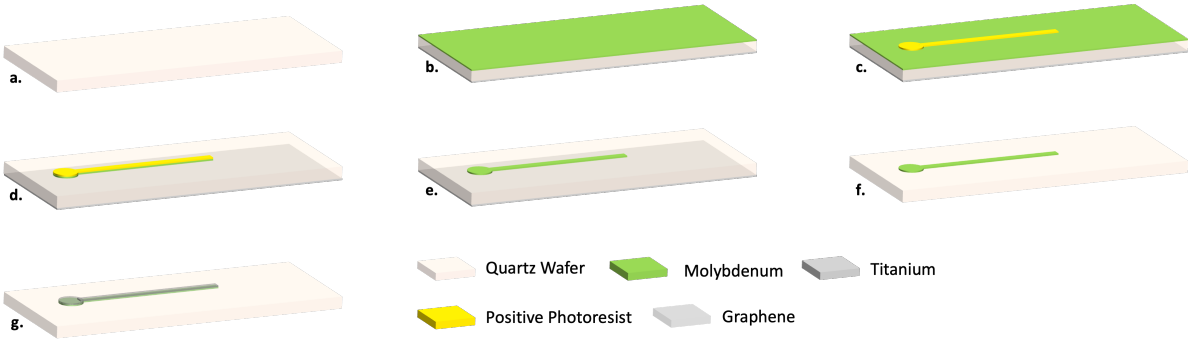

Figure 3.3: Graphene layer fabrication steps diagram: **a**: Bare quartz wafer. **b**: Frontside sputtered with 50 nm of Mo, and the backside sputtered with 50 nm of Ti. **c**: Coating and patterning positive photoresist layer. **d**: Plasma etching of Mo. **e**: Photoresist removal. **f**: Wet etching of Ti. **g**: Graphene growth over the Mo catalyst via CVD.

The quartz wafers are initially coated with 50 nm of Mo on the front side and 50 nm of titanium on the backside at 50 ºC using the Trikon Sigma sputterer [Fig. 3.3 (b)]. The backside coating renders

the wafer opaque, necessary for machines that cannot detect transparent wafers. The Mo layer is patterned using the GRAPHENE mask through lithography [Fig. 3.3 (c)] and dry etching [Fig. 3.3 (d)] with the SUSS MicroTec MA/BA8 contact aligner and the Trikon Omega 201, respectively.

Before graphene growth, the photoresist and titanium layer need to be removed. The photoresist is stripped in the spray coater with acetone and IPA [Fig. 3.3 (e)], while the titanium backside layer is removed through wet etching in 0.55% HF (Hydrogen Fluoride) [Fig. 3.3 (f)]. Finally, the wafer is placed in the AIXTRON Black Magic Pro furnace chamber, and graphene is grown at 915ºC with 960, 40, and 25 sccm of Ar, H_2, and CH_4 gas flows, respectively, at 25 mbar pressure for 20 min [Fig. 3.3 (g)]. The outcome of this process is depicted in figure 3.4 (L).

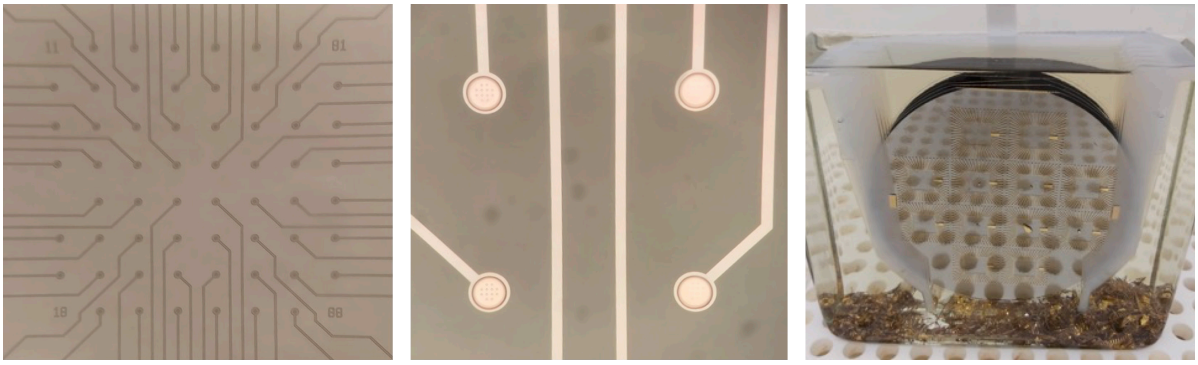

Figure 3.4: Microscope images of devices during fabrication: **Left**: Quartz wafer after Mo patterning and graphene growth. Visual of the microelectrodes and some tracks. **Center**: Electrode landing pads on top of graphene electrodes. Visual of electrodes with pure aluminium (pAl/Ti) landing pads on top of them. Graphene and Mo tracks are also visible. **Right**: Liftoff procedure with NI555. Visual of gold peeling off in an NI555 bath. The desired gold pattern of tracks, contact pads, and return electrodes are visible on the wafer.

3.3.3. Metallisation

The metallisation process for this device is divided into two distinct metal deposition phases. The first involves depositing pure aluminium to shield the graphene electrodes from potential damage during the etching of openings in the encapsulation layer. The second deposition uses gold to form the tracks and contact pads of the device.

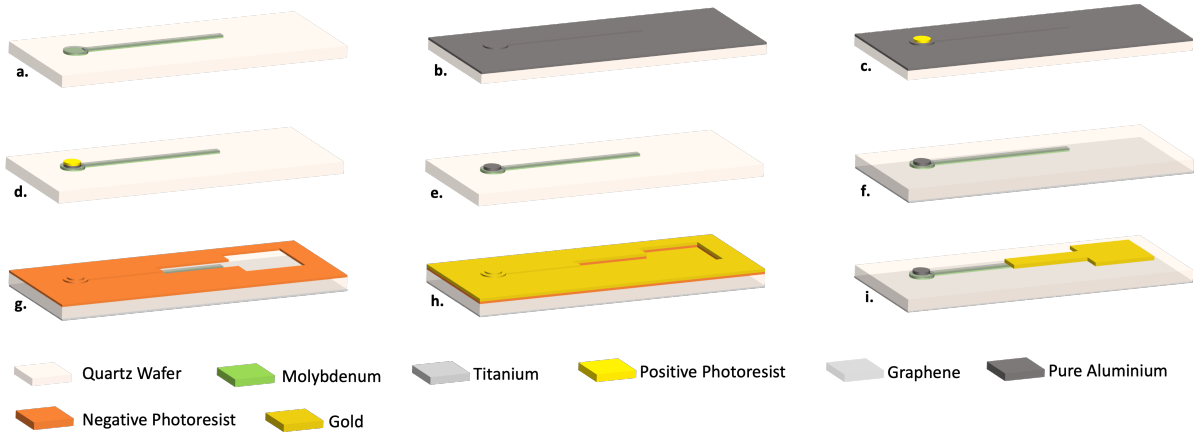

Figure 3.5: Fabrication steps diagram of electrode landing pads, and MEA tracks and contact pads: **a**: Device after graphene growth. **b**: Sputtering 100 nm of pAl with a 50 nm Ti adhesion layer. **c**: Coating and patterning positive photoresist layer. **d**: Wet etching of pAl and Ti. **e**: Photoresist removal. **f**: Physical vapour deposition of 200 nm of Ti on the backside. **g**: Coating and patterning negative photoresist layer. **h**: Physical vapour deposition of 200 nm of Au with a 10 nm Ti adhesion layer. **i**: Liftoff of the Au.

After the graphene growth, the wafers are sequentially sputtered with 50 nm of titanium (as an adhesion layer) and 100 nm of pure aluminium in the Trikon Sigma, maintaining a continuous vacuum environment [Fig. 3.5 (b)]. Subsequently, the metal layer is coated with photoresist, and then patterned

using the METAL ELECTRODES mask with the SUSS MicroTec MA/BA8 contact aligner [Fig. 3.5 (c)]. Following the development of the photoresist, the metal layer is etched in a 0.55% HF bath [Fig. 3.5 (d)]. The remaining photoresist is then manually stripped in acetone and IPA, and rinsed with DI water [Fig. 3.5 (e)]. An image illustrating the outcome of adding the electrode protection pads is available in figure 3.4 (C).

The second metal deposition involves adding a gold layer through the lift-off technique. Initially, the backside of the wafer is coated with 200 nm of Ti [Fig. 3.5 (f)] in the CHA Solution Std. machine. The purpose of the titanium layer on the backside is to facilitate electrostatic clamping in the Adixen AMS110 plasma etcher for a later step [3.3.4]. Subsequently, the frontside of the wafer is coated with negative photoresist and patterned using the METAL PADS mask in the SUSS MicroTec MA/BA8 contact aligner [Fig. 3.5 (g)]. Post-development, the CHA solution Std. machine deposits 10 nm of titanium (as an adhesion layer) followed by 200 nm of gold [Fig. 3.5 (h)]. The lift-off process commences by immersing the wafers in an NI555 bath at room temperature overnight. Figure 3.5 (i) depicts the fabrication step graphically, and figure 3.4 (R) shows a wafer in NI555 near liftoff completion. Once the liftoff is complete and all photoresist has been removed, the wafers are rinsed in DI water and air-dried.

3.3.4. Encapsulation

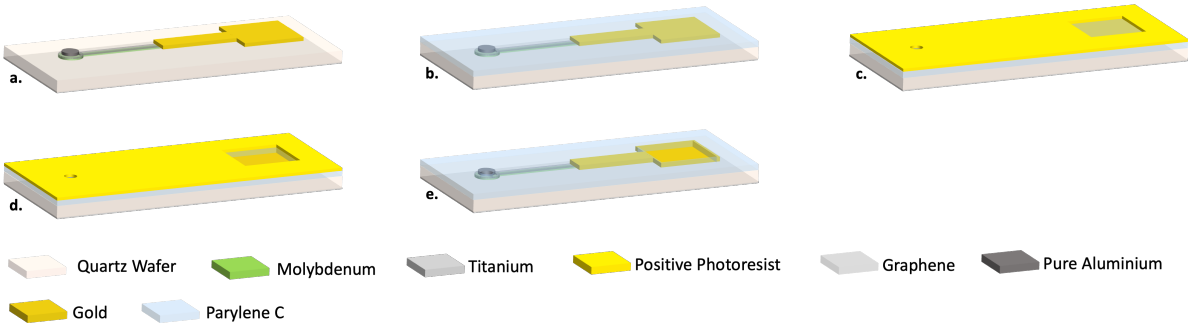

Figure 3.6: Fabrication steps diagram of encapsulation parylene C layer: **a**: Device after liftoff process. **b**: Deposition of 1 μm of parylene C through CVD. **c**: Coating and patterning negative photoresist. **d**: Create openings on the parylene C layer through oxygen plasma. **e**: Removal of photoresist.

The encapsulation layer for the device will be made of parylene C, deposited using the LABCOATER 2 (PDS 2010) parylene deposition machine, by means of CVD, in the MEMS lab. To achieve the desired thickness of 1 μm, 2 grams of parylene C dimer is loaded into the machine. During the deposition process, the wafers are placed on a glass slide to prevent Parylene deposition on the backside [Fig. 3.6 (b)].

Post-deposition, the encapsulation thickness is verified by removing a small section of the parylene C layer from a corner of the wafer (where no structures are present) and measuring the height difference, between the parylene surface and the substrate, with the Dektak 8 Surface Profilometer.

Following parylene C coating, the wafers are manually coated with photoresist on the front side and patterned using the OPENINGS mask in the SUSS MicroTec MA/BA8 contact aligner [Fig. 3.6 (c)]. After development, the openings are created using oxygen plasma on the Adixen AMS110 plasma etcher, which is contaminated and thus can be used for etching wafers with gold [Fig. 3.6 (d)] . Figure 3.7 showcases the return electrode and contact pad openings prior to photoresist removal. Finally, the photoresist layer is removed in the spray coater by spraying acetone and IPA [Fig. 3.6 (e)].

3.3.5. Final Steps

After creating the openings in the encapsulation layer, the next step is dicing the wafers. Initially, a protective photoresist layer is applied and developed, though without any pattern on it. The dicing process is carried out in the Biosonics lab using the Disco Dicer (DAD3240) with a glass blade (R07-SDC400-BB101-75 51.4 X 0.1A2 X 40) at a low-speed setting (0.5 mm/s). Post-dicing, the photoresist on the dies is manually removed in acetone, followed by rinsing with IPA and DI water. Figure 3.9 (L) shows the 12 dies from a diced wafer before the removal of photoresist.

Upon completion of the potentially damaging steps for the device, it is necessary to remove the

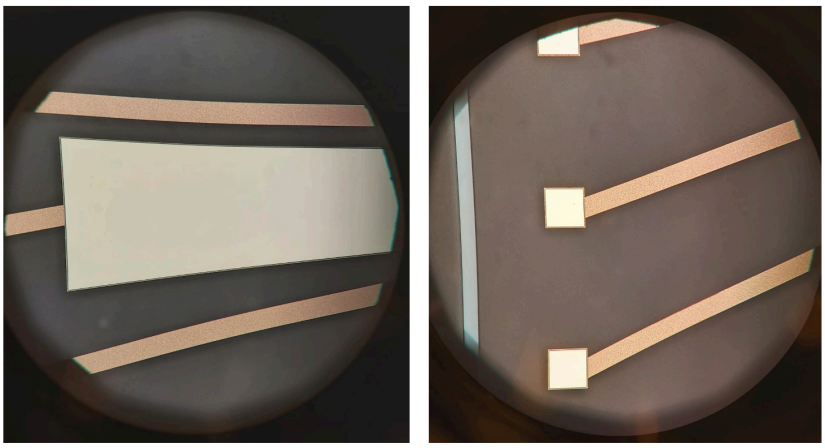

Figure 3.7: Return electrode and contact pad images after creating openings on parylene C layer, and before photoresist removal. **Left**: The parylene C on the gold return electrode surface has been removed, leaving a thin margin around the edges. The surrounding gold tracks are coated as can be seen from the colour difference. **Right**: Openings on parylene C layer above gold contact pads. The lighter grey line to the left of the contact pads is the division between gMEA devices, has no parylene C, and reaches all the way to the quartz wafer.

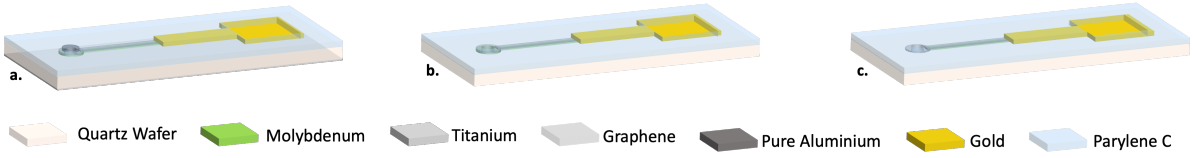

Figure 3.8: Fabrication steps diagram for the removal of sacrificial structures. **a**: Device after creating the openings in the encapsulation layer. **b**: Wet etching of pAl and Ti. **c**: Wet etching of the Mo beneath the electrodes (not in tracks).

sacrificial structures, including the protective metal layer above the graphene electrodes, the Mo beneath the electrodes, and the opaque titanium backing layer. This is accomplished by immersing the wafers in a 0.55% HF bath to etch away the unwanted aluminium and titanium structures [Fig. 3.8 (b)]. The wafers are then thoroughly rinsed in DI water. The removal of the Mo layer involves covering the surface of the horizontally placed die with a 37% hydrogen peroxide solution (H_2O_2) [Fig. 3.8 (c)]. To facilitate the etchant's penetration into the electrode openings, a drop of Triton solution is added before the hydrogen peroxide to break the surface tension. Following the etching process, the dies are abundantly rinsed with DI water to remove all resultant Mo compounds and then left to air dry for 24 hours. An additional low-temperature baking step is conducted after 24 hours to eliminate any remaining water beneath the graphene layer, thereby enhancing the graphene's adhesion to the substrate.

3.4. PCB Adaptor and Growing Well

3.4.1. PCB Adaptor

The PCB circuit functions as an adaptor, bridging the leads from the fabricated gMEA dies to the amplifier's contacts, which are designed for 49x49x1 mm devices. The PCB itself is of matching dimensions (49x49 mm) with a thickness of 1mm and a central opening of 20x20 mm, correlating with the size of the gMEA die.

To attach the gMEA die to the PCB [Fig. 3.10 (a)], the PCB is positioned on a flat metal plate, with a quartz wafer fragment placed within its opening. This step compensates for the 0.5 mm thickness of the wafer, ensuring the gMEA die's surface aligns evenly with the PCB's surface. The gMEA die is then carefully oriented (with the return electrode to the left side of the PCB [Fig. 3.9 (C)]) and placed in the PCB's opening. Using cleanroom tweezers, the gMEA die is adjusted to maintain a flat alignment with the PCB. Cyanoacrylate superglue is then applied with a needle at each corner of the die-PCB interphase to adhere the two. Once the superglue is applied, the assembly (metal plate with PCB+MEA) is transferred to a hot plate and heated at 80ºC for 15 minutes. Post-baking, the supporting quartz fragment is removed, and the final device is prepared for wire bonding. Figure 3.9 (C) depicts the

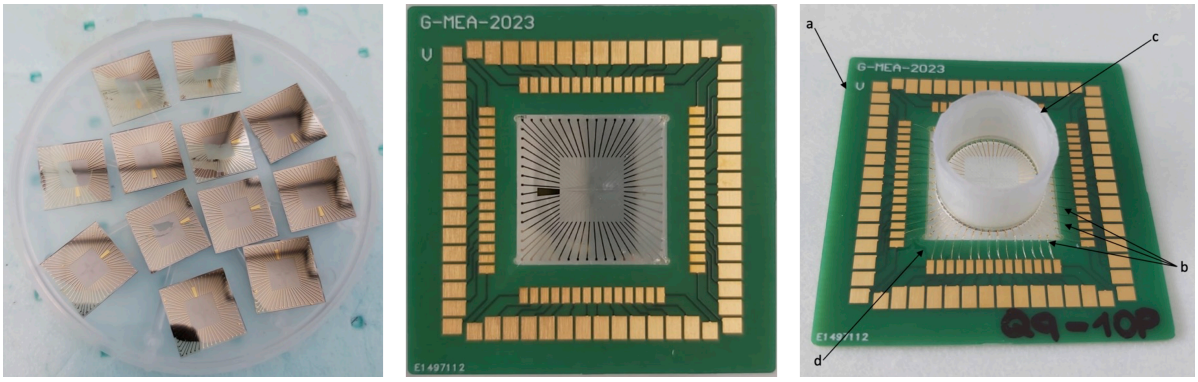

Figure 3.9: Images of devices during fabrication: **Left**: Quartz wafer after dicing. gMEA dies before the removal of sacrificial layers. The dies still have the protective photoresist layer applied before dicing. The transparent regions of the dies are due to the removal of the Ti back layer while peeling off the adhesive film used for dicing. **Center**: Finalised gMEA die attached to PCB. **Right**: Complete device with: **a**: PCB, **b**: wirebonds, **c**: growing well, **d**: protective epoxy coating (seen as shiny areas on the PCB wirebonds and well).

result of this procedure.

3.4.2. Wire Bonding

Wire bonding for the device [Fig. 3.10 (b)] was conducted using the TPT HB05 Au bonder. This process utilised gold (Au) wire with a ball-wedge wire bonding technique. The settings applied for the first and second bonds were 250 and 270 mW of ultrasound (US) power, respectively, coupled with a force of 20 mN for both bonds. The duration of the bonding process was set to 200 ms for the first bond and 225 ms for the second bond.

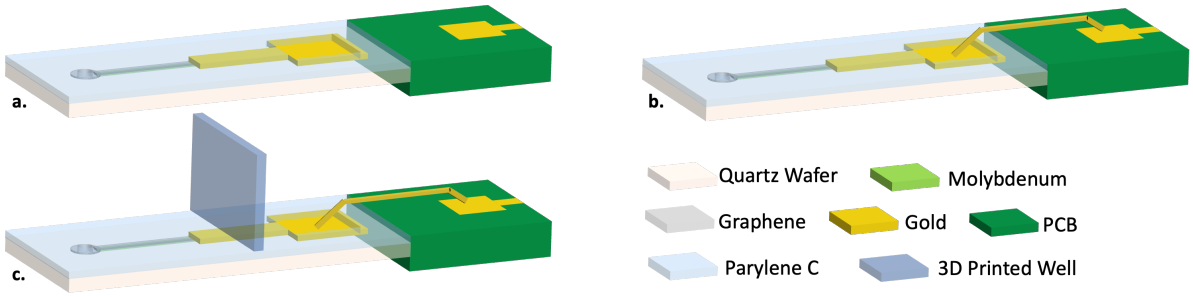

Figure 3.10: Fabrication steps diagram for the completion of the device: **a**: Attachment of the MEA dies to the PCB. **b**: Au ball wire bonding of the MEA contact pads to the PCB contact pads. **c**: Addition of 3D printed growing well.

3.4.3. Growing Well

The growing well, an integral part of the device, was fabricated using a resin 3D printer (Asiga MAX X) with Mollin Tech Clear resin. The wells were designed with an inner diameter of 15mm, a wall thickness of 1mm, and a height of 12mm. After printing, the structures were cured with UV light for a prolonged period to prevent cytotoxic interactions with the cells [119, 120]. The wells were attached to the gMEA [Fig. 3.10 (c)] after the wire bonding process to prevent any epoxy from covering the contact pads before establishing the connections. They were carefully positioned on the device, and EPO-TEK 301-2FL epoxy was dispensed around its outer wall using an epoxy dispenser pump. Enough epoxy was applied to cover the entire outer ring of the well, and additional epoxy was used to coat the wire-bonded connections.

The epoxy curing process was conducted on a hot plate at 80 ºC overnight, with the assembly placed above a metal plate to protect the hot plate surface from any potential epoxy damage. This extended curing period was necessary due to the lower temperature used, a precaution to accommodate the thermal sensitivity of parylene C. A second epoxy coating was applied to ensure complete coverage of all wire bonds.

Post-curing, the wells were filled with DI water to confirm their integrity and readiness for use. After a few minutes, the wells were emptied and air-dried.

3.4.4. Final Device

The completed device is illustrated in figure 3.9 (R). In this image, the gMEA die is centrally positioned on the PCB, with the growing well securely bonded to it. The wire-bonded connections between the contact pads of the die and the PCB are also visible. While the epoxy used for attaching the well and safeguarding the wire bonds might not be immediately apparent, it can be identified by the shiny characteristics around the wire bonds and well, as well as colour variations on the PCB. This final assembly showcases the successful integration of all components into a cohesive unit, ready for its intended applications.

4

Device Characterisation

The gMEA underwent comprehensive characterisation through various methods to assess its properties, performance, and stability. This chapter begins by exploring the characterisation approach for graphene grown on quartz and sapphire, which lead to the substrate selection for the gMEAs. Subsequently, the characterisation procedure for gMEAs is discussed across three sections, focusing on the electrochemical, stability, and biocompatibility assessements. Lastly, the procedures for the main measurements and experiments, performed in the characterisation of graphene and gMEAs, are described.

4.1. Graphene Characterisation

Incorporating graphene into the gMEA is a fundamental aspect of this project. As such, an extensive evaluation of the graphene's properties and its interactions with the in-vitro environment was conducted. This thorough analysis was crucial to gain a more complete understanding of graphene within the device context.

4.1.1. Optimisation of Graphene Growth

In the process of growing multilayer graphene using CVD, three critical variables significantly influence the outcome: substrate material, transition metal, and growth recipe. Mo was selected as the transition metal to avoid the need for transfer steps of the grown graphene onto a desired substrate during fabrication [24]. The high temperatures required for graphene growth limited the substrate choices to quartz/fused silica (SiO_2) and sapphire (Al_2O_3). Therefore, graphene was grown on both substrates using various pre-existing growth recipes to determine the optimal growth conditions for each. For a detailed description of the graphene growth process, refer to the fabrication Section [3.3.2].

Before growing graphene, the wafers with the Mo pattern were diced in the MEMS lab's Disco Dicer using a glass blade at low speed (0.5 mm/s) [Fig. 4.1 (b)], creating samples to test the different recipes. A die from each substrate was used to test each recipe. In total, six recipes were tried: at temperatures of 915 ºC, 935 ºC, and 950 ºC, each with and without a 20-minute pre-anneal treatment. The presence and quality of graphene were assessed using Raman spectroscopy [Section 4.5.1], with the Mo beneath the graphene serving as a backing layer. The optimal recipes for sapphire and quartz were identified as 950 ºC without pre-anneal and 915 ºC without pre-anneal, respectively. For a comprehensive breakdown of the results, refer to Section 5.1. Graphene was grown on the remaining dies using each substrate's optimum recipe, to create samples for additional experiments. Graphene grown on silicon (provided by S. Rice) was also included for comparison with the transparent substrates, as silicon had been the preferred substrate for graphene growth previously. These samples were repurposed from another project, requiring additional processing steps to prepare silicon wafers with only graphene on Mo before manual dicing [Fig. 4.1 (c)].

A key step in making the device transparent involved removing the Mo catalyst beneath the grown graphene [Fig. 4.1 (d)]. For a detailed description of the Mo removal process, refer to Section 3.3.5. The resulting samples were evaluated using Raman spectroscopy to assess the presence and quality of graphene. Si wafers were used as a backing layer for the sapphire and quartz samples. Additionally,

optical imaging [4.5.2] was used to assess the extent of delamination caused by Mo removal, and the general condition of the sample, including broken or damaged structures and particles in unintended locations, such as openings.

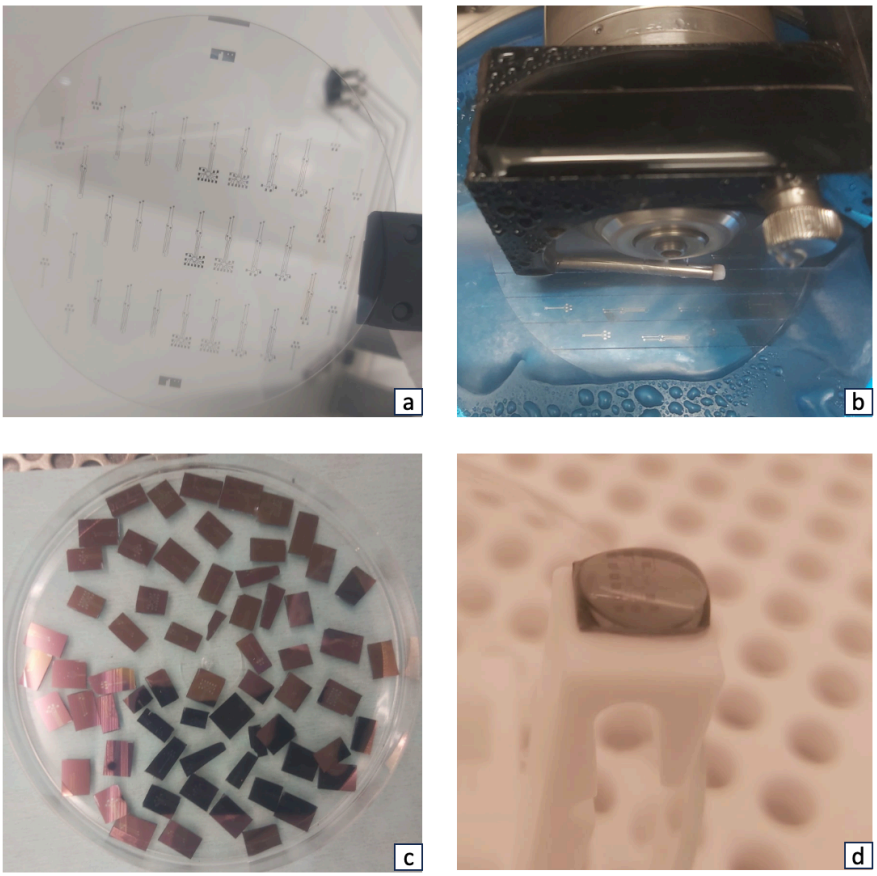

Figure 4.1: Preparation of graphene samples: **a**: Quartz wafer with Mo pattern prior to graphene growth; **b**: Dicing of the sapphire wafer using the Disco Dicer; **c**: Bulk of manually diced silicon samples; **d**: Mo etching process of a silicon sample.

4.1.2. Soaking Test

To further explore the properties of graphene and the substrates, a 12-day soaking test [4.5.6] was conducted. This test simulated the conditions the final device would undergo and assessed the impact on graphene. The aimed at providing insights into the effects of cell culture medium and fibronectin protein on graphene, the adherence of graphene to the substrate, and the influence of the optical dye (Di-4-ANBDQBS from Potentiometric Probes), used in voltage mapping, on graphene.

Prior to the soaking test, some samples underwent sterilisation by soaking in 100% ethanol for 20 minutes. This step verified that the standard ethanol sterilisation procedure [4.5.5] used by LUMC did not adversely affect graphene's properties. Raman spectroscopy [4.5.1] was employed to assess the samples both before and after the sterilisation to monitor their evolution.

For the soaking test, six samples from each substrate (silicon, quartz, and sapphire) with minimal signs of delamination were chosen. However, all samples exhibited some degree of initial delamination. Before the soaking test, these samples were characterised via Raman spectroscopy and optical imaging [4.5.2], and sterilised with ethanol [4.5.5]. Figure 4.2 illustrates the samples during the soak test. At the conclusion of the 12 days, two samples from each substrate were treated with optical dye and incubated at 37ºC for 10 minutes. Following a rinse with DI water and air drying, the material properties of these samples were re-evaluated and compared to the initial measurements.

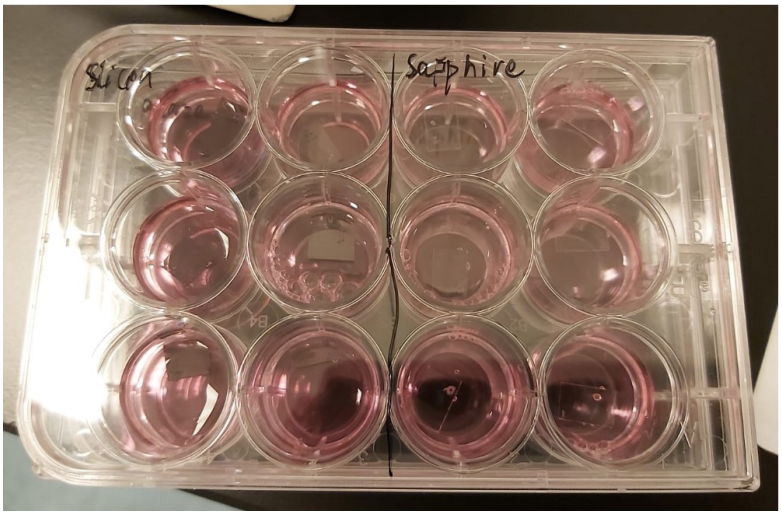

Figure 4.2: Soak test of graphene samples. Petri dish filled with culture medium with the six samples of silicon (left-hand side) and sapphire (right-hand side). The rectangular samples are visible in the centre of the wells.

4.1.3. Graphene Layers

The number of graphene layers grown can be estimated by measuring the OT [4.5.3] of bare graphene at 550 nm. To conduct OT measurements, the sample needs to be sufficiently large, several centimetres in size, to completely cover the aperture in the spectrometer. Consequently, a new sample specifically for this test was created. A 15x15 mm checkerboard pattern of graphene was grown on a quartz wafer at 915 ºC. This wafer was then diced, and the Mo beneath the graphene was etched away [Mo etching described in Section 3.3.5]. The dies without graphene were selected as reference samples for bare quartz. After a 24-hour air drying period, the OT of the samples showing no delamination was evaluated. Additional reference measurements were also taken from the bare quartz samples to compensate for its absorption on the graphene measurements. The compensated OT measurement of graphene at 550nm was used to estimate the number of layers by means of equation 2.3.

4.2. Electrochemical Properties

4.2.1. Electrochemical Impedance Spectroscopy and Cyclic Voltammetry

The devices were evaluated through EIS and CV, using the electrochemical characterisation procedures outlined in Section 4.5.4, to create a comprehensive picture of the device's operational characteristics. To facilitate these assessments, specific modifications were made to the devices, rendering them suitable solely for this testing purpose. Due to the limited number of functional devices, only three were evaluated, testing 16 electrodes from each device individually.

4.2.2. Signal-to-Noise Ratio

The aim of this test was to measure the SNR of the setup, encompassing the amplifier, filters, and electrodes, as well as to evaluate the recording capabilities of the device. The testing was conducted at LUMC using the FM60-AMP Rev.B SerNo. 047 amplifier. Both gMEAs and standard MCS-MEAs, used at LUMC, were assessed.

For the test, the MEA was mounted on the amplifier and the well was filled with PBS. A platinum electrode, linked to an MCS stimulus generator (STG 4002), was placed inside the PBS, attached to the north side (towards the PCB side with printed writing [Fig. 3.9 (c)] and maintaining consistent placement for all tests) of the well rim [Fig. 4.3]. The entire setup was then enclosed in a Faraday cage to eliminate external interference.

Using MCS' stimulating and recording applications, a stimulation was injected into the PBS via the platinum electrode (from the stimulus generator), and the voltages detected by the MEA electrodes were recorded. Seven different stimulation types were tested on each device: no stimulation, and sinusoidal and square stimulation at 1 V, 100 mV, and 10 mV. The sinusoidal signal had a frequency of 10Hz, and the square stimulation consisted of a 10 ms square signal at 1 Hz. For each stimulation type,

approximately 10 seconds of signal were collected. The data was saved as a text file and subsequently analysed in MATLAB to calculate the SNR. The baseline noise level was determined by calculating the root mean square (RMS) of recordings captured without any stimulation applied. For sinusoidal stimulations, characterised by their continuous nature, the signal level was similarly calculated using the RMS value of the entire recording. In contrast, square stimulations, which are discrete and occur at specific intervals, required a different approach. Here, only the segments of the recording during which stimulation was applied were considered. The RMS value for these segments was calculated individually, and then an average was determined for the recording. The SNR for each recording was then calculated by dividing the RMS of the signal, whether from sinusoidal or square stimulation, by the RMS of the baseline noise [2]. This calculation was performed for each electrode within the array independently, with the exclusion of any electrodes that showed evidence of damage or instability. The scripts used for the visualisation and analysis of the recorded data can be found in appendix B and C respectively.

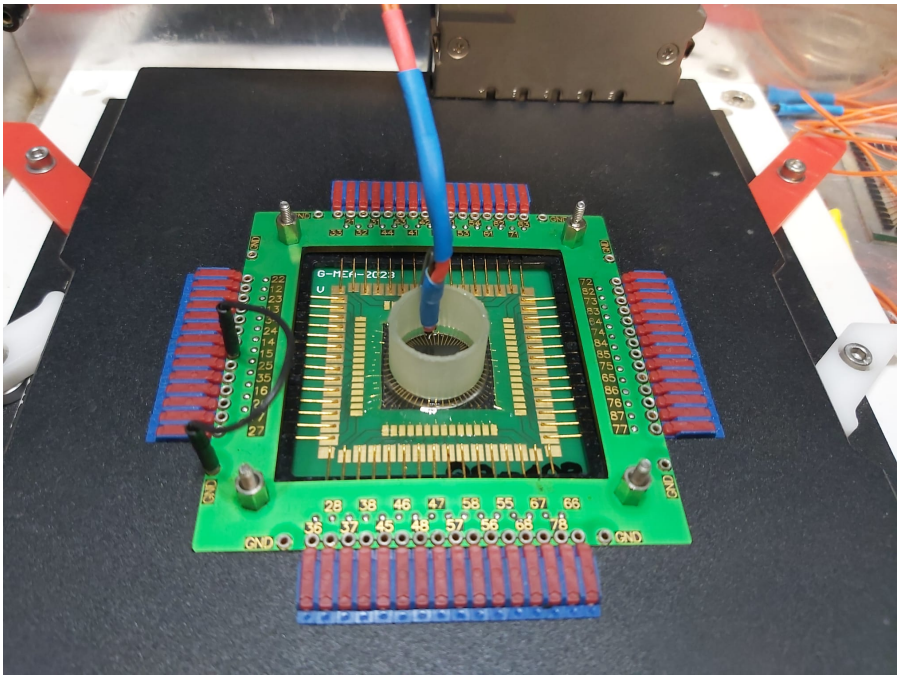

Figure 4.3: Signal-to-Noise Ratio measurement setup. gMEA mounted on the amplifier, with a stimulating Pt electrode immersed in the well's PBS. The gMEA has been sandwiched between the top and bottom plates of the amplifier.

4.2.3. Photoinduced Artifact Test

The purpose of this test was to determine whether light stimulation of the gMEA induces photo-artifacts in the signal. For comparison, a standard MCS-MEA used in Leiden was also included in this experiment.

The setup consisted of the FM60-AMP Rev.B SerNo. 047 amplifier at LUMC, with the MEA mounted in it, and a light source fixed beneath it [Fig. 4.4 (b)]. The light source featured a 470 nm LED (ThorLabs M470L3-C4) attached to a collimation adapter (ThorLabs COP1-A OLYMPUS), intended to create a parallel beam of light [Fig. 4.4 (a)]. The light was directed at the chip from the backside for photo-stimulation [Fig. 4.4 (b)].

Two different experimental setups were employed:

1. One where the light source illuminated the entire die.
2. Another where only the MEA electrodes were exposed to the light source [Fig. 4.4 (d)]. To limit exposure to just the electrodes, a mask made of electric tape was used [Fig. 4.4 (c)]. The MCS-MEAs were tested only with the aperture exposing the electrodes.

The light source's intensity was controlled using a low-noise digitaliser (Axon CNS Molecular Devices Digidata 1440A). The system outputted a voltage to the light source to achieve the desired light intens-

ity. This voltage was manually calibrated using a light sensor (console: ThorLabs PM100D; sensor: ThorLabs S130C) to estimate the light intensity on the MEA for a corresponding voltage.

The MEA's well was filled with PBS solution, and the entire setup was enclosed in a Faraday cage. The experiment was conducted in dark conditions. Initially, the inherent electronic noise of the MEA was recorded without any stimulation, serving as a baseline signal measurement. The MEA was then subjected to five light pulses, each lasting 50 ms at a frequency of 1 Hz and light intensities of 10, 30, and 50 mW/cm^2. This was designed to mimic the conditions under which optogenetic cells are stimulated. The signals were recorded using the MCS recording app and saved as a text file to be plotted and analysed in MATLAB. The data was processed using MATLAB's Fast Fourier Transform (FFT) function (**fft**), and displayed in the time and frequency domain.

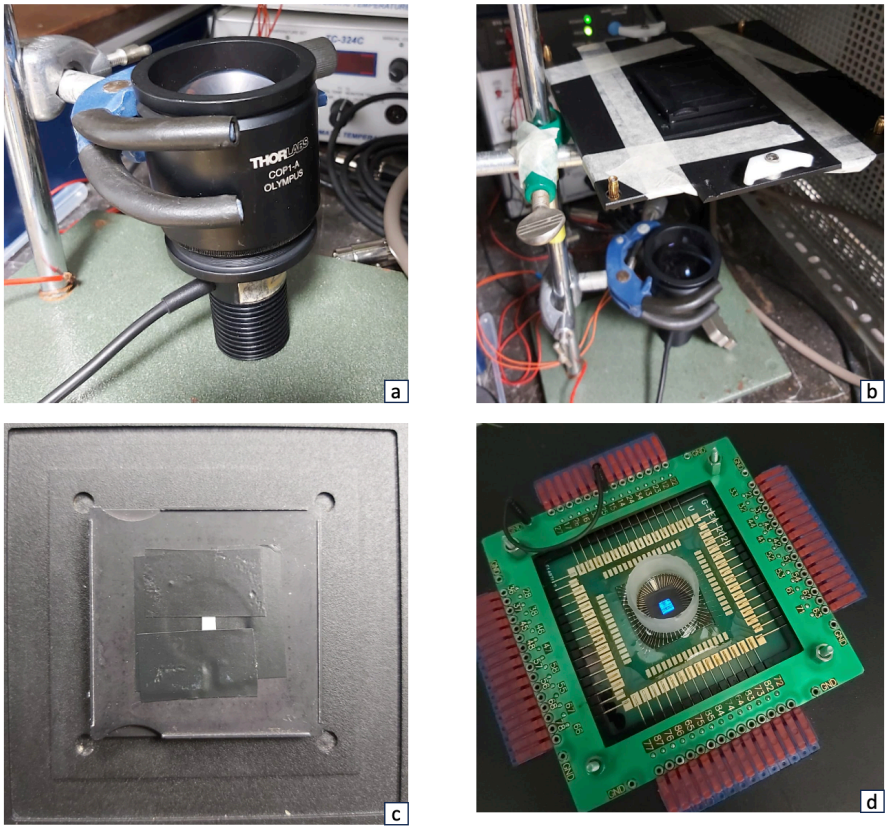

Figure 4.4: Photoinduced Artifact test setup: **a**: 470 nm ThorLabs light source with a ThorLabs collimator adapter. **b**: Lightsource and amplifier back-plate mounted on a stand. **c**: Electric tape mask on the amplifier, used to limit exposure to electrodes. **d**: gMEA mounted on the closed amplifier during limited exposure experiment (region illuminated is visible in the centre of the well).

4.3. Device Stability

The stability of the gMEA is a crucial aspect, particularly considering its prolonged exposure to the in-vitro environment during its functional life. This procedure aimed to evaluate the device's stability and the effects of such an environment on its performance. Prior to the experiments, the devices were characterised using several methods: Raman spectroscopy [4.5.1], optical imaging [4.5.3], OT [4.5.3], EIS [4.5.4], CV [4.5.4], and SNR [4.2.2]. These initial values were later compared to the characterisation measurements taken after the stability tests to identify any significant changes.

4.3.1. Changes in Optical Measurements

The devices were first subjected to an environment that closely simulated in-vitro conditions. The initial step involved sterilising the devices with ethanol [4.5.5], followed by a 2-day soak test [4.5.6] to verify their sterility. Devices showing contamination were excluded from further testing. The uncontaminated

devices were then subjected to a 12-day soak test [4.5.6]. After completion, the devices were re-evaluated using Raman spectroscopy [4.5.1], optical imaging [4.5.2], and OT [4.5.3].

This experimental procedure was conducted twice: initially with dummy devices (which were not suitable for electrical recordings) and subsequently with functional devices. However, during the second round of testing with the working devices, the fibronectin coating was not applied in the 12-day soak test.

4.3.2. Signal-to-Noise Ratio Stability

The assessment of the devices' SNR stability was conducted using the same working devices that underwent the second iteration of the soak test as detailed in the previous Section 4.3.1. Following the 12-day soak test, these devices were evaluated using the SNR procedure described in Section 4.2.2.

4.3.3. Ageing Test

For the ageing test, the same devices previously used to assess the EIS and CV [4.2] were employed. This test aimed to identify the potential failure mechanisms of the device over time. The wells of the devices were filled with PBS and sealed with a 3D printed cap made using a resin printer (Asiga MAX X) with Mollin Tech Clear resin. The samples were placed in a petri dish and incubated in a temperature cycling test chamber (Tenney by Thermal Product Solutions) set to 67ºC [87, 88].

Throughout the test, at intervals of a few days, the samples underwent re-evaluation through optical imaging [4.5.2], OT [4.5.3], EIS [4.5.4], and CV [4.5.4]. Each time, their PBS solution was replaced before they were returned to the incubator. The experiment spanned a total duration of 10 days.

4.4. Device Biocompatibility

This procedure is designed to evaluate whether the materials used in the device exhibit any cytotoxic effects on cell lines. The assessment involved growing cell lines on the devices and then analysing the cells for viability, metabolic activity, and behavioural patterns. Before beginning the experiment, the devices were characterised through optical imaging [4.5.2], OT [4.5.3], and their SNR [4.2.2] was measured. After the completion of the biocompatibility tests, the devices were re-characterised to detect any changes in the properties of the device and materials.

4.4.1. Cardiomyocyte Growth

The biocompatibility assessment was conducted at LUMC, where hiAM-CheRiff cell lines were cultivated inside the growing wells of the devices. Before seeding the cells, the devices were sterilised using ethanol [4.5.5]. To confirm the sterility of the devices, they underwent a 2-day soak test [4.5.6]. Any devices showing contamination were excluded from the experiment. The wells of the remaining devices were filled with a fibronectin solution (Fibronectin (1mg/ml) Sigma-Aldrich - F1141) and incubated for 10 minutes at 37ºC. After discarding the fibronectin solution, the wells were filled with a cell differentiation medium (details in [121]) containing the cells. The devices were placed in an incubator set at 37ºC, 5% CO_2, and approximately 100% humidity, for a duration of 12 days, with the culture medium being replaced every two days. After 7 days, the cell cultures were inspected for any issues such as infection or device damage. The gMEAs with cell cultures were divided into two groups: one for the biocompatibility testing and the other for generating voltage maps of the cells.

4.4.2. Biocompatibility Test

Following the maturation of the cardiomyocytes, we evaluated their morphology using optical microscopy, a key indicator of cell health. Following this, we conducted a viability assay to differentiate between living and non-living cells. Typically, this process involves using trypan blue dye, which dead cells assimilate due to their compromised membrane selectivity, allowing for their identification through optical means. Despite its simplicity and cost-effectiveness, this method has limitations. For instance, living cells can uptake the dye after a short exposure, and the technique may yield inaccurate results following certain cell treatments [122, 123]. Additionally, it struggles to differentiate between healthy cells and those beginning to lose function, reducing its sensitivity for in-vitro cytotoxicity evaluations [124].

Given the need for a more consistent and reliable method to assess cytotoxicity in our study, we opted for fluorescent marker staining, a superior alternative [125]. Specifically, we used fluorescein di-

acetate (FDA) and propidium iodide (PI) for staining [125–127]. FDA permeates cell membranes easily and once inside it is hydrolysed into fluorescein (which emits bright green fluorescence) and accumulates within cells that maintain an intact plasma membrane. Conversely, PI, which cannot penetrate healthy cell membranes, enters and binds to the DNA and RNA of dead or dying cells, producing a bright red fluorescence. This staining approach allows us to identify metabolically active healthy cells (FDA positive and PI negative), dying but still active cells (both FDA and PI positive), and dead cells (FDA negative and PI positive) [125–128].

We then analysed the distribution and concentration of these markers across cells using a phase contrast microscope. This analysis enabled the calculation of the ratio of viable to non-viable cells.

4.4.3. Cell Death Assessment

The ratio of viable to non-viable cells obtained from the biocompatibility test was compared to the viability ratios documented in other experiments involving hiAM-CheRiff cell lines grown on MCS-MEAs. Should there be a notable decrease in cell viability in gMEAs compared to standard MCS-MEAs, a detailed cell death assessment procedure was to be performed.

For this procedure, additional remaining cell samples were treated with fluorescent markers PI and Annexin V (AN). AN is particularly useful for identifying early cell apoptosis, as it binds to phosphatidylserine, a phospholipid that becomes exposed on the outer layer of cell membranes during the initial stages of apoptosis. However, since AN itself does not fluoresce, it must be coupled with a fluorescent marker, such as fluorescein isothiocyanate (FITC), to enable its detection during cell labelling. Through the strategic use of PI and Annexin V, we can categorise cells into four distinct groups: healthy cells (AN and PI negative), cells undergoing early apoptosis (AN positive and PI negative), necrotic or dead cells (AN and PI positive), and cells that are either necrotic, in late stages of apoptosis, or with highly damaged cell membranes (AN negative and PI positive) [129–131].

We then examined the concentration and distribution of these markers within the cells using a phase contrast microscope. This step was crucial to determine whether the cause of cell death was due to material cytotoxicity (necrosis) or natural death (apoptosis) [129–131].

4.4.4. Voltage Mapping of Cell Lines

This experiment was designed to verify that the electrical activity of the cells is within normal parameters and to evaluate the quality of recordings and the efficacy of optogenetic stimulation using the gMEA. All remaining cell samples were utilised for this final test.

Initially, the cells were treated with optical dye (Di-4-ANBDQBS from Potentiometric Probes) and incubated for 10 minutes at 37 ºC. The optical dye was then washed off and replaced with fresh culture medium before commencing the experiment. The gMEAs, with the treated cells, were mounted on the LUMC amplifier (FM60-AMP Rev.B SerNo. 047). The amplifier and gMEA setup was placed on a hot plate under the lens of the optical voltage mapping system (SciMedia - miCAM ULTIMA-L), with a micro LED array (450 nm wavelength) positioned beneath the gMEA and a platinum electrode immersed in the PBS and attached on the north side of the well (electrode attachment described in Section 4.2.2). The cells were stimulated using the micro LED array and platinum electrode alternately, applying a square stimulation of 50 ms at a frequency of 1 Hz. The light intensity for photo-stimulation, often around 30 mW/cm^2, was predetermined. The responses of the cells were captured through both the gMEA and the optical setup.

4.4.5. UV Sterilisation

Following unexpected contamination issues during the 12-day growth period in the biocompatibility test [4.4.1], alternative sterilisation methods were considered. UV sterilisation, a straightforward and accessible option at LUMC, was evaluated for its efficacy and impact on the devices. Dummy devices, which were not suitable for electrical recordings, were used in this experiment.

The devices were characterised using optical imaging [4.5.2] and OT [4.5.3] before UV exposure. The Vilber Lourmat static UV steriliser at LUMC was used to expose the devices to various UV radiation dosages, each delivering 9.999 J/cm^2. Post-treatment, some samples were returned to TU Delft, while others underwent a 2-day soak test [4.5.6] to assess sterility. Following the soak test, the devices were rinsed, air-dried, and brought back to TU Delft, where they were re-evaluated alongside the other samples through optical imaging and OT. This process aimed to detect any changes caused by UV sterilisation.

4.5. Measurements and Experimental Procedures

4.5.1. Raman Spectroscopy

Raman spectroscopy was conducted in the ESP Lab of TU Delft using a Renishaw inVia Raman Microscope. The process utilised a 514 nm wavelength laser (Modu-Laser Stellar RMN) as the light source. To ensure stability, the laser was activated 30 minutes before measurements. It was crucial to verify that the microscope was equipped with the green light laser lens, not the red one, before mounting the sample on the microscope table. Transparent samples were placed atop a silicon wafer, acting as a backing layer to reflect the incident laser. The microscope's focus was methodically adjusted from the lowest to the highest magnification, culminating with the x100 magnification objective. Subsequently, the laser shield was closed, and room lights were turned off to eliminate light leakages. The microscope light was then switched off, and the laser shutter opened to expose the sample. The laser's focus and power were carefully adjusted to achieve the smallest possible focal point with minimal power while keeping the laser focal point visible. Once the sample setup was complete and ready for measurement, it was scanned using an extended grating mode, capturing a Raman Shift range from 1100 to 3200 $cm^{-}1$. The chosen acquisition parameters were a 30-second exposure time and 50% laser power. Upon completing the measurement, the data was saved as a text file and subsequently plotted and analysed using MATLAB with a modified version of the script developed by S. Vollebregt et al. [132].

4.5.2. Optical Imaging

Optical microscopy inspections were conducted using a KEYENCE microscope (VHX-7000 Series), equipped with two lenses capable of providing magnifications ranging from x20 - x200 and x200 - x2000, respectively. Following standard operating procedures for microscope use, images of structures deemed important or interesting were captured and saved in jpg format for future reference. The microscope's software offered various image enhancement tools to assist in structure visualisation, which were utilised based on the specific requirements of the samples being imaged.

4.5.3. Optical Transmittance

OT measurements were performed using a Perkin Elmer Lambda 1050+ UV/VIS/NIR Spectrometer in the ESP lab. To ensure a stable light source, the light source was activated 30 minutes before commencing measurements. Transmittance data was collected across wavelengths ranging from 300 to 1200 nm, at 5 nm intervals. For these measurements, the sample was oriented with its front side facing the integrating sphere and the backside towards the light source. The resulting data was outputted as csv files and subsequently plotted in MATLAB.

4.5.4. Electrochemical Characterisation

Device Preparation

Before electrochemical characterisation, wires were soldered to the PCB contact pads of the devices, corresponding to the electrodes intended for assessment [Fig. 4.5 (arrow a)]. This step ensured robust contact between the crocodile clamps of the potentiostat setup and the device [Fig. 4.5 (arrow b)].

Experimental Setup

Electrochemical characterisation measurements were conducted using an Autolab MetrOhm PGSTAT302N potentiostat, with the gMEA placed inside a Faraday cage (Metroohm Autolab B.V.). The setup, depicted in figure 4.5, was arranged in a three-electrode configuration. It included a growing well filled with PBS, sealed with a 3D-printed cap [Fig. 4.5 (arrow c)]. To prevent leakages via capillary action between the cap and the well, a layer of Parafilm was placed between the two [Fig. 4.5 (arrow d)]. The cap had two openings for inserting the counter electrode (Platinum, 3mm diameter, MF-2113 from BASi) [Fig. 4.5 (arrow f)], and the reference electrode (Ag/AgCl, ET072 from eDAQ) [Fig. 4.5 (arrow g)]. The counter electrode was positioned near the PBS surface, approximately at the well's height from the gMEA electrodes. The reference electrode was inserted closer to the gMEA electrodes without making contact. The cap's orientation for the counter electrode opening was always northward (towards the PCB side with the "G-MEA-2023" marking), as shown in figure 4.5. The gMEA electrode under testing was connected to the potentiostat as the working electrode via the soldered wire. The Faraday cage was closed to finalise the setup.

After each measurement, the connection to the working electrode was switched to another gMEA electrode, and the process was repeated for all electrodes.

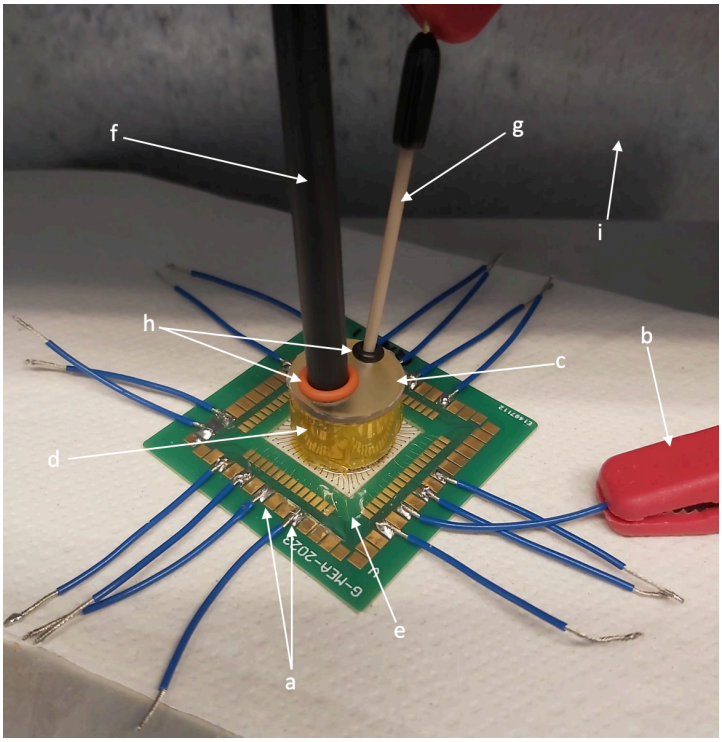

Figure 4.5: Experimental setup for electrochemical characterisation: **a**: Cables soldered to PCB contact pads; **b**: Crocodile clamps to connect electrodes to potentiostat; **c**: 3D printed cap holder for the reference and counter electrodes; **d**: Kapton tape to seal the cap to the well and prevent PBS leakages (replaced with Parafilm in later experiments); **e**: Epoxy resin (not PBS); **f**: Counter electrode (Pt); **g**: Reference electrode (Ag/AgCl); **h**: Rubber bands to keep electrodes inserted at fixed depth; **i**: Wall of the Faraday cage

Electrochemical Impedance Spectroscopy

For EIS, the ”Cyto2.0EIS” program of the potentiostat was utilised. A sinusoidal voltage of 10mV RMS was injected between the Working Electrode (WE) and the Counter Electrode (CE), and the current between the WE and the Reference Electrode (RE) was measured. EIS data was gathered over 50 frequencies, ranging from 1 Hz to 100 kHz in logarithmic steps, and then saved as a text file for analysis and plotting in MATLAB. The EIS analysis involved extrapolating the recorded data through the MATLAB function **interp1** to estimate the impedance at 1 kHz, employing a linear interpolation method.

Cyclic Voltammetry

CV was performed using the ”Cyclic Voltammetry Linear Scan” program of the potentiostat. The potential range for CV was set between -0.8 and 0.6 V. This corresponds to the water window of graphene used by Bakhshaee et al. in the characterisation of multilayer CVD graphene electrodes, produced in a similar manner to ours [43]. Following the protocol used by Bakhshaee et al. [43] and Rice [133] for comparability, CV measurements were taken at scan rates of 0.1, 0.2, 0.6, and 1 V/s. The data collected was saved as a text file to be plotted and analysed in MATLAB. The total and cathodic charge storage capacity (CSC) was measured using the **trapz** MATLAB function to calculate the enclosed area.

4.5.5. Ethanol Sterilisation

This standard ethanol sterilisation procedure is practised at LUMC. Materials were placed in a laminar flow bench and soaked in 70% ethanol for 20 minutes. Following this, the ethanol was discarded, and the materials were left to air dry within the laminar flow bench.

4.5.6. Soaking Test

The soaking test is intended to expose the samples to the cell culture environment without the presence of cells, to investigate its effects on the samples. Before conducting the soaking test, samples underwent characterisation using Raman spectroscopy and optical imaging. In some cases, additional characterisation was carried out on the samples. The procedure was conducted on a laminar flow bench at LUMC, sterilising the samples with ethanol before the start. Initially, the samples were coated with a Fibronectin solution (1 mg/ml Fibronectin, Sigma-Aldrich - F1141) and incubated for 10 minutes at 37 ºC. After discarding the remaining Fibronectin solution, the samples were immersed in differentiation medium (details in [121]) and placed in an incubator for 12 days at 37 ºC, 5% CO_2, and approximately 100% humidity.

After 7 days, an initial assessment of the samples was conducted to check for contamination and other irregularities. On the 12th day, the samples were rinsed with DI water and air-dried. They were then re-characterised and compared to the initial measurements to detect any changes in properties.

To ensure sterility post-sterilisation, a shortened, 2-day version of the soaking test was implemented. This simplified protocol omits the fibronectin coating stage, directly filling the growth well with differentiation medium. The device was then incubated under the same conditions. After the 2-day period, samples were examined with an optical microscope to check for any signs of contamination, including bacterial or fungal. Typically, most bacterial and fungal contaminants become detectable under optical microscopy within the first days, allowing for early identification of contamination before proceeding with further experimental steps [134].

5

Results and Discussion

In this chapter, we present the results and discussion surrounding the characterisation of graphene and gMEAs. Initially, we identify the optimal graphene growth parameters for quartz and sapphire and evaluate the resistance to different environmental conditions, leading to the selection of quartz as the preferred substrate. Subsequently, we explore the outcomes from the gMEA, examining its performance in culture medium, its SNR, and physical integrity through optical assessments. We also assess the device's durability through ageing tests, noting changes in EIS measurements and physical appearance. Lastly, we address the unsuccessful attempt to culture cells on the device due to contamination.

5.1. Substrate Selection

5.1.1. Parameter Optimisation

All graphene samples produced using various CVD parameters were assessed via Raman spectroscopy to confirm the presence of graphene above the Mo surface and characterise it. Each sample exhibited the characteristic three peaks in the Raman spectra: the D peak at $\sim 1357.26 \pm 6.12 cm^{-1}$, the G peak at $\sim 1590.96 \pm 3.61 cm^{-1}$, and the 2D peak at $\sim 2718.93 \pm 27.41 cm^{-1}$, as shown in Fig. 5.1. These peak locations are consistent with those reported in literature [49–51].

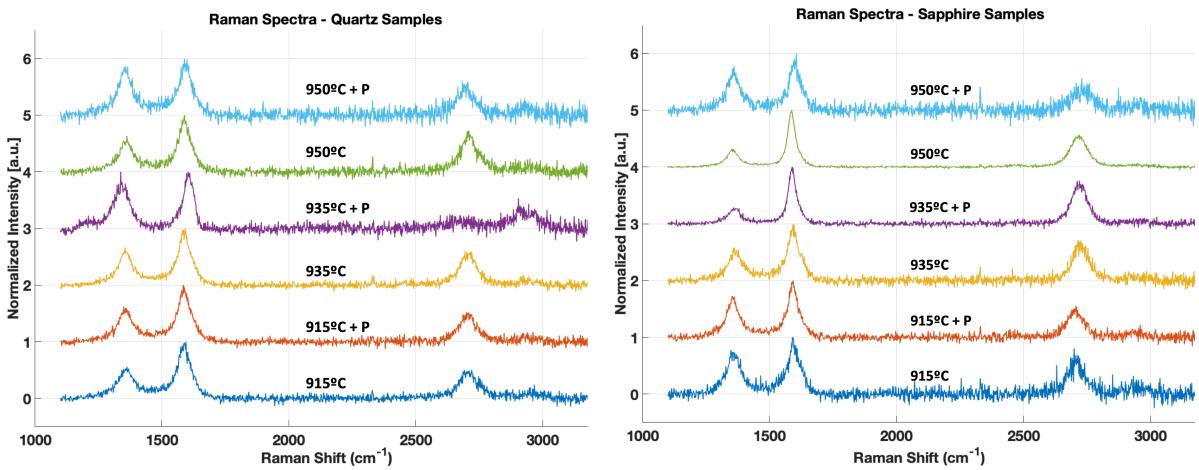

Figure 5.1: Raman spectra of graphene samples for substrate selection. P stands for "Pre-anneal". **Left**: Graphene samples on quartz. **Right**: Graphene samples on sapphire.

For the spectral analysis, we used a modified version of the MATLAB code developed by Vollebregt et al. [132]. This code quantified the spectral properties by fitting three Lorentzians to the peaks. The properties are then used in the assessment of the samples. Notably, the ratio of the intensities of the 2D peak to the G peak (I_{2D}/I_G) is inversely proportional to the number of graphene layers [53]. This ratio serves as an indicator of monolayer (> 1) or multilayer (< 1) graphene. Another marker for the

presence of multilayer graphene is the FWHM of the 2D peak, which increases with increasing layer count [135]. Since all of our samples exhibited I_{2D}/I_G ratios < 1 [Tbl. 5.1] and 2D peak FWHM values $\sim 75cm^{-1}$, which is $\sim$ 3 times that of monolayer graphene [136], we concluded that our samples were comprised of multilayer graphene. Furthermore, the fitting of the 2D peaks was achieved by a single Lorenzian. This implies the produced graphene is turbostratic, meaning its layers are rotated relative to each other [136, 137].

Additionally, the ratio of the intensities of the D peak to the G peak (I_D/I_G) provides insight into the number of defects present in the samples. A higher I_D/I_G ratio indicates more defects, which could result from contamination, disorder, or physical imperfections [49]. We used both the I_D/I_G ratio and the level of noise in the Raman spectra to determine the optimal CVD parameters. For samples on quartz substrates, the best graphene quality was achieved at a temperature of 915 ºC. In contrast, for sapphire substrates, optimal results were obtained at 935 ºC with a 20 min pre-annealing step (935 ºC + P) [Tbl. 5.1]. However, we chose the 950 ºC recipe for sapphire due to its lower spectral noise level, as evidenced in Fig. 5.1 (R). Overall, our findings indicate that the sapphire substrates yielded a higher quality of graphene. Nonetheless, the achieved quality in both substrates is lower than that reported in similar studies [43, 67, 133].

		915ºC	915ºC + P	935ºC	935ºC + P	950ºC	950ºC + P
Quartz	I_D/I_G	0.52	0.6	0.62	0.86	0.57	0.89
	I_{2D}/I_G	0.49	0.53	0.61	0.15	0.7	0.54
Sapphire	I_D/I_G	0.83	0.72	0.55	0.27	0.3	0.79
	I_{2D}/I_G	0.67	0.52	0.73	0.74	0.57	0.44

Table 5.1: Raman ratios for substrate selection

5.1.2. Graphene Characterisation

New samples produced using the identified optimal parameters for quartz and sapphire, respectively, were used to investigate the effects of different processes and environments.

Raman Spectroscopy

This section of the study first examines the impact of Mo removal on the Raman spectrum of our graphene samples. We observed a notable reduction in noise within the spectrum post-Mo removal, suggesting that the Mo backing layer interferes with the signal. Additionally, there was an observed decrease in the I_D/I_G ratio. However, this decrease is likely attributable to the Mo's influence on the signal rather than an actual enhancement in the graphene's quality.

A key observation following Mo removal was the emergence of additional peaks in the spectrum, specifically at $\sim$ 1175, 1408, 1450, and 1509 cm^{-1}, as illustrated in Fig. 5.2 (UL and UR). Although the exact nature of these substances could not be definitively identified, the peaks are characteristic of carbon compounds [138–140]. We hypothesise that these are likely by-products of the graphene growth process, which became evident once the Mo was removed. Moreover, an additional peak was noted beyond the 2D peak at the higher end of the spectrum, identified as the D+D' band. This band is typically present in graphene samples with defects [49, 51].

To assess the durability of the samples, particularly their ability to withstand sterilisation, we soaked them in 100% ethanol for 20 min and then reassessed them. Post-sterilisation, the Raman spectra indicated a reduction in the residues identified after Mo removal, marked by the disappearance of the extra peaks [Fig. 5.2 (UR)].

Furthermore, the samples underwent a soaking test in cell differentiation medium. Post-test, the Raman spectra revealed an increased inter-valley intensity between the D and G peaks [Fig. 5.2 (LL)], commonly associated with an increased number of defects in the sample. This increase, along with a widening at the base of these peaks, may be attributed to the fibronectin coating applied over the graphene, as some of its reported peaks coincide with this region [141]. This pattern was also noted in 4 of the 18 samples that exhibited contamination signs during the test.

In a supplementary examination, 2 samples from each substrate type were incubated with optical dye for 10 min following the soak test. The Raman spectra of these dye-incubated samples shared similar features with the other samples, with the addition of a distinctive depressed peak at $\sim$ 1166

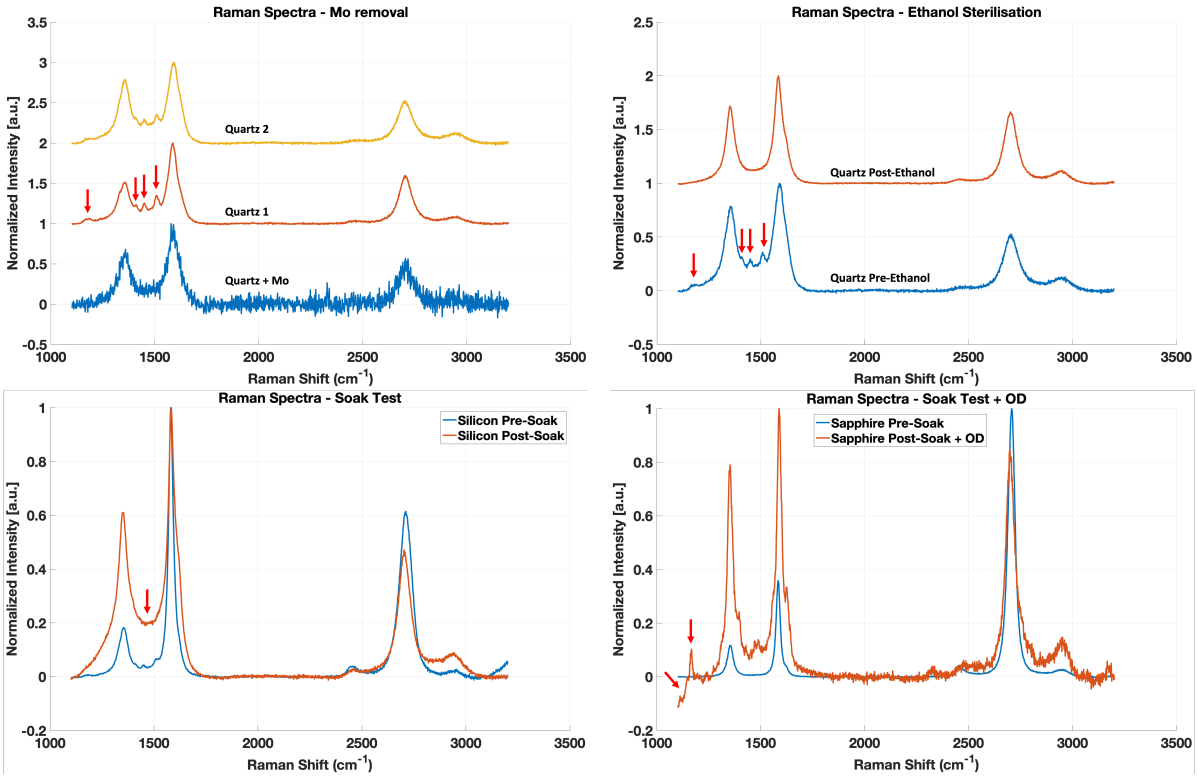

Figure 5.2: Raman spectra of graphene samples during soaking test experiments. **Upper left**: Graphene samples on quartz with and without the Mo backing layer. Indicated with red arrows are the visible extra peaks that indicate the presence of residues. **Upper right**: Graphene sample on quartz before and after soaking in 100% ethanol. Red arrows point to the extra peaks that indicate the presence of residues. **Lower left**: Graphene sample on silicon before and after soak test. The red arrow points to the valley between the D and G peaks, where the increase in intensity occurs after the soaking test. **Lower right**: Graphene sample on sapphire before and after soaking test with the additional treatment of optical dye (OD). The red arrows point to the peak and depression features observed in the spectra of samples treated with OD.

cm^{-1}. This peak is likely characteristic of the optical dye used, confirming its presence in the samples [Fig. 5.2 (LR)].

Optical Microscopy

Before and after conducting the tests, we used optical microscopy to image the graphene samples. This enabled us to closely observe any changes in the graphene structures.

Among the various steps in our experiment, the Mo removal process was found to be the most detrimental to the graphene's structural integrity. The absence of supporting structures during this step made the graphene especially prone to delamination and wrinkling, as evidenced in Fig. 5.3. From all the substrates we tested, graphene on silicon with SiO_2 demonstrated the highest resilience, showing minimal damage, typically limited to small areas of delamination in a few samples. This was followed by quartz, with sapphire substrates showing the most damage (complete delamination of structures), present in most samples. Interestingly, the graphene structures exhibited no significant changes after undergoing ethanol sterilisation or the soaking test.

5.1.3. Choice of Substrate

When comparing graphene grown on quartz and sapphire substrates under the identified optimal conditions, we observed similar behaviors in both when exposed to the testing environments. However, a key distinction was noted in the Mo removal process. Graphene on sapphire substrates experienced more severe delamination compared to that on quartz substrates. Taking into account this difference, along with the cost factor, quartz emerged as the preferred substrate for our application.

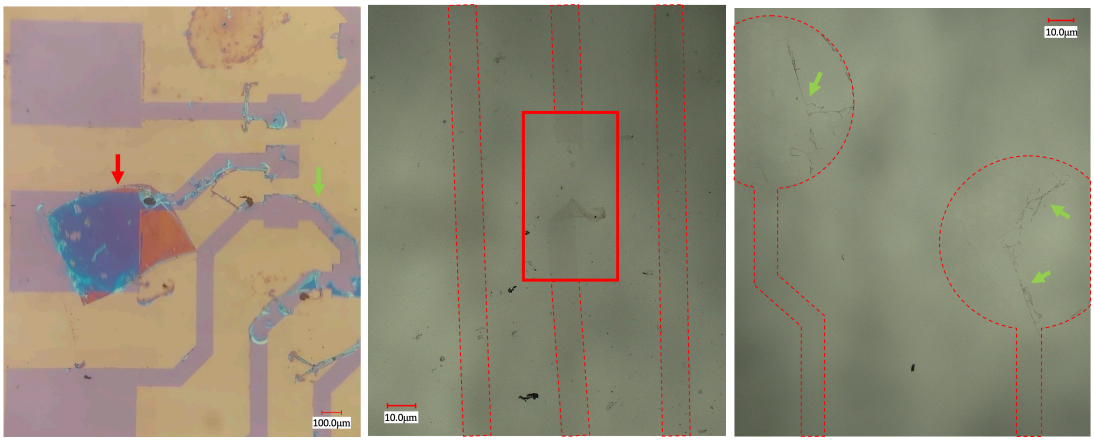

Figure 5.3: Damage to graphene structures after Mo removal. **Left**: Graphene on silicon, where we achieve the best visibility of the structures. The red arrow points to the delamination of a graphene structure, and the green arrow points to a structure that wrinkled and wrapped on itself. **Center**: Graphene on quartz. The central track broke and delaminated (inside the red square). **Right**: Graphene on sapphire. Electrode structures wrinkled and wrapped on themselves pointed at with green arrows.

5.1.4. Graphene Layer Estimation

Utilising the optimised parameters and the chosen quartz substrate, we fabricated 15x15 mm graphene samples to determine the number of layers. To achieve this, OT measurements were taken for two of the graphene samples, along with a bare quartz die as a reference. Each of these was measured twice.

The estimation of the graphene layers was carried out using the method outlined in Section 2.2.3. This method involves the use of the OT values of the graphene samples at 550 nm [Fig. 5.4]. To accurately determine the OT of the graphene, we accounted for the influence of the quartz substrate. This was done by adding the substrate's average absorbance at 550 nm to the OT values of the graphene. Based on this approach, we estimated that the samples consisted of $\sim 10.24 \approx 10$ layers [Tbl. 5.2].

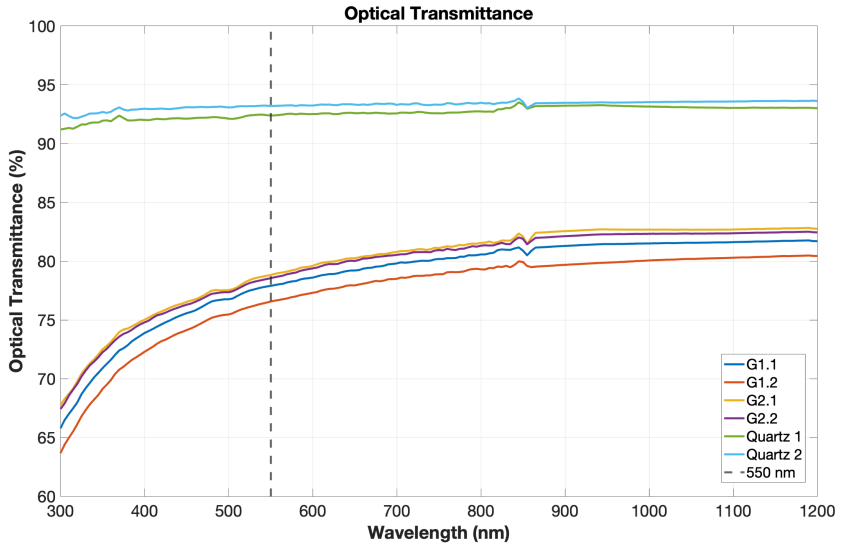

Figure 5.4: Optical transmittance of graphene and quartz for graphene layer estimate.

5.2. Device Characterisation

Upon completion of the MEAs, the presence of graphene on the electrodes was verified using Raman spectroscopy, where the three characteristic graphene peaks were visible.

Absorbance of Quartz at 550 nm	Raw Graphene OT at 550 nm	Compensated Graphene OT at 550 nm	Layer Estimate
Average OT: 92.79±0.57%	G1.1: 77.9% G1.2: 76.57% G2.1: 78.82% G2.2: 78.55%	G1.1: 85.11% G1.2: 83.78% G2.1: 86.03% G2.2: 85.76%	G1.1: 10.27 G1.2: 11.02 G2.1: 9.75 G2.2: 9.90
Absorbance: 7.21±0.57%			Average: 10.23±0.57

Table 5.2: Graphene layer estimate.

5.2.1. Soaking Test

The soaking test was carried out in two iterations: the first on sample devices unsuitable for electrical measurements, and the second on functional devices whose SNR was also assessed. The results from both tests are discussed collectively in this section. Throughout the testing period, none of the devices showed signs of contamination.

Optical microscopy examinations revealed partial degradation of the Mo layer beneath the graphene structures [Fig. 5.5 (U)]. This degradation was more pronounced near the electrodes at the centre, whereas remnants of Mo were still visible further from the centre. Notably, Mo degradation extended to areas beyond direct exposure through the parylene C layer's openings [Fig. 5.5 (LL - numbers)], indicating the material's permeability to the differentiation medium. Thus, the Mo layer's degradation can be attributed to its biodegradability [142, 143] and the encapsulation layer's permeability.

Additionally, the appearance of darker [Fig. 5.5 (LR)] and blue [Fig. 5.5 (LL)] regions around the Mo structures beneath the parylene C were observed, often accompanied by crystal formations [Fig. 5.5 (LL - green arrow)]. These changes are likely due to the leaching or accumulation of Mo trioxide (which forms blue crystals) and other molybdate ions at the degradation sites [142–144].

The changes observed in OT measurements of the devices after the soak test indicated an increase in transmittance across all monitored wavelengths by $\sim$ 3-4% [Fig. 5.6]. This aligns with the findings observed during the optical microscopy examination, owing to the degradation of the Mo layer.

Furthermore, a sinusoidal pattern can be seen in the spectra [Fig. 5.6]. This is attributed to the optical properties of parylene C, which cause constructive and destructive interference in characteristic absorption bands [145]. It is important to notice that the OT measurements of the devices were not performed in a standard manner. Due to the size of the growing well, the sample stood 12 mm away from the device opening [Fig. 5.7]. Thus, the OT measurements are only indicative of the OT of the samples and cannot be used as an absolute OT measurement.

The device's sensing capabilities were evaluated by measuring the SNR of the electrodes before and after the soaking test. The SNR was calculated as the ratio of the RMS of the signal with respect to the RMS of the baseline noise (details of the calculation can be found in Section 4.2.2). Tables 5.3, 5.4, and 5.5 present the average RMS of the baseline noise and signals acquired from sinusoidal and square waveform stimulations, measured in μV. Similarly, tables 5.6, 5.7, and 5.8 present the average SNR, in arbitrary units (a.u.), for 1 V, 100 mV, and 10 mV amplitude stimulations, respectively. Damaged and unstable electrodes were excluded from the calculations, therefore, the number of electrodes used for each average is specified alongside the value.

Prior to the soak test, the devices exhibited an average baseline noise of $\sim$ 23 μV. While this level of noise does not significantly affect the detection of higher amplitude signals, it notably interferes with or completely masks lower amplitude signals, as evidenced by the low SNR of the 100 mV and 10 mV stimulation recordings. As expected, the higher amplitude stimulations yielded larger RMS values and subsequently higher SNR values as well. However, variations were observed between waveforms, with sinusoidal signals surpassing square signals at 1 V amplitudes, and square signals exceeding sinusoidal signals at 100 mV amplitudes. In contrast for 10 mV amplitudes, both waveforms had similar values, but they approached or fell below the baseline noise level, resulting in an SNR close to or below 1, which is insufficient for signal detection.

Significant variability was observed for RMS (and corresponding SNR) values within the same MEA and across different devices. Since the placement of the stimulating electrode was consistent throughout the experiment, the discrepancies are primarily attributed to fabrication defects, such as inhomo-

	Noise RMS [μV]		
Devices	Run 1	Run 2	Run 3
Q9-2OP	17.04±2.88 (Av.54)	7.73±2.02 (Av.52)	9.2±3.4 (Av.51)
Q9-3OP	36.93±12.76 (Av.45)	8.01±2.39 (Av.49)	9.92±5.88 (Av.50)
Q9-4OP	18.16±4.16 (Av.46)	9.42±2.59 (Av.48)	
QN-2	26.57±9.21 (Av.20)	11.49±4.5 (Av.53)	12.48±3.45 (Av.45)
QN-3		16.2±8.23 (Av.36)	11.82±4.64 (Av.42)
QN-4		22.97±11.92 (Av.27)	68.83±32.41 (Av.29)

MCS1	4.33±5.4 (Av.54)
MCS2	3.96±3.5 (Av.52)
MCS3	3.69±2.2 (Av.46)

Table 5.3: RMS of baseline noise of the tested devices. Colour cells indicate measurement was taken after: 2-day (green), 4-day (pink), and 12-day (blue) soak tests, or white if no treatment was applied. Every cell provides the RMS of the baseline noise in the form [average±SD (number of electrodes used for the average and SD)]. MCS 1-3 are the MultiChannel Systems MEAs.

	Signal RMS (sine) [μV]								
	Run 1			Run 2			Run 3		
Devices	1 V	100 mV	10 mV	1 V	100 mV	10 mV	1 V	100 mV	10 mV
Q9-2OP	1257.32± 179.48 (Av. 54)	40.94± 9.93 (Av.54)	19.01± 5.87 (Av.54)	196.11± 127.68 (Av.52)	13.96± 5.31 (Av.52)	8.22± 2.26 (Av.52)	435.28± 142.73 (Av.51)	15.18± 4.45 (Av.51)	7.97± 2.58 (Av.51)
Q9-3OP	310.01± 128.36 (Av. 45)	32.33± 5.57 (Av.45)	18.19± 3.32 (Av.45)	383.25± 424.43 (Av.49)	26.52± 31.63 (Av.49)	9.22± 2.9 (Av.49)	494.15± 385.41 (Av.50)	22.64± 26.41 (Av.50)	8.91± 2.86 (Av.50)
Q9-4OP	1134.14± 202.45 (Av.46)	41.8± 9.16 (Av.46)	19.51± 4.28 (Av.46)	127.57± 32.38 (Av.48)	12.29± 3.39 (Av.48)	10.86± 2.99 (Av.48)			
QN-2	1149.49± 310.1 (Av.20)	58.35± 22.49 (Av.20)	23.14± 4.91 (Av.20)	426.92± 409.43 (Av.53)	29.38± 36.2 (Av.52)	11.83± 4.13 (Av.53)	513.37± 270.26 (Av.45)	15.32± 8.08 (Av.45)	13.97± 5.75 (Av.45)
QN-3				366.58± 283.63 (Av.36)	21.0± 13.2 (Av.36)	14.78± 7.45 (Av.36)	523.98± 291.0 (Av.42)	16.22± 6.65 (Av.42)	11.98± 4.53 (Av.42)
QN-4				554.34± 472.08 (Av.27)	41.43± 28.28 (Av.27)	22.1± 12.19 (Av.27)	476.08± 203.87 (Av.29)	75.85± 34.98 (Av.29)	74.07± 35.12 (Av.29)
	1 V			100 mV			10 mV		
MCS1	461.1±344.41 (Av.54)			16.9±13.48 (Av.54)			3.14±1.28 (Av.54)		
MCS2	500.66±356.89 (Av.52)			19.16±17.67 (Av.52)			3.52±1.89 (Av.52)		
MCS3	387.28±241.61 (Av.46)			15.6±9.3 (Av.46)			3.23±0.93 (Av.46)		

Table 5.4: RMS of the signal of the tested devices from sinusoidal waveform stimulation. Colour cells indicate measurement was taken after: 2-day (green), 4-day (pink), and 12-day (blue) soak tests, or white if no treatment was applied. Every cell provides the RMS of the signal in the form [average±SD (number of electrodes used for the average and SD)]. MCS 1-3 are the MultiChannel Systems MEAs.

	Signal RMS (square) [μV]								
	Run 1			Run 2			Run 3		
Devices	1 V	100 mV	10 mV	1 V	100 mV	10 mV	1 V	100 mV	10 mV
Q9-2OP	517.28± 52.21 (Av. 54)	69.16± 17.64 (Av.54)		225.85± 61.15 (Av.52)	27.02± 16.06 (Av.52)	7.44± 1.96 (Av.52)	326.49± 54.93 (Av.51)	20.46± 6.37 (Av.51)	8.76± 2.54 (Av.51)
Q9-3OP	246.41± 99.01 (Av.45)	42.43± 12.5 (Av.45)	18.62± 3.83 (Av.45)	209.55± 188.8 (Av.49)	27.13± 23.96 (Av.49)	15.16± 17.82 (Av.49)	393.73± 160.05 (Av.50)	55.68± 56.14 (Av.50)	8.18± 2.62 (Av.50)
Q9-4OP	642.54± 60.8 (Av.46)	80.12± 14.98 (Av.46)	18.93± 3.84 (Av.46)	242.25± 85.2 (Av.48)	21.39± 6.52 (Av.48)	9.37± 2.83 (Av.48)			
QN-2	744.73± 142.34 (Av.20)	84.09± 27.38 (Av.20)	27.47± 4.84 (Av.20)	409.37± 194.75 (Av.53)	27.53± 20.51 (Av.53)	11.63± 4.63 (Av.53)	417.26± 134.88 (Av.45)	33.94± 23.4 (Av.45)	15.3± 6.15 (Av.45)
QN-3				393.44± 138.06 (Av.36)	30.32± 22.11 (Av.36)	12.56± 5.49 (Av.36)	352.03± 91.49 (Av.42)	13.8± 4.72 (Av.42)	12.69± 4.88 (Av.42)
QN-4				280.66± 200.24 (Av.27)	60.05± 38.76 (Av.27)	21.39± 10.24 (Av.27)	462.24± 117.59 (Av.29)	81.83± 38.67 (Av.29)	73.67± 34.93 (Av.29)
	1 V			100 mV			10 mV		
MCS1	414.16±197.89 (Av.54)			10.02±9.72 (Av.54)			4.05±1.98 (Av.54)		
MCS2	393.85±199.17 (Av.52)			20.67±21.44 (Av.52)			6.27±4.68 (Av.52)		
MCS3	403.83±154.78 (Av.46)			10.83±6.16 (Av.46)			2.84±0.58 (Av.46)		

Table 5.5: RMS of the signal of the tested devices from square waveform stimulation. Colour cells indicate measurement was taken after: 2-day (green), 4-day (pink), and 12-day (blue) soak tests, or white if no treatment was applied. Every cell provides the RMS of the signal in the form [average±SD (number of electrodes used for the average and SD)]. MCS 1-3 are the MultiChannel Systems MEAs.

	Signal-to-Noise Ratio 1 V [a.u.]					
	Run 1		Run 2		Run 3	
Devices	Sine	Square	Sine	Square	Sine	Square
Q9-2OP	75.11±13.14 (Av.54)	31.04±5.08 (Av.54)	28.58±29.07 (Av.52)	31.49±13.85 (Av.52)	52.17±23.51 (Av.51)	39.2±12.61 (Av.51)
Q9-3OP	9.27±5.02 (Av.45)	7.34±3.83 (Av.45)	61.2±93.64 (Av.49)	32.25±42.15 (Av.49)	65.22±77.36 (Av.50))	48.53±35.85 (Av.50)
Q9-4OP	64.37±14.04 (Av.46)	36.78±6.92 (Av.46)	14.63±5.84 (Av.27)	27.94±12.52 (Av.27)		
QN-2	47.42±16.99 (Av.20)	30.57±9.59 (Av.20)	43.72±49.35 (Av.53)	40.66±27.07 (Av.53)	42.83±25.45 (Av.45)	35.44±14.89 (Av.45)
QN-3			24.59±18.1 (Av.36)	26.82±10.92 (Av.36)	49.31±40.44 (Av.42)	33.08±14.65 (Av.42)
QN-4			23.55±15.56 (Av.27)	12.28±6.33 (Av.27)	8.35±4.64 (Av.29)	7.79±2.73 (Av.29)
	Sine		Square			
MCS1	157.43±144.45 (Av.54)		142.45±89.01 (Av.54)			
MCS2	160.05±125.03 (Av.52)		131.08±85.01 (Av.52)			
MCS3	123.97±93.7 (Av.46)		128.86±66.31 (Av.46)			

Table 5.6: Signal-to-Noise Ratio of tested devices from 1 V stimulation. Colour cells indicate measurement was taken after: 2-day (green), 4-day (pink), and 12-day (blue) soak tests, or white if no treatment was applied. Every cell provides the SNR of the signal in the form [average±SD (number of electrodes used for the average and SD)]. MCS 1-3 are the MultiChannel Systems MEAs.

	Signal-to-Noise Ratio 100 mV [a.u.]					
	Run 1		Run 2		Run 3	
Devices	Sine	Square	Sine	Square	Sine	Square
Q9-2OP	2.44±0.66 (Av.54)	4.15±1.21 (Av.54)	1.88±0.84 (Av.52)	3.85±2.89 (Av.52)	1.8±0.72 (Av.51)	2.37±0.81 (Av.51)
Q9-3OP	0.96±0.32 (Av.45)	1.19±0.3 (Av.45)	4.12±7.11 (Av.49)	3.91±5.53 (Av.49)	3.18±5.2 (Av.50)	7.64±11.78 (Av.50)
Q9-4OP	2.36±0.52 (Av.46)	4.54±0.92 (Av.46)	1.31±0.18 (Av.27)	2.43±0.94 (Av.27)		
QN-2	2.4±1.1 (Av.20)	3.45±1.38 (Av.20)	3.05±5.23 (Av.53)	2.68±2.71 (Av.53)	1.23±0.61 (Av.45)	2.81±2.07 (Av.45)
QN-3			1.29±0.41 (Av.36)	1.9±1.11 (Av.36)	1.48±0.88 (Av.42)	1.26±0.57 (Av.42)
QN-4			1.77±0.82 (Av.27)	2.69±1.46 (Av.27)	1.11±0.07 (Av.29)	1.2±0.14 (Av.29)
	Sine		Square			
MCS1	5.83±5.62 (Av.54)		3.54±3.9 (Av.54)			
MCS2	6.07±5.75 (Av.52)		6.6±7.29 (Av.52)			
MCS3	5.03±3.7 (Av.46)		3.54±2.52 (Av.46)			

Table 5.7: Signal-to-Noise Ratio of tested devices from 100 mV stimulation. Colour cells indicate measurement was taken after: 2-day (green), 4-day (pink), and 12-day (blue) soak tests, or white if no treatment was applied. Every cell provides the SNR of the signal in the form [average±SD (number of electrodes used for the average and SD)]. MCS 1-3 are the MultiChannel Systems MEAs.

	Signal-to-Noise Ratio 10 mV [a.u.]					
	Run 1		Run 2		Run 3	
Devices	Sine	Square	Sine	Square	Sine	Square
Q9-2OP	1.12±0.3 (Av.54)		1.06±0.09 (Av.52)	0.96±0.06 (Av.52)	0.88±0.09 (Av.51)	0.99±0.22 (Av.51)
Q9-3OP	0.53±0.14 (Av.45)	0.54±0.15 (Av.45)	1.22±0.58 (Av.49)	2.37±4.0 (Av.49)	1.02±0.42 (Av.50)	0.93±0.34 (Av.50)
Q9-4OP	1.09±0.2 (Av.46)	1.04±0.21 (Av.46)	1.16±0.13 (Av.27)	1.02±0.08 (Av.27)		
QN-2	0.91±0.16 (Av.20)	1.1±0.23 (Av.20)	1.07±0.36 (Av.53)	1.04±0.41 (Av.53)	1.11±0.26 (Av.45)	1.25±0.43 (Av.45)
QN-3			0.91±0.06 (Av.36)	0.8±0.09 (Av.36)	1.03±0.14 (Av.42)	1.09±0.18 (Av.42)
QN-4			0.96±0.23 (Av.27)	0.95±0.21 (Av.27)	1.08±0.09 (Av.29)	1.07±0.06 (Av.29)
	Sine		Square			
MCS1	1.02±0.33 (Av.54)		1.33±0.69 (Av.54)			
MCS2	1.02±0.27 (Av.52)		1.77±1.01 (Av.52)			
MCS3	0.97±0.28 (Av.46)		0.89±0.26 (Av.46)			

Table 5.8: Signal-to-Noise Ratio of tested devices from 10 mV stimulation. Colour cells indicate measurement was taken after 2-day (green), 4-day (pink), and 12-day (blue) soak tests, or white if no treatment was applied. Every cell provides the SNR of the signal in the form [average±SD (number of electrodes used for the average and SD)]. MCS 1-3 are the MultiChannel Systems MEAs.

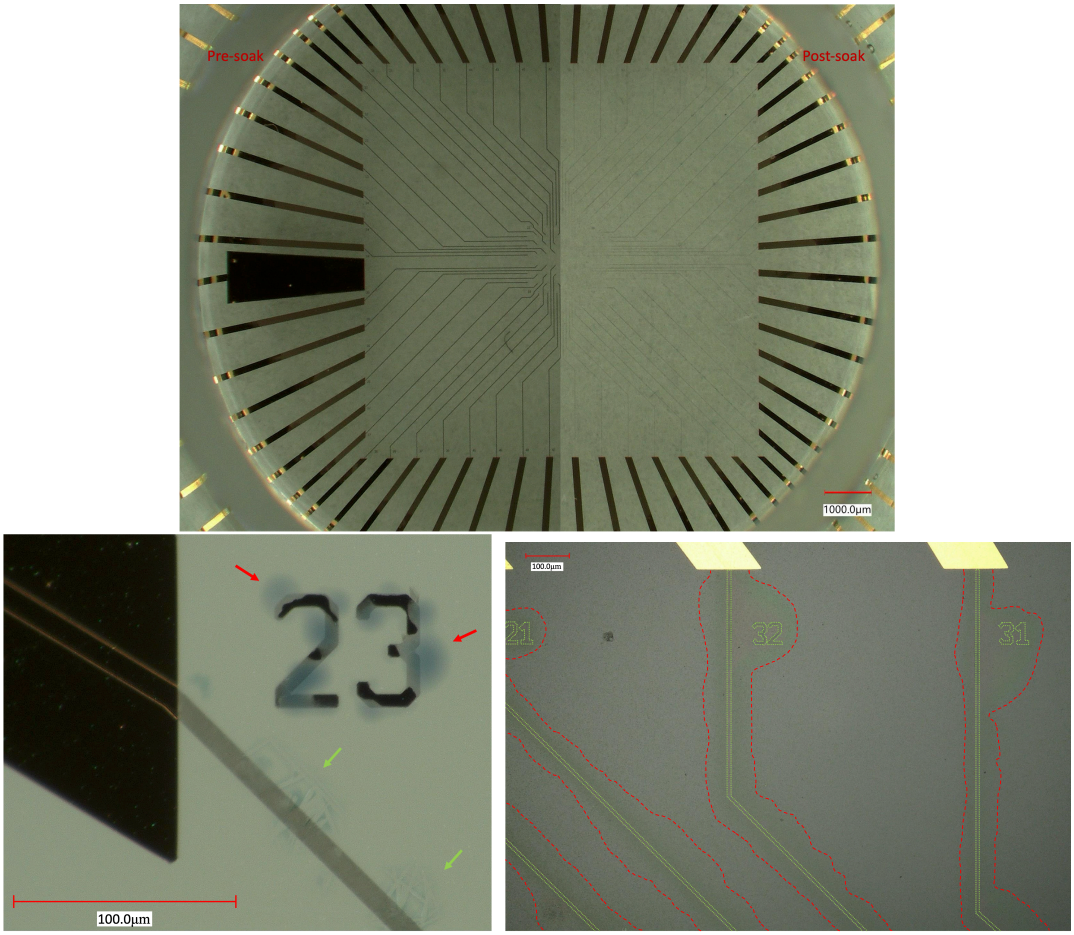

Figure 5.5: Effects of soak test on the devices. **Upper**: Image depicting the MEA circuit. The left-hand side of the image was taken prior to the soak test, while the right-hand side was taken after it. **Lower left**: Image of a MEA track after soak test. Pointed at with red arrows are areas with a blue colouration next to Mo structures. Green arrows point to visible crystals in the areas with blue colouration. **Lower right**: Darker regions near the Mo tracks after the soak test. Outlined in red lines are the darker areas around the Mo tracks. Outlined in green are the original Mo structures for better visualisation.

geneities in CVD-grown graphene, incomplete removal of the metal layer from electrode pads, and structural damage. This accumulation of defects can strongly influence the difference observed among batches. For instance, batch QN exhibited more noise and instability compared to batch Q9.

All gMEAs that underwent any form of soaking test remained capable of recording signals, although with notable variations in baseline noise and sensitivity. The baseline noise decreased by $\sim$ 56%, reaching an average of $\sim$ 10 μV, while recorded signal amplitudes decreased by $\sim$ 50% on average, indicating an altered device sensitivity. Furthermore, an increase in the SD of the signal RMS and corresponding SNR, with respect to the initial SDs, indicates greater differences among electrodes.

Numerous variables can contribute to the observed changes, but the primary factors are the permeability of the encapsulation layer and the degradation of Mo. The encapsulation layer's permeability enables water and solutes to penetrate the tracks during the soaking tests, altering the gMEA's behaviour. Simultaneously, Mo degradation alters the circuit's material composition and introduces new compounds, such as molybdate ions, that can alter the electrical properties of the track. This degradation is facilitated by the presence of water and solutes in the tracks. These factors play a large role in modifying the electrochemical properties of the circuit and subsequently affect the baseline noise and sensitivity of the device. In a similar manner, the increased disparity among electrode recordings (SD) post-soaking can be attributed to the non-uniform degradation of Mo across tracks.

Changes in run 3 can also be explained by means of the same phenomena. For instance, devices Q9-2OP and Q9-3OP were allowed to dry for around 2 weeks after their soak tests, allowing for all the water to evaporate from the tracks and leave behind solutes or Mo degradation compounds. This

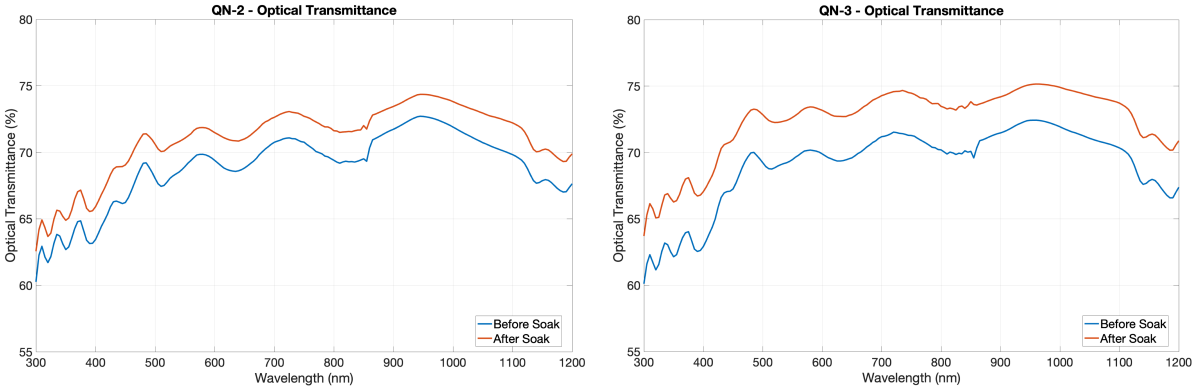

Figure 5.6: Optical transmittance measurements of functional devices before and after soak test. **Left**: Measurements of device QN-2. **Right**: Measurements of device QN-3.

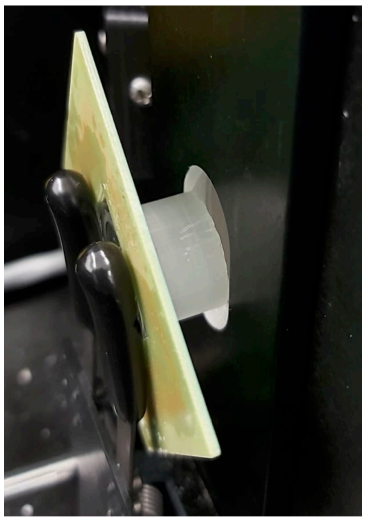

Figure 5.7: Setup of a device for an OT measurement. The sample stands 12 mm away from the opening.

removal of water and precipitation of solutes are factors that can change the electrochemical behaviour of the device. Device QN-2 was soaked for an additional 12 days following the 2-day soak test it had just undergone. Optical microscopy examinations determined that Mo degradation was still ongoing at the end of the 12-day soak test, elucidating that the signal changes observed were caused by the continued degradation of Mo structures. Lastly, device QN-4 exhibited a dramatic increase in baseline noise and a substantial increase in signal, without undergoing a soaking test. This was likely due to the briefly exposure to PBS (rinsed with DI water) while performing the measurements. The water remains may have caused the formation and accumulation of Mo compounds near the electrode while air drying, which led to the increased baseline noise. This latter finding can be extended to explain the decrease in baseline noise observed in other devices after the first soak test. In new devices, the remains of Mo compounds from the etching step may cause an increased baseline noise. However, prolonged exposure to the differentiation medium dilutes and diffuses these compounds, reducing their impact. In contrast, for device QN-4, the produced Mo compounds, unable to diffuse out into a liquid medium, accumulate, contributing to increased baseline noise. Nevertheless, these are merely educated guesses of the processes taking place, and a larger sample size is needed to reach accurate conclusions.

In summary, significant variations in signal RMS and SNR values were observed from the device's initial characterization, attributed to fabrication inhomogeneities and batch differences. The soaking test highlighted the gMEA's vulnerability to the culture medium, driven by encapsulation layer permeability and Mo biodegradability. This is evident in optical microscope images, where Mo fades from tracks and sealed structures, increasing the OT of the device in the process. These alterations in conductive elements and the surrounding environment led to signal instability, manifesting as notable variations in

baseline noise and signal sensitivity after exposure to the culture medium. The key numerical findings regarding average baseline noise and signal RMS are presented in table 5.9. Nonetheless, the significant distance between stimulating and recording electrodes in the signal recording setup complicates drawing conclusions on the relationship between stimulation amplitude and recorded signals. This is due to signal dissipation in PBS, which makes the voltage reaching the electrodes unknown.

		Baseline Noise (μV)	Sinusoidal Amplitude (μV)	Square Amplitude (μV)
Pre-soak	1 V	23	795	471
	100 mV		39	61
	10 mV		20	20
Post-soak	1 V	10	362	309
	100 mV		19	25
	10 mV		11	12

Table 5.9: Summary of average baseline noise and signal RMS of all devices before and after being soaked.

5.2.2. Photoinduced Artifact Test

The photo-induced artifact test was performed to assess the devices' sensitivity to photostimulation of different intensities. Two types of stimulation were performed, stimulating the entire MEA and only the electrodes (as described in Section 4.2.3), to assess the influence of the gold tracks on the presence of artifacts. Out of all the assessed devices, artefacts were visible to the naked eye in the recorded data of three devices, in the form of spikes. One device displayed artifacts upon stimulation of the entire MEA, another only when stimulation was targeted exclusively at the electrodes, and the third showed no artifacts during whole MEA stimulation but did when only the electrodes were stimulated.

To perform a more detailed analysis of the recorded signals, these were plotted as normalised power spectra. The presence of peaks at the fundamental and harmonic frequencies of the stimulation would indicate the sensitivity of the devices to photostimulation. Since the stimulation was performed mimicking that used for optogenetic cell stimulation, at 1 Hz, the signs of photoinduced artifacts would be displayed as an intense peak at 1 Hz, and harmonics with decreasing intensities at every integer frequency. An example of this can be seen in Fig. 5.8 (R), which displays the normalised power spectrum of an electrode from a device with visible artifacts in the time domain. In the figure, an increasing peak intensity with increasing photostimulation intensity is also visible, further linking the photostimulation to the presence of these artifacts. Nonetheless, peaks at $\sim$1 Hz are also visible on devices without artifacts in the time domain, but with nearly no harmonics present [Fig. 5.8 (L)]. Furthermore, the increasing peak intensity with increasing light intensity relationship is also observed in this case. Though this would point to some degree of sensitivity of all devices to photostimulation (independently of stimulation approach (whole MEA or only electrodes)), the low-frequency region of the power spectrum is highly influenced by other sources of noise, as can be seen in the baseline power spectrum plots of the devices [Fig. 5.8 (L and R)]. This activity may alter the observed peaks, leading to inconclusive results.

While the photosensitivity of the devices cannot be completely discarded, the presence of molybdenum trioxide (MoO_3), one of the principal bi-products of Mo degradation, may also influence these outcomes. This compound is sensitive to photostimulation, as changes to its colouration, as well as photoelectric properties, are observed [142–144, 146, 147]. Thus, its presence in the MEAs may contribute to the appearance of photoinduced artifacts.

Additionally, a high-intensity peak at 50 Hz was identified in the power spectrum of the devices [Fig. 5.9]. This can be attributed to the power line noise which alternates at 50 Hz in Europe.

5.2.3. Benchmark

The commercial MCS 60MEA200/30iR-Ti MEAs were assessed and compared to our devices based on their SNR and photosensitivity, using the gMEAs' initial characterisation values. The highest SNRs were achieved during the 1 V stimulation, largely outperforming the gMEA devices. On average, the MCS-MEAs were 3.61 and 5.56 times larger than the corresponding gMEA average for sinusoidal and square waveforms, respectively [Tbl. 5.6]. As expected, the MCS-MEAs also exhibit an exponential

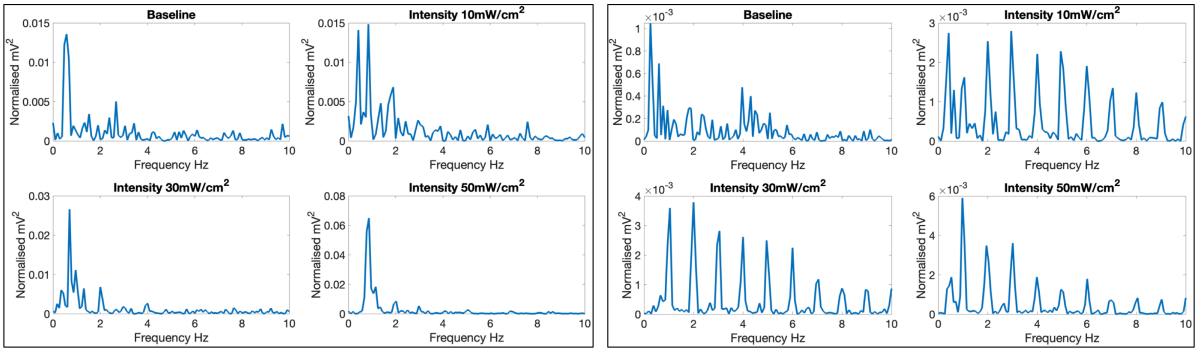

Figure 5.8: Normalised power spectrum of signals recorded during photoinduced artifact test. **Left**: Plot of device showing no artifacts in the time domain. **Right**: Plot of device presenting artifacts in the time domain.

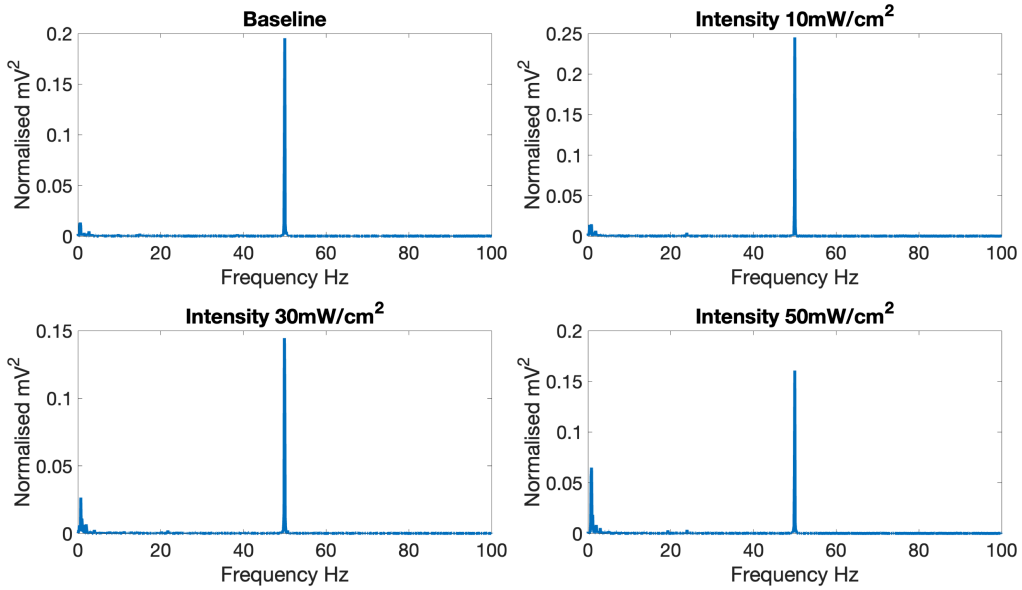

Figure 5.9: Normalised power spectrum of signals recorded during photoinduced artifact test displaying power line noise. This plot is the same as Fig. 5.8 (L), but with x-axis extended to 100 Hz.

decrease in SNR with decreasing stimulation amplitude but remain larger than that of the gMEAs for 100 mV stimulation. In this case, the average MCS-MEA SNR were 3.02 and 1.53 times larger than that of their respective sinusoidal and square counterparts from the gMEA devices [Tbl. 5.7]. At last, the SNRs from the 10 mV stimulation turned out to be very similar to those of the gMEA array, very near a ratio of 1, and thus insufficient for adequate signal detection [Tbl. 5.8]. However, by looking at the noise and signal RMS independently, we find that the baseline noise is the main reason why the SNR is substantially lower in our devices. For the MCS devices, the average baseline noise is 4 μV, compared to 23 μV observed in gMEAs [Tbl. 5.3]. On the other hand, gMEAs attain a higher signal RMS at 1 V ($\sim$ 1.6 times larger) and 100 mV ($\sim$ 3.7 times larger) for both sinusoidal and square waveform stimulations compared to MCS-MEAs [Tbl. 5.4 and 5.5]. This however changes after the soaking tests, when the gMEAs' signals reach similar RMS values to the commercial devices', except for the 100 mV stimulation with square waveform, where gMEAs signals remain larger.

Lastly, the MCS-MEAs underwent the photoinduced artifact test. Only one of the devices displayed a visible artifact in the time domain signal, in the form of a small depression in the baseline signal. Subsequently, the signals were assessed in the form of a normalised power spectrum. Most of the assessed electrodes presented a nearly noiseless baseline signal throughout all frequencies, excluding an initial peak near 0 Hz [Fig. 5.10 (UL)]. Nonetheless, photoinduced artifacts were visible to some degree in all of them, without the influence of other sources of noise. The intensity of the artifacts varied from negligible, typically only minimally visible in the 30 and 50 mW/cm^2 stimulated signals, to prominent,

clearly visible at even the 10 mW/cm^2 stimulated signal [Fig. 5.10]. In all cases, the peaks were well aligned with the 1 Hz and subsequent harmonic frequencies. This and the increasing artifacts' intensities with increasing stimulation intensity demonstrate some degree of photosensitivity. Additionally, the influence of the power line noise (50 Hz peak) was negligible throughout the assessment.

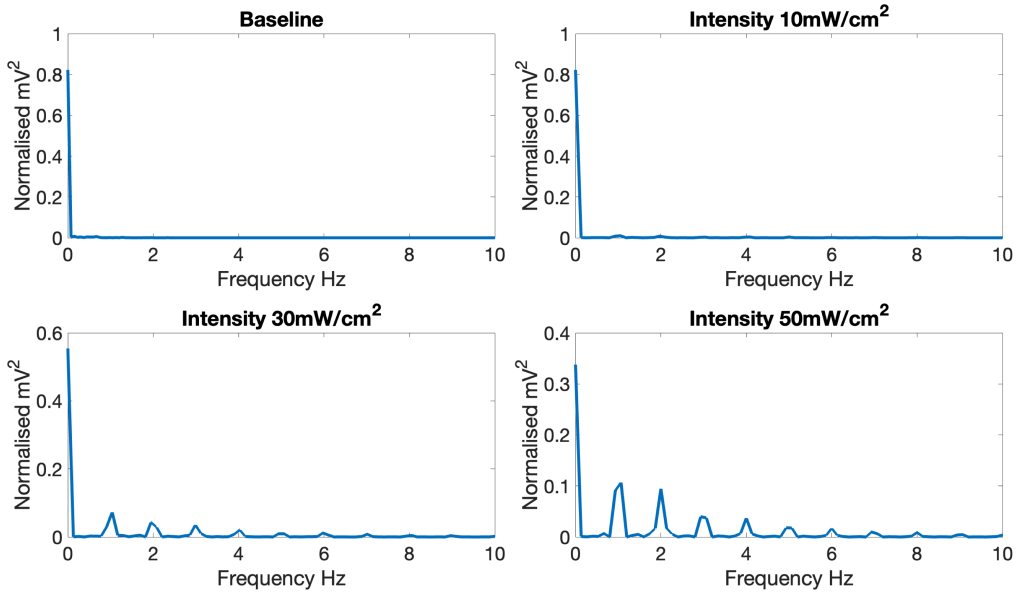

Figure 5.10: Normalised power spectrum of signals recorded using the MCS-MEAs during photoinduced artifact test. Photoinduced artifacts are visible at all light intensities but primarily at 30 and 50 mW/cm^2.

In summary, the MCS-MEAs demonstrate a superior performance over gMEAs, primarily due to their significantly lower baseline noise. However, gMEAs showcase a higher signal amplitude in recorded signals. Furthermore, MCS-MEAs exhibit no sensitivity to power line noise, whereas gMEAs are notably influenced by it. It is essential to acknowledge that the evaluation of the gMEAs has been significantly impacted by various device-related issues. To provide a more accurate and representative comparison, a reassessment should be conducted after resolving these underlying issues.

5.2.4. Ageing Test

The evolution of the devices through the ageing test was monitored through optical microscopy. The exact degradation and timeline of the processes varied per device, however, a general pattern was observed. Generally, the Mo degradation began immediately, mostly around the region of the electrode openings and showed no effect on the Mo regions with no openings [Fig. 5.11 (Day 1)]. Furthermore, the formation of large ($> 450\mu m$) and small white salt deposits ($< 5\mu m$) were visible from day 1 [Fig. 5.13 (Day 1)]. Subsequently, we observed the formation of large "bubbles" along some tracks on days 1 and 2 [Fig. 5.12 (Day 1)]. The bubble formation can be attributed to the rapid expansion of Mo oxide layers and subsequent dissolution and release of molybdate ions [142]. Furthermore, a steep increase in concentration gradient on the area of degradation may contribute to the swelling via diffusion of water through the parylene C layer, as its permeability has already been confirmed [148].

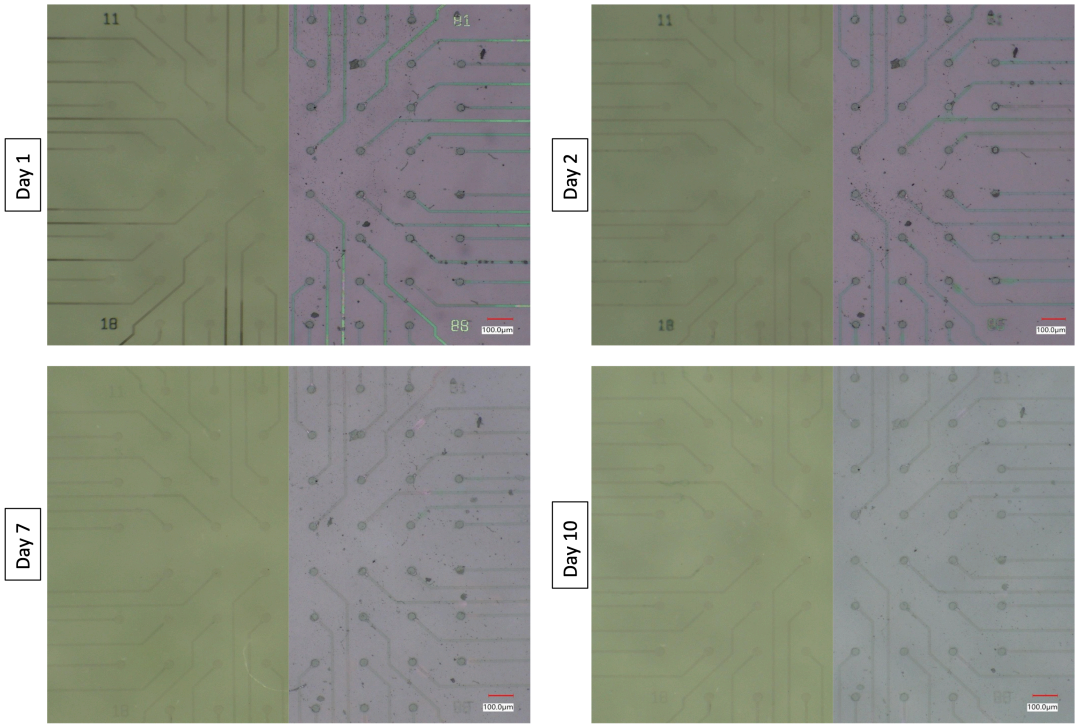

Figure 5.11: Mo degradation of MEA electrodes in ageing test. Left and right-hand side of the figures taken with coaxial and ring lighting of the microscope. **Day 1**: Start of the degradation near the electrode openings. Degrading tracks present a green colouration. **Day 2**: Degradation has extended to unopened regions of the MEA (numbers). Degradation extends to all tracks beyond the centre. Degrading Mo structures display pink/green colouration, which extends to surrounding areas in some cases. **Day 7**: Mo degradation is nearly complete and tracks are mostly transparent with some minor colouration. **Day 10**: Mo structures are completely transparent and display minimal remains of Mo compounds.

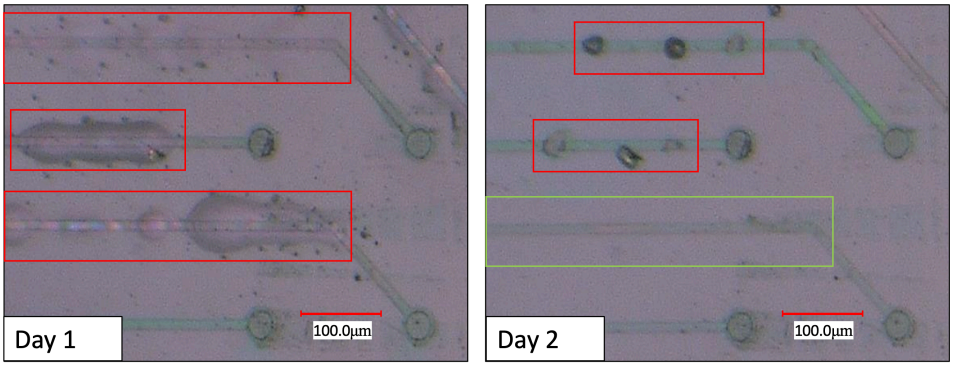

Figure 5.12: Bubble formation along tracks in ageing test. **Day 1**: Red squares outline the presence of bubbles on the tracks. **Day 2**: Red squares point to the salt deposits that remain after the bubble. The green square points to a track where salt deposits did not form.

By day 2, the degradation of Mo had reached the entirety of every track as well as the sealed structures (such as the indicator numbers). This is an indicator that the PBS had penetrated the encapsulation layer. Nonetheless, the central area remained the most degraded region [Fig. 5.11 (Day 2)]. At this point, tracks appear pink and green, in some cases extending to the surrounding areas of the tracks. The colouration is once again caused by Mo compounds formed during its degradation. The identification of the exact compounds is outside of the scope of this project, however, Mo trioxide along with molybdate ions formed through hydrolysis or redox reactions in combination with the PBS salts are the most likely candidates, as they are able to display a wide range of colours [142–144]. In the case of device QN-1, the colouration accumulated around the tracks, restricted to the surrounding area similar to figure 5.5 (LR). In comparison, the other devices seemed to dissipate the colour better.

The previously mentioned bubbles have now deflated, in most cases leaving behind areas with salt deposits [Fig. 5.12 (Day 2)].

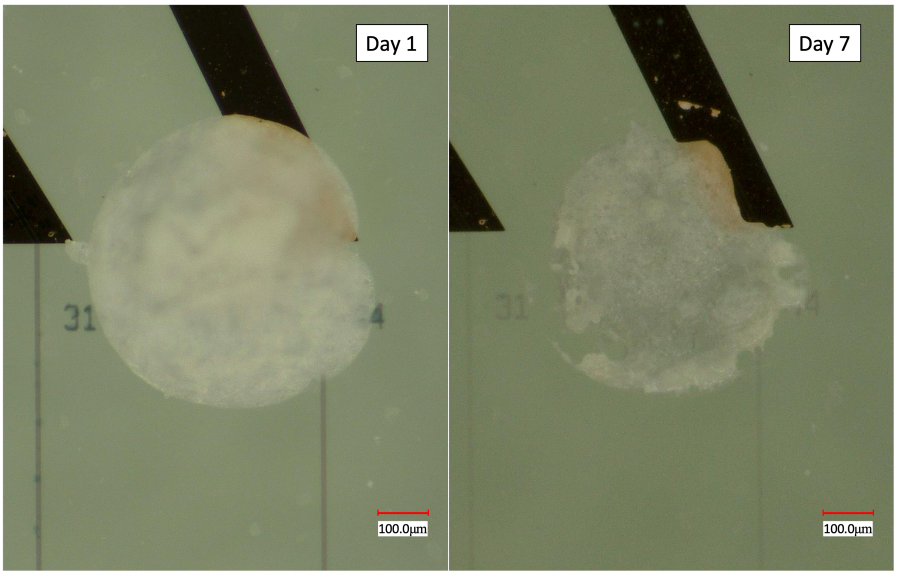

Figure 5.13: Degradation of salt deposits in ageing test. **Day 1**: Salt deposit with diameter $\sim$ 500 μm. **Day 7**: Observable degradation of salt deposit.

By day 4, we observed darker markings around the epoxy used to attach the well. This is likely caused by salt deposits beneath the parylene C under the epoxy [Fig. 5.15 (Day 4)]. The tracks continue to degrade but have lost a large portion of their green/pink colouration. Furthermore, small salt deposits are appearing along some graphene and Au tracks. Some delamination between the parylene C and the Au track is observed near the graphene / Au interface on days 4 and 7. These delaminations appear in the form of a large bubble covering the region of the Au track [Fig. 5.14 (Day 4)] This can be explained in a similar manner to the formation of bubbles along Mo tracks. In this case, however, the low adhesion of parylene C to metals may be the reason why the bubble forms on the Au surface rather than on areas with better adhesion to parylene C [148]. Furthermore, the delay in the appearance of signs of Mo degradation compared to other structures could be attributed to the protection offered by the Au track, covering a section of the graphene track.

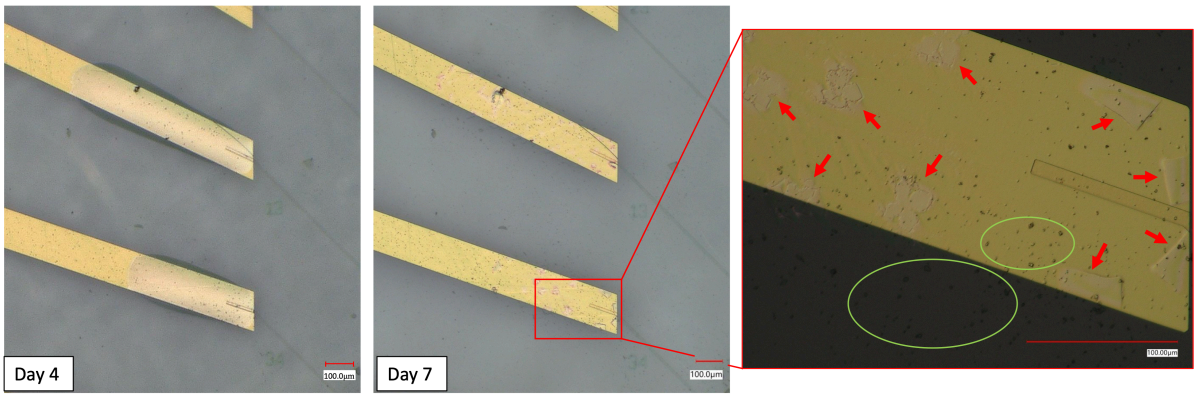

Figure 5.14: Paryelene C delamination from Au during ageing test. **Day 4**: Presence of bubbles on multiple Au tracks at the interface with the graphene tracks. **Day 7**: Bubbles deflate leaving behind green/pink crystals. **Zoomed in image**: Red arrows point to pink crystals on the Au surface. Green circles outline small salt deposits visible as small dark spots.

By day 7, the tracks are nearly transparent with some minor colouration still visible on the tracks and next to them. The closed Mo structures are also nearly completely degraded [Fig. 5.11 (Day 7)]. The larger salt deposits that formed by day 1 are being degraded by this point [Fig. 5.13 (Day 7)], but smaller deposits ($< 5\mu m$) are still visible throughout the device [Fig. 5.14 (day 7 - green circles)]. By

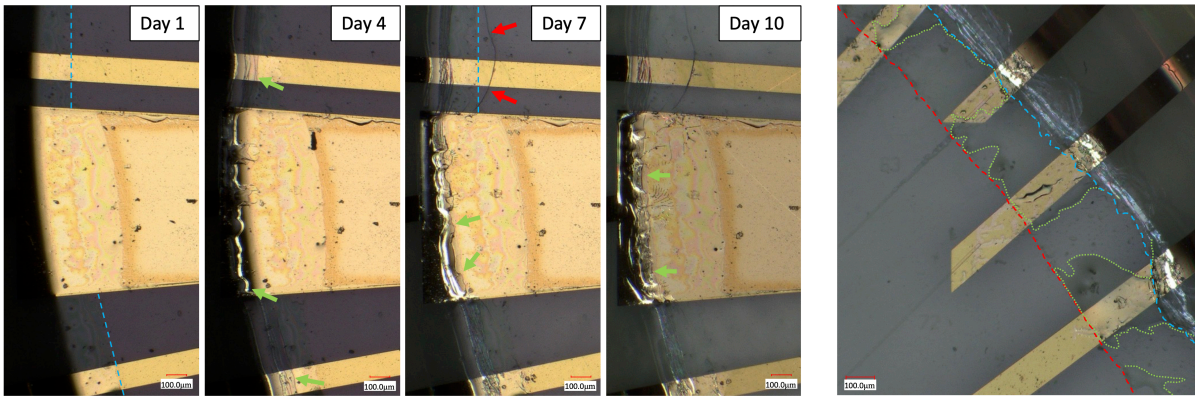

Figure 5.15: Epoxy delamination during ageing test. **Day 1**: Blue dotted lines indicate the limit of the epoxy adhesive. **Day 4**: Green arrows point to the markings within the epoxy region, likely caused by salt deposits beneath the parlyene C under the epoxy layer. The more shiny areas are possibly fluid accumulations. **Day 7**: Red arrows point to the boundary of a delamination that has moved past the epoxy limit (blue line). Green arrows point to the expanded boundary of the fluid accumulation which expands beneath the epoxy. **Day 10**: Green arrows point to the "deflated" fluid accumulation beneath the epoxy layer. **Right**: Microscope image of the upper right corner, of the same device from left images, on day 10. The blue dotted line indicates the limit of the epoxy adhesive, the red dotted line highlights the boundary of delamination that had moved past the epoxy limit (blue dotted line) creating a large fluid accumulation, and the green dotted lines point to fluid deposits remaining after the retraction of fluid from the red dotted line.

day 8, new delaminations of parylene from the Au tracks are visible, and the ones that formed earlier are now deflating and forming green/pink crystals in the area [Fig. 5.14 (Day 7 - red arrows)]. Furthermore, delamination in the form of bubbles is also visible around the edges of the epoxy and extends inwards [Fig. 5.15 (Day 7 - red arrows, and right image - red line)] (no signs of epoxy delamination for device QN-1).

Lastly, on day 10, we observe that all the regions near Au which delaminated show the presence of green/pink crystals. The delaminations near the epoxy have now diminished, but some larger and smaller bubbles are still present [Fig. 5.14 (Right image - green outline)]. The tracks are now completely transparent or with very few remains of Mo degradation [Fig. 5.11 (Day 10)]. Small salt deposits ($< 5\mu m$) are visible throughout the MEA [Fig. 5.14 (green circles)].

OT measurements of the devices showed an increase in transmittance over time, starting from day 2 and peaking on day 10 [Fig. 5.16]. This trend, similar to that observed during the soaking test [Sec. 5.2.1], is attributed to the degradation of the opaque Mo layer due to the encapsulation layer's permeability to PBS. Once more, the sinusoidal shape of the spectra can be attributed to interference caused by the optical properties of parylene C [145].

The devices were also characterised by EIS throughout the ageing test. An attempt to improve EIS measurements by rinsing the electrodes with IPA prior to testing was carried out. The aim was to remove possible residues on the electrode surface. Variations in the outcomes were however insignificant, thus EIS measurements were performed directly on the electrodes with fresh PBS.

In the initial evaluation, we observed a high impedance across all devices, decreasing with increasing frequency linearly [Fig. 5.17 (L)]. The phase plot exhibited significant capacitive dominance through all frequencies, remaining $\sim$ -70º up to 10^3 Hz, and then progressing towards -130º by 10^5 Hz [Fig. 5.17 (R)]. The increase in phase beyond -90º is associated with complex electrochemical processes. In our case, it is most likely caused by the large resistance of the circuit caused by the use of graphene. This can limit the current flow, especially at lower frequencies, leading to a phase lag and explaining the more negative phase observed. Alternatively, a phase angle reaching -130, particularly at high frequencies might also suggest the influence of inductive components in the circuit. This is less likely considering our device but could be caused by the leads connecting the gMEA to the potentiometer. The Nyquist plot presents a nearly straight line at $\sim$ 40º from the x-axis, which is associated with the Warburg impedance [Fig. 5.18]. This suggests reactions at the electrode-electrolyte interface are mostly dominated by diffusive processes.

During the ageing test, EIS measurements revealed behavioural variations in the devices. The most significant changes occurred within the first few days, stabilising the latest by day 4. We observed a dramatic reduction in impedance across all frequencies during this period [Fig. 5.17 (L)], showing a

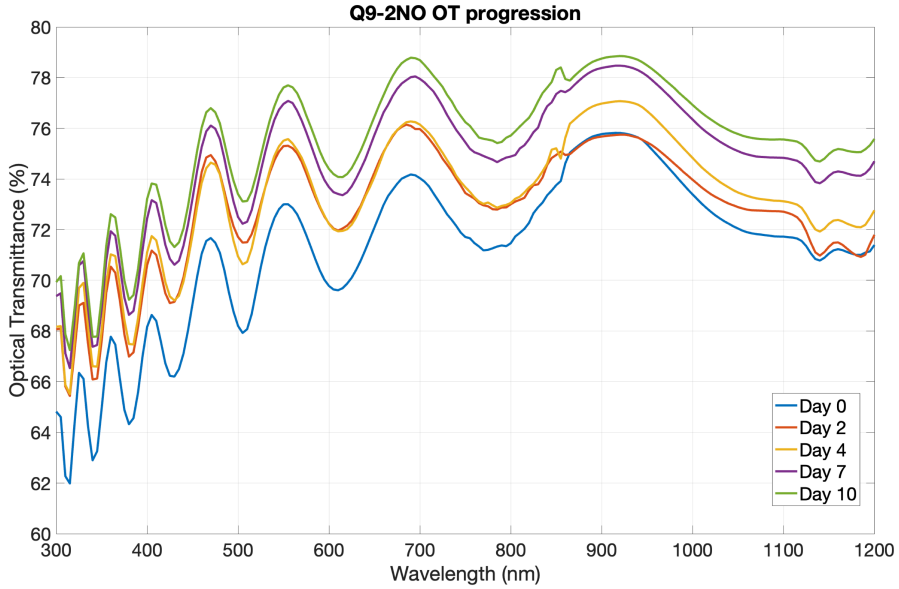

Figure 5.16: Progression of OT from device Q9-2NO during ageing test.

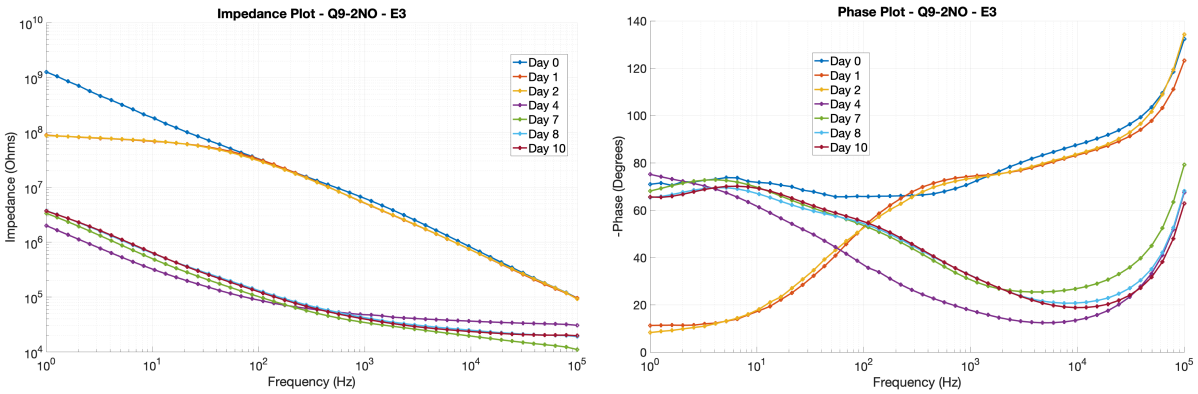

Figure 5.17: EIS impedance and phase measurements of device Q9-2NO, electrode 3, throughout the ageing test. **Left**: Impedance measurements. **Right**: Phase measurements

drop of 98.5-99.1% between the initial and final measurements at 1kHz [Tbl. 5.10]. There was also a noticeable shift in phase, where capacitive behaviour dominated smaller frequencies, shifting towards a resistive behaviour in higher frequencies, and switching again to capacitive behaviour by $\sim 10^5$ Hz [Fig. 5.17 (R)]. These changes are caused by the penetration of PBS through the encapsulation layer, resulting in short-circuits that lower the overall resistance of the device and lead to a decreased impedance. Similarly, the introduction of conductive paths due to PBS infiltration can result in a more resistive behaviour, causing a reduction in the phase angles as the capacitive elements are bypassed. However, at very high frequencies ($\sim 10^5$ Hz), the capacitive elements become dominant again. Furthermore, we can expect the space left behind after Mo degradation will be filled in by PBS. While this does not mean that all the tracks exposed to PBS will behave as the electrode surface, it is possible that a larger area than the electrode pad will act as the primary site for electrochemical reactions, thus lowering the impedance.

The Nyquist plot underwent a significant decrease in magnitude due to the proportional decrease in impedance. The new plot displays a half semicircle associated with charge transfer processes, followed by a much longer straight line at $\sim$ 40-45º from the x-axis (Warburg impedance), indicating the dominance of diffusive processes [Fig. 5.18]. The appearance of the half semicircle may have been caused by the Mo removal, which could have masked the charge transfer resistances due to its conductive nature. In fact, we also see a semicircle in the Nyquist plot of days 1 and 2 (before the short-circuits), when the changes were caused by the Mo degradation [Fig. 5.18].

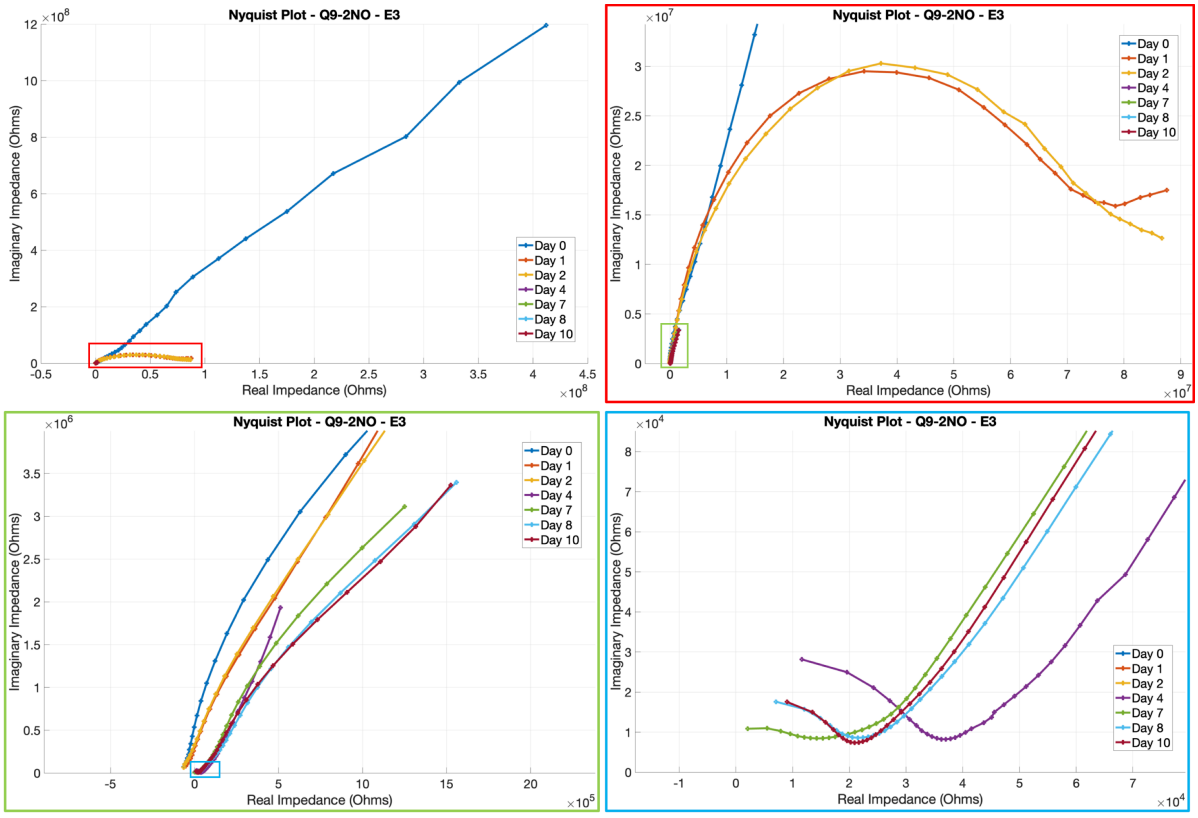

Figure 5.18: Nyquist plots from electrode 3 in device Q9-2NO through the ageing test. Due to the difference in magnitude, multiple zoomed-in versions of the plot are shown.

One of the three assessed devices (QN-1) produced different Bode and Nyquist plots (not included) than the ones previously described. The drop in impedance was not as large as for the other two devices [Tbl. 5.10], and the phase plot remained similar to the initially described one, where a capacitive behaviour is depicted throughout all frequencies, reaching -120º by $\sim 10^5$ Hz. Additionally, the device only became more stable on day 7. This difference is attributed to a better adhesion of the encapsulation layer. For the insulation of this device, the deposition tool had just been cleaned, and it facilitated reaching a high vacuum. This improved adhesion restricts the volume of PBS crossing the encapsulation layer, thereby lessening the extent of electrolyte-induced short-circuiting pathways between the tracks. Consequently, the overall impact on the device impedance and phase characteristics is reduced. Nonetheless, full Mo degradation still takes place in this device. Furthermore, its Nyquist plots remained as straight lines throughout the tests, only decreasing in magnitude and with smaller angles to the x-axis (∼10-20º). The reduced angles indicate a mixed control with charge transfer and diffusive processes.

The devices experienced damage during the ageing test, making the impedance values obtained from the initial characterisation the most reliable indicators of their performance. These values are higher than those typically reported in the literature, especially for device QN-1. However, when area normalised, the impedance is comparable to figures from other studies, even if on the higher end [Tbl. 2.1]. This discrepancy could be attributed to a greater number of defects in our graphene compared to those in other research [43, 67, 133].

An attempt to characterise the electrodes through CV was also carried out. However, the device did not withstand the test, leading to the dissolution of multiple Au tracks [Fig. 5.19]. Before the complete failure, three CV measurements were carried out, each with worsened outcomes. Considering this was the first characterisation of the devices, we theorise that a charge buildup along the track may have caused some sort of electroosmotic flow. Thus, PBS would be forced through the parylene C, which would have taken several days to penetrate otherwise. Considering the highly capacitive behaviour observed in the phase plot of the EIS measurement, a charge build-up is plausible [Fig. 5.17 (R)].

Table 5.10: Evolution of average impedance at 1kHz and area normalised impedance during ageing test. Number of electrodes used to calculate the average and surface area of electrodes is noted next to the device name. The differences in surface area are due to the electrode openings on some devices [Sec. 3.1].

		Day						
Device		0	1	2	4	7	8	10
Q9-2NO (av. 16) Area: $\sim 707\ \mu m^2$	Impedance ($10^4\Omega$)	522.94 ± 311.2	560.14 ± 220.41	519.99 ± 178.21	4.23 ± 1.51	4.05 ± 1.92	4.10 ± 1.73	4.67 ± 1.31
	Area Normalised Impedance ($\Omega\, cm^2$)	36.96 ± 22.0	39.59 ± 15.58	36.76 ± 12.6	0.3 ± 0.11	0.29 ± 0.14	0.29 ± 0.12	0.33 ± 0.09
Q9-4OP (av. 15) Area: $\sim 659\ \mu m^2$	Impedance ($10^4\Omega$)	320.34 ± 163.32	12.6 ± 9.36	6.68 ± 4.69	5.65 ± 3.61	7.17 ± 2.88	5.43 ± 1.73	4.85 ± 2.49
	Area Normalised Impedance ($\Omega\, cm^2$)	21.11 ± 10.76	0.83 ± 0.62	0.44 ± 0.31	0.37 ± 0.24	0.47 ± 0.19	0.36 ± 0.11	0.32 ± 0.16
QN-1 (av. 11) Area: $\sim 707\ \mu m^2$	Impedance ($10^4\Omega$)	989.0 ± 894.8	435.0 ± 232.3	656.0 ± 332.35	547.68 ± 291.26	380.2 ± 279.54	369.98 ± 234.67	323.97 ± 218.77
	Area Normalised Impedance ($\Omega\, cm^2$)	69.91 ± 63.25	30.75 ± 16.42	46.37 ± 23.49	38.71 ± 20.59	26.87 ± 19.76	26.15 ± 16.59	22.9 ± 15.46

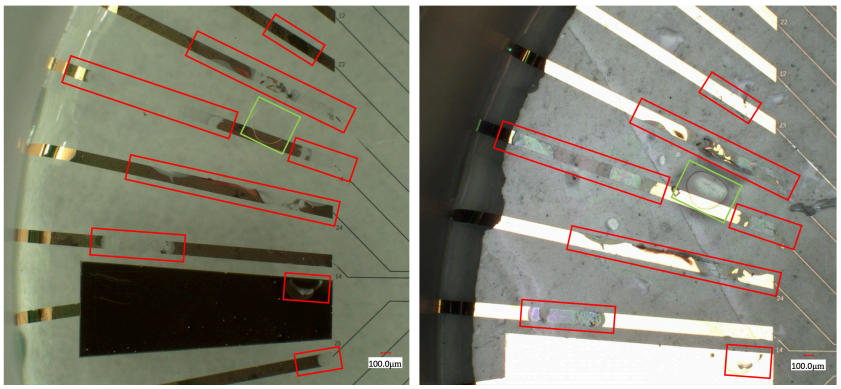

Figure 5.19: Degradation of Au tracks after CV measurement. Left and right sides of the images were taken with coaxial and ring lighting of the microscope, respectively. Outlined in red are the damaged areas, and in green a bubble beneath the parylene C layer.

The presence of PBS on the tracks, combined with the applied voltage, can lead to electrochemical reactions such as the oxidation of gold, forming soluble (Au^{3+}) ions. Additionally, the presence of chloride ions, present in the PBS, can lead to the formation of water-soluble gold-chloride complexes, further enhancing the track dissolution [149, 150]. We also observe damages to more than three Au and graphene tracks [Fig. 5.20], meaning the effect was not limited to the track being tested. This likely occurred after the breakage of the track. The substantial increase of resistance, possibly caused the voltage to flow through alternative nearby tracks. Furthermore, short-circuits due to the presence of PBS may arise among the Au tracks, enabling the completion of the circuit through alternative pathways with lower resistance than the degraded track, thus degrading the surrounding Au tracks.

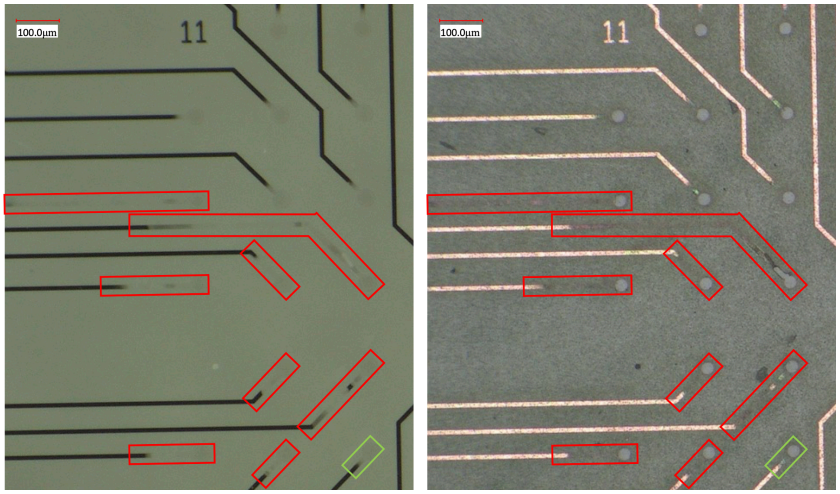

Figure 5.20: Degradation of Mo tracks after CV measurement. Left and right sides of the images were taken with coaxial and ring lighting of the microscope, respectively. Outlined in red are the degraded areas, and in green a normal electrode and track.

Based on these results and observations, the infiltration of fluid and degradation of the Mo layer are the primary contributors to the changes observed during the ageing test.

5.2.5. Biocompatibility Test

Six devices were initially prepared for the experiment, by sterilising them with ethanol and subjecting them to a 2-day soak test to confirm their sterility. None of the devices presented signs of contamination by the end of the 2-day soak test. Due to a limited number of available cells, only 4 of the 6 devices were seeded [Fig. 5.21] and started the cell culture procedure. However, all samples showed signs of contamination by the 2nd day after seeding, which required the termination of the procedure. Out of the contaminated devices, only 2 were recovered. The cells and fibronectin coating were cleaned out, with Accutase cell detachment solution, and the OT and SNR of the devices were reassessed. The changes and observations are discussed in Section 5.2.1. Due to the issues encountered during the cell growth stage of the biocompatibility test, neither the biocompatibility nor the voltage mapping procedure could be carried out. It is important to consider that the observed Mo degradation, during the soak and ageing tests, may be a problematic factor for the biocompatibility of the device as it is toxic in large doses [96].

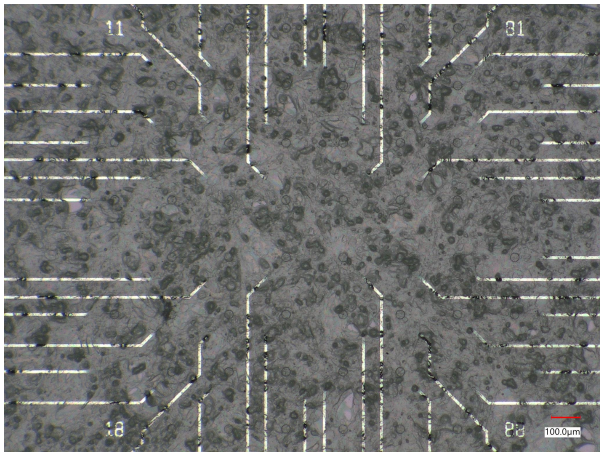

Figure 5.21: gMEA seeded with optogenetic cardiomyocytes. Electrode openings and tracks are visible in the image.

The devices showed no signs of contamination after the 2-day soak test, and the contamination took place after the seeding of the cells. The 2-day soak test is a good indicator that the contamination did arise from the seeding of the cells. However, since no control was used in the experiment, the origin

of the contamination cannot be accurately traced back. As such, UV sterilisation was explored as an alternative method for our devices.

UV Sterilisation Test

Given the known sensitivity of parylene C to UV exposure, we closely monitored its effects through OT measurements conducted both before and after UV exposure. The devices were subjected to one or two doses of 9.999 J/cm². To assess sterility, one sample from each exposure group was immersed in a culture medium for two days. Just as with ethanol sterilisation, no signs of contamination were observed in any of the devices, confirming the effectiveness of the UV approach.

Post-sterilisation, all samples underwent OT measurements. It was noted that UV sterilisation reduced the devices' transparency to wavelengths ranging from 300 nm to 430 nm. For most cases, there was an observed increase in OT at wavelengths from 430 nm to 1200 nm [Fig. 5.22].

These reduced OT values between $\sim$ 300 to 400 nm are caused by photo-oxidation of parylene C during UV exposure and are consistent with other studies [145]. While this is not a concern for our specific purpose, given that hiAM-CheRiff cells are photostimulated with 450 nm light, large UV exposure doses ($> 12J/cm^2$) can cause the deterioration of paryene C [148]. Thus, using this sterilisation approach for future versions of the gMEA (assuming encapsulation layer impermeability), may compromise the parylene C layer integrity and limit the functional life of the device. Nonetheless, a more detailed investigation into the effects of UV sterilisation on the parylene C layer of the device is required to draw accurate conclusions.

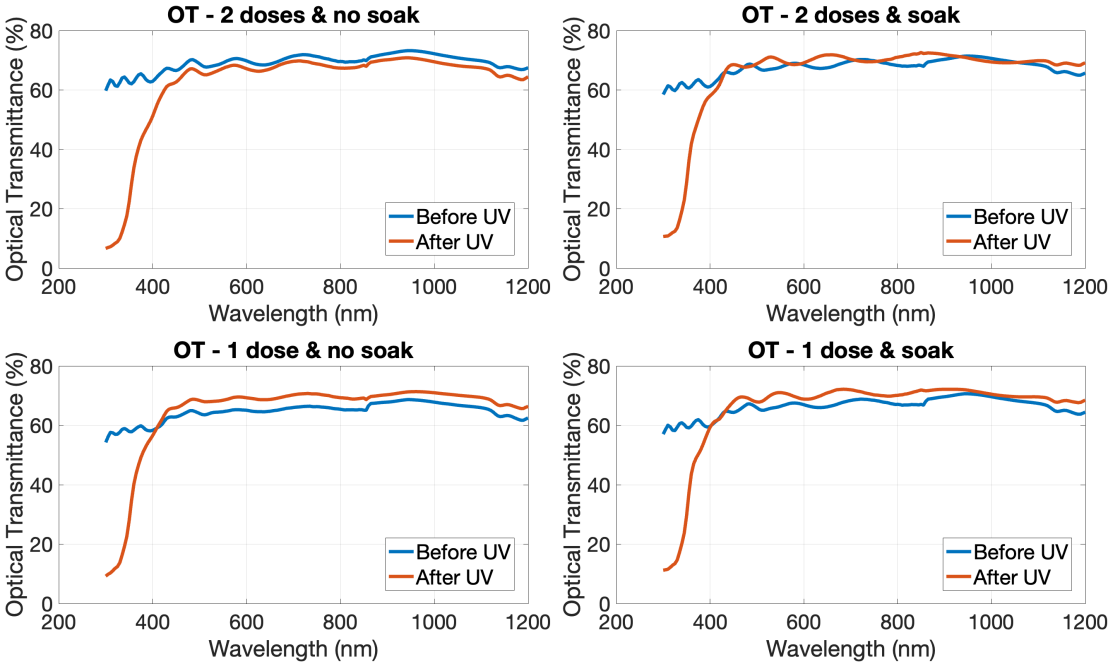

Figure 5.22: Optical transmittance measurements of devices sterilised with UV approach.

5.3. Summary of Main Findings

Graphene growth was achieved on quartz and sapphire substrates using a transfer-free method [24]. The resulting graphene displayed turbostratic stacking characteristics and more defects compared to graphene grown on silicon using the same method. Notably, the removal of Mo during the process was identified as the most detrimental step, often leading to sample delamination. Quartz was chosen as the preferred substrate due to its resistance to graphene delamination. OT measurements confirmed the growth of $\sim$ 10 layers of graphene on quartz.

The initial characterization of the gMEAs revealed a baseline noise of $\sim$ 23 μV. While this noise level enabled the detection of larger amplitude stimulations at 1 V, it hindered and overwhelmed those

at 100 mV and 10 mV, respectively. Further examination through EIS showed an impedance at 1 kHz ranging from 3.2 to 9.89 $M\Omega$, substantially higher than in other studies. However, when area normalised, the impedance remained comparable to reported values. The photosensitivity test yielded inconclusive results but indicated a sensitivity of the devices to the power line noise.

In comparison to a commercial MCS-MEA, the gMEAs exhibited lower performance, having a baseline noise nearly six times larger. Despite this, the recorded signal amplitude of gMEAs surpassed that of MCS-MEAs. Furthermore, the commercial devices showed sensitivity to photostimulation but were unaffected by power line noise.

Device characterisation through optical microscopy and OT after the soaking and ageing tests demonstrated the permeability of the encapsulation layer and the biodegradability of Mo structures. These factors significantly influenced the outcomes of subsequent electrochemical measurements, highlighting the low stability of the gMEAs.

6

Conclusions and Future Work

6.1. Conclusions

In this study, we successfully grew multilayer graphene on both quartz and sapphire substrates through a transfer-free method using Mo as a catalyst. Among the substrates tested, graphene on sapphire was more prone to delamination during the Mo removal process. However, neither matched the quality and delamination resistance of graphene grown with the same catalyst on thermally oxidised silicon. Through OT assessments, it was estimated that $\sim$ 10 layers of graphene were synthesised on quartz under optimal conditions. Although the produced graphene did not attain high quality, this thesis demonstrates the feasibility of direct graphene growth on transparent substrates through a transfer-free approach. Further refinement of the graphene growth recipe on quartz and sapphire holds the promise of enhancing the quality of obtained graphene.

This novel approach for graphene growth on quartz enabled the successful fabrication of transparent gMEAs, which, upon initial testing, demonstrated their capability to detect stimuli injected in the PBS filling the growing well. Despite the gMEAs presenting a relatively high baseline noise of $\sim 23\ \mu V$, they achieved significant signal detection at stimulations of 1 V and 100 mV. This resulted in a satisfactory SNR for 1 V stimulations and an average SNR $>$ 1 for 100 mV stimulations, sufficient for signal detection. In comparison, commercially available MCS-MEAs exhibited significantly lower baseline noise, 5.7 times smaller, but lower signal detection levels for the same stimulations. MCS-MEAs recorded higher SNR across all tests due to their lower noise levels. However, the experimental setup used is a limiting factor when drawing conclusions on the relationship between stimulation amplitude and recorded signals. This arises from the separation between stimulating and recording electrodes, which leads to signal dissipation in PBS, making the voltage reaching the electrodes unknown.

The study also explored the photosensitivity of the gMEA devices. However, due to significant noise at low frequencies overlapping with the photostimulation signals, and the potential presence and influence of photosensitive compounds like MoO_3, the findings were inconclusive. Furthermore, a distinct peak at 50 Hz confirmed the influence of the power line interference on the devices. In contrast, the absence of overlapping noise in the signals from commercial MEAs, enabled the detection of photoinduced artifacts, thus proving their sensitivity to light stimuli. Additionally, the 50 Hz peak phenomenon was not observed.

Further assessments through EIS revealed that the impedance of gMEAs at 1 kHz was higher than previously reported, ranging from 3.2 to 9.89 MΩ, whereas area-normalised impedance values were comparable, but on the higher end. This may be due to a lower graphene quality or to the Mo degradation taking place near the electrode. Nonetheless, arriving at a definitive conclusion requires a more thorough analysis to differentiate between the potential influences of lower graphene quality and Mo degradation.

The stability tests of the devices highlighted several issues, primarily attributed to the permeability of the encapsulation layer and the biodegradability of Mo structures. Observations under optical microscopy revealed defects such as delamination of parylene C, salt deposits beneath the parylene C, and Mo degradation, marked by an increased OT. A re-evaluation of the recording properties showed a noticeable decrease in both noise ($\sim$ 10 μV) and signal amplitude, with noise levels of the gMEAs

being 2.5 times higher than that of the commercial devices, yet with comparable signal sensitivity. Thus, the commercial MEAs still boasted a significantly higher SNR due to their lower baseline noise. The impedance at 1 kHz also showed a dramatic decrease, in most cases dropping by $\sim$ 99% of the original value by the tenth day of the ageing test. The drastic changes observed in SNR and EIS highlight the impact of conductive structure alterations and other issues on device performance, such as liquid-induced short-circuits. The same failure mechanisms are responsible for the breakage and dissolution of gold tracks during CV tests, further emphasising the challenges posed by the encapsulation layer's permeability.

In the final phase of our study, we intended to assess the biocompatibility of our devices; however, the cell cultures became contaminated during the seeding process, preventing any in-vitro experiments from being conducted. While the contamination's source appeared unrelated to the devices themselves, this incident led to the exploration of UV sterilisation as a more effective alternative compared to standard ethanol sterilisation. Devices subjected to single and double UV doses of 9.999 J/cm^2 exhibited substantial reductions in OT across the 300 - 430 nm wavelength range. Importantly, none of the devices treated with UV sterilisation showed signs of contamination after a 2-day soak test, suggesting the efficacy of UV sterilisation. In addition, it is essential to acknowledge that a potential biocompatibility concern for these devices is the degradation of Mo structures, as elevated doses of Mo have been reported to be toxic. Due to the unexpected contamination of cell cultures and time constraints, we were unable to address the question of whether transfer-free graphene is biocompatible. Nonetheless, this thesis lays the groundwork for future research attempts aiming to answer this question.

6.2. Future Work

In this thesis, we successfully grew graphene directly on quartz and sapphire substrates using a transfer-free approach. However, achieving high-quality graphene proved challenging with the temperature parameters explored. To address this, a more comprehensive investigation into the impact of additional factors, such as growth time, gas flow, and pressure, on graphene synthesis for these substrates would be valuable.

While testing graphene samples grown on the various substrates, we observed carbon-compound associated peaks in the Raman spectra. These peaks were attributed to carbon-compounds formed during the graphene growth process and only became detectable with Raman spectroscopy after removing Mo. We also observed a reduction in the unwanted peaks after the ethanol sterilisation procedure. Thus, to improve the graphene quality, we recommend attempting the removal of these residues through a more thorough cleaning procedure.

While the gMEA was successfully fabricated and demonstrated it was capable of recording signals, it exhibited a high baseline noise and an impedance at 1 kHz, significantly exceeding literature values. SNR measurements and microscopy images, taken after short liquid exposures, showed baseline noise improvement as Mo near the electrodes began to degrade. As such we can assume that Mo compounds derived from its degradation play a role in the electrochemical impedance of the device. Thus, the complete removal of Mo from the gMEA may enhance the recording quality and potentially reduce the impedance. Nonetheless, the addition of an alternative conductor may be needed to reduce the high resistance of bare graphene tracks, which can increase the impedance. We also faced stability issues due to the encapsulation layer's permeability and the subsequent degradation of Mo structures. Accurate performance assessment of gMEAs requires addressing these issues, starting with the development of an impermeable encapsulation layer. Improvements may be achieved through a thicker parylene C layer, improving the adhesion to the gMEA by ensuring a good vacuum before CVD or using appropriate adhesion-promoting techniques, and the use of alternative materials such as PDMS or non-polymeric materials like SiO_2. Additionally, eliminating all Mo from the device and closing the $\sim$ 50 nm gap left by its removal will prevent liquid infiltration through the electrode openings and associated alterations of the electrical properties due to Mo degradation. Using wider graphene tracks might also reduce resistance and lower the impedance.

Assessment methods may also benefit from some refinement. The current setup for SNR assessment, with the stimulating electrode placed far from the gMEA, diminishes the stimulation amplitude as it travels through PBS. Placing the stimulating electrode closer to the gMEA and using smaller voltages may provide a better understanding of the electrodes' sensitivity. A holder for the stimulating electrode, similar to the one used in EIS measurements, could ensure consistent electrode positioning across

tests. Furthermore, increasing the stimulation frequency to 10 Hz for the photoinduced artifact test could help distinguish artifacts from the low-frequency noise, ensuring the stimulation peak and any harmonics are at higher frequencies than the background noise.

Finally, new devices must be evaluated for biocompatibility and their ability to detect cardiomyocyte action potentials and support optogenetic stimulation. The use of mice cardiomyocyte cells as an alternative to hiAM-CheRiff cell lines may be viable if contamination issues persist. These cells can be cultured with antibiotics, reducing infection risks. However, optogenetically modified mice cardiomyocyte cells were not available to us at LUMC, thus electrical pacing would be necessary, potentially introducing artifacts in the recorded signals.

6.3. Recommendations

This section intends to offer a compilation of practical recommendations to guide subsequent work. The recommendations are directed to the design and microfabrication of the gMEA.

6.3.1. Avoid Oxygen Plasma on Mo Structures

In the standard positive photoresist removal process, oxygen plasma, often applied in the TEPLA, is a commonly employed method. However, in the course of our project, we observed the unintended formation of oxide layers on Mo structures when utilising oxygen plasma for removing photoresist remnants after Mo etching. Given that this oxide layer may interfere with the subsequent graphene growth process, its removal becomes essential before proceeding with this step. To mitigate the formation of Mo oxides on the patterned surface, we recommend opting for the photoresist removal program available on the spin coater. This program involves rinsing the wafer with acetone followed by a subsequent rinse with IPA, resulting in an effective and thorough removal process.

6.3.2. Photoresist Removal

Photoresist plays a crucial role in the fabrication of gMEAs, generally proving uncomplicated. However, challenges arise under specific conditions, such as when utilising a negative photoresist or exposing the material to plasma or high temperatures. Negative photoresist, for instance, demands meticulous removal, achievable with NI555 overnight at room temperature, as demonstrated in the liftoff step during fabrication. It is essential to renew NI555 between wafers to ensure complete removal and prevent potential issues like a cloudy appearance of MEAs after parylene C deposition.

Conversely, removing plasma-exposed or hard-baked photoresist proves difficult, and we have yet to identify a suitable method to eliminate residues effectively. This becomes particularly problematic post-etching of openings on parylene C, where particles and film remnants of photoresist persist, especially in electrode openings, potentially causing partial blockage. In our project, we resorted to cautiously swiping a cotton bud soaked in IPA around the openings, significantly reducing photoresist remnants. However, this method falls short of complete removal and occasionally results in scratches on the parylene C, sometimes cutting through to the tracks.

For future work, we strongly recommend ensuring thorough photoresist removal before proceeding to subsequent steps. Additionally, avoiding the use of a photoresist hard mask during the etching of openings on the parylene C layer can prevent the formation of persistent photoresist residues, contributing to a smoother fabrication process.

6.3.3. Landing Pads

Landing pads serve the purpose of safeguarding graphene electrodes during the creation of openings on the parylene C using oxygen plasma. In the device's design, we deliberately crafted landing pads smaller than the graphene area to ensure proper adherence of graphene to the parylene C layer after the removal of the landing pad. However, a photoresist hard mask is vulnerable to widening of the openings, occasionally leading to exposure of graphene beyond the intended protection from plasma etching. Consequently, the central area of the graphene electrode becomes disconnected from the track.

To mitigate this issue, we adopted a precautionary approach by employing shorter etching times and regularly inspecting the openings under a microscope. Despite this diligence, the process proved time-consuming. In future endeavours, we recommend the incorporation of a metal hard mask during the etching step to prevent unintended widening of the openings. Alternatively, expanding the dimensions

of both the graphene electrode and landing pad could provide a larger margin of error during the oxygen plasma etching step and accommodate potential misalignment issues during the microfabrication process.

6.3.4. Electrode Opening Features for Improved Adhesion

In the initial device design, we incorporated small openings on half of the produced devices' electrode surfaces intending to enhance metal layer adhesion by providing anchor points to the substrate. However, in our study, we observed no instances of delamination for the landing pads, whether they were associated with electrodes featuring openings or those with solid surfaces. Based on these findings, we recommend that future projects employing metal features on graphene, with dimensions similar to the electrodes produced in this study, may consider using solid electrodes, as there was no apparent advantage observed in terms of delamination prevention with the inclusion of small openings.

6.3.5. MEA Contact Pads

While attempting the wire bonding of MEAs to the PCB through Al wire wedge wire bonding, we encountered a significant challenge stemming from the low adhesion of the Au/Ti layer to the substrate. This issue manifested in the delamination of the bonded area from the substrate as soon as the wire bonder needle was retracted. To address this, we opted for Au ball-wedge wire bonding, as it offered a viable solution. However, due to equipment restrictions and the expertise required, a technician had to perform the wire bonding.

The low adhesion of the Au/Ti layer not only poses challenges during wire bonding but also raises concerns about the potential delamination of other circuit components. Presently, the only adhesion 'enhancement' technique involved leaving the CHA Solutions chamber venting overnight to ensure optimal vacuum conditions before metal layer deposition. For future endeavours, we recommend focusing on improving adhesion to the substrate. Exploring active adhesion enhancement techniques beyond the current practice could prove beneficial in addressing these challenges more effectively.

6.3.6. Space for Growing Well

The existing dies were designed with minimal spacing between electrodes and contact pads to accommodate the growing well. However, this design choice resulted in several complications. Firstly, during the attachment of the growing well, epoxy covered portions of the return electrode due to its proximity to the well. This unintentional coverage reduces the surface area of the return electrode, potentially compromising signal quality by increasing impedance and baseline noise.

Moreover, feedback from LUMC technicians during soaking tests and cell growth procedures highlighted the preference for a larger well capable of holding a greater volume of culture medium. To address these issues proactively in future iterations, we recommend increasing the distance between electrodes and contact pads, as well as enlarging the die size. For instance, considering a 30 x 30 mm die for the device could provide the necessary space for efficient well attachment and alleviate the concerns related to signal quality and well capacity.

References

[1] Xiaowei Du et al. 'Graphene microelectrode arrays for neural activity detection'. In: *Journal of Biological Physics* 41.4 (1st Sept. 2015), pp. 339–347. ISSN: 1573-0689. DOI: 10.1007/s10867-015-9382-3. URL: https://doi.org/10.1007/s10867-015-9382-3.

[2] Sepideh Rastegar et al. 'Measurement of Signal-to-Noise Ratio In Graphene-based Passive Microelectrode Arrays'. In: *Electroanalysis* 31.6 (2019), pp. 991–1001. ISSN: 1521-4109. DOI: 10.1002/elan.201800745. URL: https://onlinelibrary.wiley.com/doi/abs/10.1002/elan.201800745.

[3] Nicolette Driscoll et al. 'Multimodal in vivo recording using transparent graphene microelectrodes illuminates spatiotemporal seizure dynamics at the microscale'. In: *Communications Biology* 4.1 (29th Jan. 2021). Publisher: Nature Publishing Group, pp. 1–14. ISSN: 2399-3642. DOI: 10.1038/s42003-021-01670-9. URL: https://www.nature.com/articles/s42003-021-01670-9.

[4] Dmitry Kireev et al. 'Versatile Flexible Graphene Multielectrode Arrays'. In: *Biosensors* 7.1 (Mar. 2017). Publisher: Multidisciplinary Digital Publishing Institute, p. 1. ISSN: 2079-6374. DOI: 10.3390/bios7010001. URL: https://www.mdpi.com/2079-6374/7/1/1.

[5] Duygu Kuzum et al. 'Transparent and flexible low noise graphene electrodes for simultaneous electrophysiology and neuroimaging'. In: *Nature Communications* 5.1 (20th Oct. 2014). Publisher: Nature Publishing Group, p. 5259. ISSN: 2041-1723. DOI: 10.1038/ncomms6259. URL: https://www.nature.com/articles/ncomms6259.

[6] Mehrdad Ramezani et al. 'High-density transparent graphene arrays for predicting cellular calcium activity at depth from surface potential recordings'. In: *Nature Nanotechnology* (11th Jan. 2024). Publisher: Nature Publishing Group, pp. 1–10. ISSN: 1748-3395. DOI: 10.1038/s41565-023-01576-z. URL: https://www.nature.com/articles/s41565-023-01576-z.

[7] Samarendra K. Mohanty and Vasudevan Lakshminarayananan. 'Optical Techniques in Optogenetics'. In: *Journal of modern optics* 62.12 (2015), pp. 949–970. ISSN: 0950-0340. DOI: 10.1080/09500340.2015.1010620. URL: https://www.ncbi.nlm.nih.gov/pmc/articles/PMC4582796/.

[8] Wenqing Chen et al. 'The Roles of Optogenetics and Technology in Neurobiology: A Review'. In: *Frontiers in Aging Neuroscience* 14 (19th Apr. 2022), p. 867863. ISSN: 1663-4365. DOI: 10.3389/fnagi.2022.867863. URL: https://www.ncbi.nlm.nih.gov/pmc/articles/PMC9063564/.

[9] Hubin Zhao. 'Recent Progress of Development of Optogenetic Implantable Neural Probes'. In: *International Journal of Molecular Sciences* 18.8 (11th Aug. 2017), p. 1751. ISSN: 1422-0067. DOI: 10.3390/ijms18081751. URL: https://www.ncbi.nlm.nih.gov/pmc/articles/PMC5578141/.

[10] Marleen Welkenhuysen et al. 'An integrated multi-electrode-optrode array for in vitro optogenetics'. In: *Scientific Reports* 6.1 (2nd Feb. 2016), p. 20353. ISSN: 2045-2322. DOI: 10.1038/srep20353. URL: https://www.nature.com/articles/srep20353.

[11] Anna Susloparova et al. 'Low impedance and highly transparent microelectrode arrays (MEA) for in vitro neuron electrical activity probing'. In: *Sensors and Actuators B: Chemical* 327 (15th Jan. 2021), p. 128895. ISSN: 0925-4005. DOI: 10.1016/j.snb.2020.128895. URL: https://www.sciencedirect.com/science/article/pii/S0925400520312429.

[12] Vijay Viswam et al. 'Optimal Electrode Size for Multi-Scale Extracellular-Potential Recording From Neuronal Assemblies'. In: *Frontiers in Neuroscience* 13 (2019). ISSN: 1662-453X. URL: https://www.frontiersin.org/journals/neuroscience/articles/10.3389/fnins.2019.00385.

[13] E. Entcheva et al. ‘Fluorescence imaging of electrical activity in cardiac cells using an all-solid-state system’. In: *IEEE Transactions on Biomedical Engineering* 51.2 (Feb. 2004). Conference Name: IEEE Transactions on Biomedical Engineering, pp. 333–341. ISSN: 1558-2531. DOI: 10.1109/TBME.2003.820376. URL: https://ieeexplore.ieee.org/abstract/document/1262111?casa_token=sFbwH8kXo5QAAAAA:AzCDFKSBaw-llnqt8-x3lgx1zSf4RD31uw0DRGwuF9p2VM53XuXpRad0RiMLy-Mc6oI4_Ogb.

[14] S. Chemla and F. Chavane. ‘Voltage-sensitive dye imaging: Technique review and models’. In: *Journal of Physiology-Paris*. Computational Neuroscience, from Multiple Levels to Multi-level 104.1 (1st Jan. 2010), pp. 40–50. ISSN: 0928-4257. DOI: 10.1016/j.jphysparis.2009.11.009. URL: https://www.sciencedirect.com/science/article/pii/S0928425709000916.

[15] Leslie M. Loew. ‘Design and Use of Organic Voltage Sensitive Dyes’. In: *Membrane Potential Imaging in the Nervous System and Heart*. Ed. by Marco Canepari, Dejan Zecevic and Olivier Bernus. Advances in Experimental Medicine and Biology. Cham: Springer International Publishing, 2015, pp. 27–53. ISBN: 978-3-319-17641-3. DOI: 10.1007/978-3-319-17641-3_2. URL: https://doi.org/10.1007/978-3-319-17641-3_2.

[16] Schuyler B VanEngelenburg and Amy E Palmer. ‘Fluorescent biosensors of protein function’. In: *Current Opinion in Chemical Biology* 12.1 (1st Feb. 2008), pp. 60–65. ISSN: 1367-5931. DOI: 10.1016/j.cbpa.2008.01.020. URL: https://www.sciencedirect.com/science/article/pii/S1367593108000124.

[17] Takeaki Ozawa, Hideaki Yoshimura and Sung Bae Kim. ‘Advances in Fluorescence and Bioluminescence Imaging’. In: *Analytical Chemistry* 85.2 (15th Jan. 2013). Publisher: American Chemical Society, pp. 590–609. ISSN: 0003-2700. DOI: 10.1021/ac3031724. URL: https://doi.org/10.1021/ac3031724.

[18] Chenfei Hu et al. ‘Optical excitation and detection of neuronal activity’. In: *Journal of Biophotonics* 12.3 (2019), e201800269. ISSN: 1864-0648. DOI: 10.1002/jbio.201800269. URL: https://onlinelibrary.wiley.com/doi/abs/10.1002/jbio.201800269.

[19] Yuecheng Zhou et al. ‘Optical Electrophysiology: Toward the Goal of Label-Free Voltage Imaging’. In: *Journal of the American Chemical Society* 143.28 (21st July 2021). Publisher: American Chemical Society, pp. 10482–10499. ISSN: 0002-7863. DOI: 10.1021/jacs.1c02960. URL: https://doi.org/10.1021/jacs.1c02960.

[20] Michael J. Sanderson et al. ‘Fluorescence Microscopy’. In: *Cold Spring Harbor protocols* 2014.10 (1st Oct. 2014), pdb.top071795. ISSN: 1940-3402. DOI: 10.1101/pdb.top071795. URL: https://www.ncbi.nlm.nih.gov/pmc/articles/PMC4711767/.

[21] John. F. Wager. ‘Transparent Electronics’. In: *Science* 300.5623 (23rd May 2003). Publisher: American Association for the Advancement of Science, pp. 1245–1246. DOI: 10.1126/science.1085276. URL: https://www-science-org.tudelft.idm.oclc.org/doi/full/10.1126/science.1085276.

[22] Daeyeon Won et al. ‘Transparent Electronics for Wearable Electronics Application’. In: *Chemical Reviews* 123.16 (23rd Aug. 2023). Publisher: American Chemical Society, pp. 9982–10078. ISSN: 0009-2665. DOI: 10.1021/acs.chemrev.3c00139. URL: https://doi.org/10.1021/acs.chemrev.3c00139.

[23] Sahil Kumar Rastogi et al. ‘Graphene Microelectrode Arrays for Electrical and Optical Measurements of Human Stem Cell-Derived Cardiomyocytes’. In: *Cellular and Molecular Bioengineering* 11.5 (1st Oct. 2018), pp. 407–418. ISSN: 1865-5033. DOI: 10.1007/s12195-018-0525-z. URL: https://doi.org/10.1007/s12195-018-0525-z.

[24] S. Vollebregt et al. ‘A transfer-free wafer-scale CVD graphene fabrication process for MEMS/NEMS sensors’. In: *2016 IEEE 29th International Conference on Micro Electro Mechanical Systems (MEMS)*. 2016 IEEE 29th International Conference on Micro Electro Mechanical Systems (MEMS). Jan. 2016, pp. 17–20. DOI: 10.1109/MEMSYS.2016.7421546. URL: https://ieeexplore.ieee.org/document/7421546.

[25] Shihong Xu et al. 'Recent Progress and Perspectives on Neural Chip Platforms Integrating PDMS-Based Microfluidic Devices and Microelectrode Arrays'. In: *Micromachines* 14.4 (23rd Mar. 2023), p. 709. ISSN: 2072-666X. DOI: 10.3390/mi14040709. URL: https://www.ncbi.nlm.nih.gov/pmc/articles/PMC10145465/.

[26] Yaoyao Liu et al. 'Nanomaterial-based microelectrode arrays for in vitro bidirectional brain–computer interfaces: a review'. In: *Microsystems & Nanoengineering* 9 (30th Jan. 2023), p. 13. ISSN: 2096-1030. DOI: 10.1038/s41378-022-00479-8. URL: https://www.ncbi.nlm.nih.gov/pmc/articles/PMC9884667/.

[27] Reem M. Almasri et al. 'Emerging trends in the development of flexible optrode arrays for electrophysiology'. In: *APL Bioengineering* 7.3 (7th Sept. 2023), p. 031503. ISSN: 2473-2877. DOI: 10.1063/5.0153753. URL: https://www.ncbi.nlm.nih.gov/pmc/articles/PMC10491464/.

[28] Henrique Teixeira et al. 'Gold-Mushroom Microelectrode Arrays and the Quest for Intracellular-Like Recordings: Perspectives and Outlooks'. In: *Advanced Materials Technologies* 6.2 (2021), p. 2000770. ISSN: 2365-709X. DOI: 10.1002/admt.202000770. URL: https://onlinelibrary.wiley.com/doi/abs/10.1002/admt.202000770.

[29] Micha E. Spira and Aviad Hai. 'Multi-electrode array technologies for neuroscience and cardiology'. In: *Nature Nanotechnology* 8.2 (Feb. 2013), pp. 83–94. ISSN: 1748-3395. DOI: 10.1038/nnano.2012.265. URL: https://www.nature.com/articles/nnano.2012.265.

[30] Yuya Sato et al. 'Microfluidic cell engineering on high-density microelectrode arrays for assessing structure-function relationships in living neuronal networks'. In: *Frontiers in Neuroscience* 16 (2023). ISSN: 1662-453X. URL: https://www.frontiersin.org/articles/10.3389/fnins.2022.943310.

[31] Victor Dupuit, Anne Briançon-Marjollet and Cécile Delacour. 'Portrait of intense communications within microfluidic neural networks'. In: *Scientific Reports* 13.1 (29th July 2023). Publisher: Nature Publishing Group, p. 12306. ISSN: 2045-2322. DOI: 10.1038/s41598-023-39477-9. URL: https://www.nature.com/articles/s41598-023-39477-9.

[32] Martina Brofiga et al. 'Multiple neuron clusters on Micro-Electrode Arrays as an in vitro model of brain network'. In: *Scientific Reports* 13.1 (20th Sept. 2023). Publisher: Nature Publishing Group, p. 15604. ISSN: 2045-2322. DOI: 10.1038/s41598-023-42168-0. URL: https://www.nature.com/articles/s41598-023-42168-0.

[33] Hyogeun Shin et al. 'Neural probes with multi-drug delivery capability'. In: *Lab on a Chip* 15.18 (25th Aug. 2015). Publisher: The Royal Society of Chemistry, pp. 3730–3737. ISSN: 1473-0189. DOI: 10.1039/C5LC00582E. URL: https://pubs.rsc.org/en/content/articlelanding/2015/lc/c5lc00582e.

[34] Hongbian Li, Jinfen Wang and Ying Fang. 'Recent developments in multifunctional neural probes for simultaneous neural recording and modulation'. In: *Microsystems & Nanoengineering* 9.1 (4th Jan. 2023). Publisher: Nature Publishing Group, pp. 1–13. ISSN: 2055-7434. DOI: 10.1038/s41378-022-00444-5. URL: https://www.nature.com/articles/s41378-022-00444-5.

[35] Yi Qiang et al. 'Transparent arrays of bilayer-nanomesh microelectrodes for simultaneous electrophysiology and two-photon imaging in the brain'. In: *Science Advances* 4.9 (5th Sept. 2018). Publisher: American Association for the Advancement of Science, eaat0626. DOI: 10.1126/sciadv.aat0626. URL: https://www-science-org.tudelft.idm.oclc.org/doi/full/10.1126/sciadv.aat0626.

[36] Brahim Aïssa et al. 'Recent Progress in the Growth and Applications of Graphene as a Smart Material: A Review'. In: *Frontiers in Materials* 2 (2015). ISSN: 2296-8016. URL: https://www.frontiersin.org/articles/10.3389/fmats.2015.00058.

[37] Hamza El Etri. 'Graphene: A State-of-the-Art Review of Types, Properties and Applications in Different Sectors'. In: *Prabha Materials Science Letters* 2 (14th Aug. 2023). DOI: 10.33889/PMSL.2023.2.2.009.

[38] Rebecca S. Edwards and Karl S. Coleman. 'Graphene synthesis: relationship to applications'. In: *Nanoscale* 5.1 (7th Dec. 2012). Publisher: The Royal Society of Chemistry, pp. 38–51. ISSN: 2040-3372. DOI: 10.1039/C2NR32629A. URL: https://pubs.rsc.org/en/content/articlelanding/2013/nr/c2nr32629a.

[39] Zhen Zhen and Hongwei Zhu. '1 - Structure and Properties of Graphene'. In: *Graphene*. Ed. by Hongwei Zhu et al. Academic Press, 1st Jan. 2018, pp. 1–12. ISBN: 978-0-12-812651-6. DOI: 10.1016/B978-0-12-812651-6.00001-X. URL: https://www.sciencedirect.com/science/article/pii/B978012812651600001X.

[40] A. H. Castro Neto et al. 'The electronic properties of graphene'. In: *Reviews of Modern Physics* 81.1 (14th Jan. 2009), pp. 109–162. ISSN: 0034-6861, 1539-0756. DOI: 10.1103/RevModPhys.81.109. URL: https://link.aps.org/doi/10.1103/RevModPhys.81.109.

[41] Artur T. Dideikin and Alexander Y. Vul'. 'Graphene Oxide and Derivatives: The Place in Graphene Family'. In: *Frontiers in Physics* 6 (2019). ISSN: 2296-424X. URL: https://www.frontiersin.org/articles/10.3389/fphy.2018.00149.

[42] Poulomi Das et al. 'Stepwise reduction of graphene oxide and studies on defect-controlled physical properties'. In: *Scientific Reports* 14.1 (2nd Jan. 2024). Publisher: Nature Publishing Group, p. 294. ISSN: 2045-2322. DOI: 10.1038/s41598-023-51040-0. URL: https://www.nature.com/articles/s41598-023-51040-0.

[43] Nasim Bakhshaee Babaroud et al. 'Multilayer CVD graphene electrodes using a transfer-free process for the next generation of optically transparent and MRI-compatible neural interfaces'. In: *Microsystems & Nanoengineering* 8.1 (26th Sept. 2022). Publisher: Nature Publishing Group, pp. 1–14. ISSN: 2055-7434. DOI: 10.1038/s41378-022-00430-x. URL: https://www.nature.com/articles/s41378-022-00430-x.

[44] K. S. Novoselov et al. 'Electric Field Effect in Atomically Thin Carbon Films'. In: *Science* 306.5696 (22nd Oct. 2004). Publisher: American Association for the Advancement of Science, pp. 666–669. DOI: 10.1126/science.1102896. URL: https://www-science-org.tudelft.idm.oclc.org/doi/10.1126/science.1102896.

[45] Hui Huang et al. 'Highly efficient electrolytic exfoliation of graphite into graphene sheets based on Li ions intercalation–expansion–microexplosion mechanism'. In: *Journal of Materials Chemistry* 22.21 (8th May 2012). Publisher: The Royal Society of Chemistry, pp. 10452–10456. ISSN: 1364-5501. DOI: 10.1039/C2JM00092J. URL: https://pubs.rsc.org/en/content/articlelanding/2012/jm/c2jm00092j.

[46] Filiberto Ricciardella et al. 'Wafer-scale transfer-free process of multi-layered graphene grown by chemical vapor deposition'. In: *Materials Research Express* 7.3 (1st Mar. 2020), p. 035001. ISSN: 2053-1591. DOI: 10.1088/2053-1591/ab771e. URL: https://iopscience.iop.org/article/10.1088/2053-1591/ab771e.

[47] Qingsong Huang et al. 'Epitaxial graphene on 4H-SiC by pulsed electron irradiation'. In: *Chemical Communications* 46.27 (29th June 2010). Publisher: The Royal Society of Chemistry, pp. 4917–4919. ISSN: 1364-548X. DOI: 10.1039/C000175A. URL: https://pubs.rsc.org/en/content/articlelanding/2010/cc/c000175a.

[48] Spyros N. Yannopoulos et al. 'CO2-Laser-Induced Growth of Epitaxial Graphene on 6H-SiC(0001)'. In: *Advanced Functional Materials* 22.1 (2012), pp. 113–120. ISSN: 1616-3028. DOI: 10.1002/adfm.201101413. URL: https://onlinelibrary.wiley.com/doi/abs/10.1002/adfm.201101413.

[49] Jiang-Bin Wu et al. 'Raman spectroscopy of graphene-based materials and its applications in related devices'. In: *Chemical Society Reviews* 47.5 (5th Mar. 2018). Publisher: The Royal Society of Chemistry, pp. 1822–1873. ISSN: 1460-4744. DOI: 10.1039/C6CS00915H. URL: https://pubs.rsc.org/en/content/articlelanding/2018/cs/c6cs00915h.

[50] L. M. Malard et al. 'Raman spectroscopy in graphene'. In: *Physics Reports* 473.5 (1st Apr. 2009), pp. 51–87. ISSN: 0370-1573. DOI: 10.1016/j.physrep.2009.02.003. URL: https://www.sciencedirect.com/science/article/pii/S0370157309000520.

[51] Andrea C. Ferrari and Denis M. Basko. 'Raman spectroscopy as a versatile tool for studying the properties of graphene'. In: *Nature Nanotechnology* 8.4 (Apr. 2013). Publisher: Nature Publishing Group, pp. 235–246. ISSN: 1748-3395. DOI: 10.1038/nnano.2013.46. URL: https://www.nature.com/articles/nnano.2013.46.

[52] Thomas H. Kauffmann, Ninel Kokanyan and Marc D. Fontana. 'Use of Stokes and anti-Stokes Raman scattering for new applications'. In: *Journal of Raman Spectroscopy* 50.3 (2019), pp. 418–424. ISSN: 1097-4555. DOI: 10.1002/jrs.5523. URL: https://onlinelibrary.wiley.com/doi/abs/10.1002/jrs.5523.

[53] Jian Zeng et al. 'Irradiation effects of graphene and thin layer graphite induced by swift heavy ions*'. In: *Chinese Physics B* 24.8 (June 2015). Publisher: IOP Publishing, p. 086103. ISSN: 1674-1056. DOI: 10.1088/1674-1056/24/8/086103. URL: https://dx.doi.org/10.1088/1674-1056/24/8/086103.

[54] Shou-En Zhu, Shengjun Yuan and G. C. A. M. Janssen. 'Optical transmittance of multilayer graphene'. In: *Europhysics Letters* 108.1 (Sept. 2014). Publisher: EDP Sciences, IOP Publishing and Società Italiana di Fisica, p. 17007. ISSN: 0295-5075. DOI: 10.1209/0295-5075/108/17007. URL: https://dx.doi.org/10.1209/0295-5075/108/17007.

[55] Zhongfan Liu et al. 'Chapter 2 - CVD Synthesis of Graphene'. In: *Thermal Transport in Carbon-Based Nanomaterials*. Ed. by Gang Zhang. Micro and Nano Technologies. Elsevier, 1st Jan. 2017, pp. 19–56. ISBN: 978-0-323-46240-2. DOI: 10.1016/B978-0-32-346240-2.00002-9. URL: https://www.sciencedirect.com/science/article/pii/B9780323462402000029.

[56] Andrada I. Velea et al. 'Wafer-Scale Graphene-Based Soft Electrode Array with Optogenetic Compatibility'. In: *2020 IEEE 33rd International Conference on Micro Electro Mechanical Systems (MEMS)*. 2020 IEEE 33rd International Conference on Micro Electro Mechanical Systems (MEMS). ISSN: 2160-1968. Jan. 2020, pp. 421–424. DOI: 10.1109/MEMS46641.2020.9056367. URL: https://ieeexplore.ieee.org/document/9056367.

[57] Kostas Kostarelos et al. 'Graphene in the Design and Engineering of Next-Generation Neural Interfaces'. In: *Advanced Materials* 29.42 (2017), p. 1700909. ISSN: 1521-4095. DOI: 10.1002/adma.201700909. URL: https://onlinelibrary.wiley.com/doi/abs/10.1002/adma.201700909.

[58] Arghya Narayan Banerjee. 'Graphene and its derivatives as biomedical materials: future prospects and challenges'. In: *Interface Focus* 8.3 (6th June 2018). Publisher: Royal Society. DOI: 10.1098/rsfs.2017.0056. URL: https://royalsocietypublishing.org/doi/full/10.1098/rsfs.2017.0056.

[59] Ashkan Aryaei, Ahalapitiya H. Jayatissa and Ambalangodage C. Jayasuriya. 'The effect of graphene substrate on osteoblast cell adhesion and proliferation'. In: *Journal of Biomedical Materials Research Part A* 102.9 (2014), pp. 3282–3290. ISSN: 1552-4965. DOI: 10.1002/jbm.a.34993. URL: https://onlinelibrary.wiley.com/doi/abs/10.1002/jbm.a.34993.

[60] Jaehyeung Park and Mingdi Yan. 'Covalent Functionalization of Graphene with Reactive Intermediates'. In: *Accounts of Chemical Research* 46.1 (15th Jan. 2013). Publisher: American Chemical Society, pp. 181–189. ISSN: 0001-4842. DOI: 10.1021/ar300172h. URL: https://doi.org/10.1021/ar300172h.

[61] Tapas Kuila et al. 'Chemical functionalization of graphene and its applications'. In: *Progress in Materials Science* 57.7 (1st Sept. 2012), pp. 1061–1105. ISSN: 0079-6425. DOI: 10.1016/j.pmatsci.2012.03.002. URL: https://www.sciencedirect.com/science/article/pii/S0079642512000254.

[62] Guangfu Wu et al. 'Chemical functionalization of graphene with aromatic molecule'. In: *2015 IEEE 15th International Conference on Nanotechnology (IEEE-NANO)*. 2015 IEEE 15th International Conference on Nanotechnology (IEEE-NANO). July 2015, pp. 1324–1327. DOI: 10.1109/NANO.2015.7388878. URL: https://ieeexplore.ieee.org/document/7388878.

[63] Josef Jampilek and Katarina Kralova. 'Advances in Drug Delivery Nanosystems Using Graphene-Based Materials and Carbon Nanotubes'. In: *Materials* 14.5 (24th Feb. 2021), p. 1059. ISSN: 1996-1944. DOI: 10.3390/ma14051059. URL: https://www.ncbi.nlm.nih.gov/pmc/articles/PMC7956197/.

[64] Renu Geetha Bai and Ghaleb A. Husseini. 'Graphene-based drug delivery systems'. In: *Biomimetic Nanoengineered Materials for Advanced Drug Delivery*. Ed. by Afeesh Rajan Unnithan et al. Elsevier, 1st Jan. 2019, pp. 149–168. ISBN: 978-0-12-814944-7. DOI: 10.1016/B978-0-12-814944-7.00011-4. URL: https://www.sciencedirect.com/science/article/pii/B9780128149447000114.

[65] Mojtaba Hoseini-Ghahfarokhi et al. 'Applications of Graphene and Graphene Oxide in Smart Drug/Gene Delivery: Is the World Still Flat?' In: *International Journal of Nanomedicine* 15 (27th Nov. 2020), pp. 9469–9496. ISSN: 1176-9114. DOI: 10.2147/IJN.S265876. URL: https://www.ncbi.nlm.nih.gov/pmc/articles/PMC7710865/.

[66] Rana Imani, Fatemeh Mohabatpour and Fatemeh Mostafavi. 'Graphene-based Nano-Carrier modifications for gene delivery applications'. In: *Carbon* 140 (1st Dec. 2018), pp. 569–591. ISSN: 0008-6223. DOI: 10.1016/j.carbon.2018.09.019. URL: https://www.sciencedirect.com/science/article/pii/S0008622318308273.

[67] Andrada Iulia Velea. 'Flexible Graphene-Based Passive and Active Spinal Cord Implants'. PhD thesis. TU Delft, 13th Dec. 2019. 115 pp.

[68] Sahil Kumar Rastogi et al. 'Effect of Graphene on Nonneuronal and Neuronal Cell Viability and Stress'. In: *Nano Letters* 17.5 (10th May 2017). Publisher: American Chemical Society, pp. 3297–3301. ISSN: 1530-6984. DOI: 10.1021/acs.nanolett.7b01215. URL: https://doi.org/10.1021/acs.nanolett.7b01215.

[69] S. Syama and P. V. Mohanan. 'Safety and biocompatibility of graphene: A new generation nanomaterial for biomedical application'. In: *International Journal of Biological Macromolecules* 86 (1st May 2016), pp. 546–555. ISSN: 0141-8130. DOI: 10.1016/j.ijbiomac.2016.01.116. URL: https://www.sciencedirect.com/science/article/pii/S0141813016301180.

[70] Artur M. Pinto, Inês C. Gonçalves and Fernão D. Magalhães. 'Graphene-based materials biocompatibility: A review'. In: *Colloids and Surfaces B: Biointerfaces* 111 (1st Nov. 2013), pp. 188–202. ISSN: 0927-7765. DOI: 10.1016/j.colsurfb.2013.05.022. URL: https://www.sciencedirect.com/science/article/pii/S0927776513003482.

[71] Xiaowei Wu et al. 'A review on the biocompatibility and potential applications of graphene in inducing cell differentiation and tissue regeneration'. In: *Journal of Materials Chemistry B* 5.17 (2017). Publisher: Royal Society of Chemistry, pp. 3084–3102. DOI: 10.1039/C6TB03067J. URL: https://pubs-rsc-org.tudelft.idm.oclc.org/en/content/articlelanding/2017/tb/c6tb03067j.

[72] Dong-Wook Park et al. 'Electrical Neural Stimulation and Simultaneous in Vivo Monitoring with Transparent Graphene Electrode Arrays Implanted in GCaMP6f Mice'. In: *ACS Nano* 12.1 (23rd Jan. 2018). Publisher: American Chemical Society, pp. 148–157. ISSN: 1936-0851. DOI: 10.1021/acsnano.7b04321. URL: https://doi.org/10.1021/acsnano.7b04321.

[73] Yichen Lu et al. 'Ultralow Impedance Graphene Microelectrodes with High Optical Transparency for Simultaneous Deep Two-Photon Imaging in Transgenic Mice'. In: *Advanced Functional Materials* 28.31 (2018), p. 1800002. ISSN: 1616-3028. DOI: 10.1002/adfm.201800002. URL: https://onlinelibrary.wiley.com/doi/abs/10.1002/adfm.201800002.

[74] Martin Thunemann et al. 'Deep 2-photon imaging and artifact-free optogenetics through transparent graphene microelectrode arrays'. In: *Nature Communications* 9.1 (23rd May 2018). Publisher: Nature Publishing Group, p. 2035. ISSN: 2041-1723. DOI: 10.1038/s41467-018-04457-5. URL: https://www.nature.com/articles/s41467-018-04457-5.

[75] Ivan R. Minev et al. 'Electronic dura mater for long-term multimodal neural interfaces'. In: *Science* 347.6218 (9th Jan. 2015). Publisher: American Association for the Advancement of Science, pp. 159–163. DOI: 10.1126/science.1260318. URL: https://www.science.org/doi/10.1126/science.1260318.

[76] Berit Körbitzer et al. 'Electrochemical Characterization of Graphene Microelectrodes for Biological Applications'. In: *ChemNanoMat* 5.4 (2019), pp. 427–435. ISSN: 2199-692X. DOI: 10.1002/cnma.201800652. URL: https://onlinelibrary.wiley.com/doi/abs/10.1002/cnma.201800652.

[77] Pranoti Kshirsagar et al. ‘Transparent Graphene/PEDOT:PSS Microelectrodes for Electro- and Optophysiology’. In: *Advanced Materials Technologies* 4.1 (2019), p. 1800318. ISSN: 2365-709X. DOI: 10.1002/admt.201800318. URL: https://onlinelibrary.wiley.com/doi/abs/10.1002/admt.201800318.

[78] Pranoti Kshirsagar et al. ‘Graphene-based transparent microelectrode arrays for optical access to the recording site’. In: *Frontiers in Cellular Neuroscience* 12 (2018). ISSN: 1662-5102. DOI: 10.3389/conf.fncel.2018.38.00036. URL: http://www.frontiersin.org/Community/AbstractDetails.aspx?ABS_DOI=10.3389%2fconf.fncel.2018.38.00036.

[79] Berit Koerbitzer et al. ‘Graphene electrodes for stimulation of neuronal cells’. In: *2D Materials* 3.2 (Apr. 2016). Publisher: IOP Publishing, p. 024004. ISSN: 2053-1583. DOI: 10.1088/2053-1583/3/2/024004. URL: https://dx.doi.org/10.1088/2053-1583/3/2/024004.

[80] Nasim Bakhshaee et al. *Surface modification of multilayer graphene neural electrodes by local printing of platinum nanoparticles using spark ablation*. 2nd Aug. 2023. DOI: 10.1101/2023.07.30.551155.

[81] Dong-Wook Park et al. ‘Graphene-based carbon-layered electrode array technology for neural imaging and optogenetic applications’. In: *Nature Communications* 5 (20th Oct. 2014), p. 5258. ISSN: 2041-1723. DOI: 10.1038/ncomms6258. URL: https://www.ncbi.nlm.nih.gov/pmc/articles/PMC4218963/.

[82] Xin Liu et al. ‘A Compact Closed-Loop Optogenetics System Based on Artifact-Free Transparent Graphene Electrodes’. In: *Frontiers in Neuroscience* 12 (2018). ISSN: 1662-453X. URL: https://www.frontiersin.org/journals/neuroscience/articles/10.3389/fnins.2018.00132.

[83] Jeongpil Park et al. ‘Design and Fabrication of Blue LED-Integrated Graphene Electrodes for Neural Stimulation and Signal Recording’. In: *ACS Applied Electronic Materials* 3.10 (26th Oct. 2021). Publisher: American Chemical Society, pp. 4308–4316. DOI: 10.1021/acsaelm.1c00440. URL: https://doi.org/10.1021/acsaelm.1c00440.

[84] Hongming Lyu et al. ‘Graphene neural interfaces for artifact free optogenetics’. In: *2016 38th Annual International Conference of the IEEE Engineering in Medicine and Biology Society (EMBC)*. 2016 38th Annual International Conference of the IEEE Engineering in Medicine and Biology Society (EMBC). Orlando, FL: IEEE, Aug. 2016, pp. 4204–4207. ISBN: 978-1-4577-0220-4. DOI: 10.1109/EMBC.2016.7591654. URL: http://ieeexplore.ieee.org/document/7591654/.

[85] Christian Boehler et al. ‘Tutorial: guidelines for standardized performance tests for electrodes intended for neural interfaces and bioelectronics’. In: *Nature Protocols* 15.11 (Nov. 2020), pp. 3557–3578. ISSN: 1754-2189, 1750-2799. DOI: 10.1038/s41596-020-0389-2. URL: https://www.nature.com/articles/s41596-020-0389-2.

[86] Alexandros Ch. Lazanas and Mamas I. Prodromidis. ‘Electrochemical Impedance Spectroscopy — A Tutorial’. In: *ACS Measurement Science Au* 3.3 (21st June 2023). Publisher: American Chemical Society, pp. 162–193. DOI: 10.1021/acsmeasuresciau.2c00070. URL: https://doi.org/10.1021/acsmeasuresciau.2c00070.

[87] David Ding et al. ‘Evaluation of Durability of Transparent Graphene Electrodes Fabricated on Different Flexible Substrates for Chronic in vivo Experiments’. In: *IEEE transactions on biomedical engineering* 67.11 (Nov. 2020), pp. 3203–3210. ISSN: 0018-9294. DOI: 10.1109/TBME.2020.2979475. URL: https://www.ncbi.nlm.nih.gov/pmc/articles/PMC8560430/.

[88] Ryan Caldwell et al. ‘Characterization of Parylene-C degradation mechanisms: In vitro reactive accelerated aging model compared to multiyear in vivo implantation’. In: *Biomaterials* 232 (1st Feb. 2020), p. 119731. ISSN: 0142-9612. DOI: 10.1016/j.biomaterials.2019.119731. URL: https://www.sciencedirect.com/science/article/pii/S014296121930849X.

[89] Alex Suarez-Perez et al. ‘Quantification of Signal-to-Noise Ratio in Cerebral Cortex Recordings Using Flexible MEAs With Co-localized Platinum Black, Carbon Nanotubes, and Gold Electrodes’. In: *Frontiers in Neuroscience* 12 (2018). ISSN: 1662-453X. URL: https://www.frontiersin.org/journals/neuroscience/articles/10.3389/fnins.2018.00862.

[90] Ryan C. Kelly et al. ‘Comparison of Recordings from Microelectrode Arrays and Single Electrodes in the Visual Cortex’. In: *Journal of Neuroscience* 27.2 (10th Jan. 2007). Publisher: Society for Neuroscience Section: Toolbox, pp. 261–264. ISSN: 0270-6474, 1529-2401. DOI: 10.1523/JNEUROSCI.4906-06.2007. URL: https://www.jneurosci.org/content/27/2/261.

[91] Johan Agorelius et al. ‘An array of highly flexible electrodes with a tailored configuration locked by gelatin during implantation—initial evaluation in cortex cerebri of awake rats’. In: *Frontiers in Neuroscience* 9 (25th Sept. 2015). DOI: 10.3389/fnins.2015.00331.

[92] Sarnthein Johannes et al. ‘Evaluation of a new cortical strip electrode for intraoperative somatosensory monitoring during perirolandic brain surgery’. In: *Clinical Neurophysiology* 142 (1st Aug. 2022). DOI: 10.1016/j.clinph.2022.07.497.

[93] Joon Hyong Cho and Michael Cullinan. ‘Graphene Growth on and Transfer From Platinum Thin Films’. In: *Journal of Micro and Nano-Manufacturing* 6.2 (1st June 2018), p. 024501. ISSN: 2166-0468, 2166-0476. DOI: 10.1115/1.4038676. URL: https://asmedigitalcollection.asme.org/micronanomanufacturing/article/doi/10.1115/1.4038676/366762/Graphene-Growth-on-and-Transfer-From-Platinum-Thin.

[94] M. Shafiei et al. ‘Improvement of platinum adhesion to carbon surfaces using PVD coatings’. In: *Surface and Coatings Technology* 205.2 (15th Oct. 2010), pp. 306–311. ISSN: 0257-8972. DOI: 10.1016/j.surfcoat.2010.06.050. URL: https://www.sciencedirect.com/science/article/pii/S0257897210004810.

[95] Yelena Hagendoorn et al. ‘Direct Wafer-Scale CVD Graphene Growth under Platinum Thin-Films’. In: *Materials* 15.10 (Jan. 2022). Publisher: Multidisciplinary Digital Publishing Institute, p. 3723. ISSN: 1996-1944. DOI: 10.3390/ma15103723. URL: https://www.mdpi.com/1996-1944/15/10/3723.

[96] Noam Eliaz. ‘Corrosion of Metallic Biomaterials: A Review’. In: *Materials* 12.3 (28th Jan. 2019), p. 407. ISSN: 1996-1944. DOI: 10.3390/ma12030407. URL: https://www.ncbi.nlm.nih.gov/pmc/articles/PMC6384782/.

[97] Anthony H. D. Graham et al. ‘Neuronal cell biocompatibility and adhesion to modified CMOS electrodes’. In: *Biomedical Microdevices* 11.5 (21st May 2009), p. 1091. ISSN: 1572-8781. DOI: 10.1007/s10544-009-9326-4. URL: https://doi.org/10.1007/s10544-009-9326-4.

[98] Jae Park et al. ‘Functional Bioelectronic Materials for Long-Term Biocompatibility and Functionality’. In: *ACS Applied Electronic Materials* 4.4 (26th Apr. 2022). Publisher: American Chemical Society, pp. 1449–1468. DOI: 10.1021/acsaelm.1c01212. URL: https://doi.org/10.1021/acsaelm.1c01212.

[99] Kee Scholten and Ellis Meng. ‘Materials for microfabricated implantable devices: a review’. In: *Lab on a Chip* 15.22 (27th Oct. 2015). Publisher: The Royal Society of Chemistry, pp. 4256–4272. ISSN: 1473-0189. DOI: 10.1039/C5LC00809C. URL: https://pubs.rsc.org/en/content/articlelanding/2015/lc/c5lc00809c.

[100] Seung-Hee Ahn, Joonsoo Jeong and Sung June Kim. ‘Emerging Encapsulation Technologies for Long-Term Reliability of Microfabricated Implantable Devices’. In: *Micromachines* 10.8 (Aug. 2019). Publisher: Multidisciplinary Digital Publishing Institute, p. 508. ISSN: 2072-666X. DOI: 10.3390/mi10080508. URL: https://www.mdpi.com/2072-666X/10/8/508.

[101] Christina Hassler, Tim Boretius and Thomas Stieglitz. ‘Polymers for neural implants’. In: *Journal of Polymer Science Part B: Polymer Physics* 49.1 (2011), pp. 18–33. ISSN: 1099-0488. DOI: 10.1002/polb.22169. URL: https://onlinelibrary.wiley.com/doi/abs/10.1002/polb.22169.

[102] Ziyu Chen and Jeong-Bong Lee. ‘Biocompatibility of SU-8 and Its Biomedical Device Applications’. In: *Micromachines* 12.7 (July 2021). Publisher: Multidisciplinary Digital Publishing Institute, p. 794. ISSN: 2072-666X. DOI: 10.3390/mi12070794. URL: https://www.mdpi.com/2072-666X/12/7/794.

[103] Sung-Hoon Cho et al. ‘Biocompatible SU-8-Based Microprobes for Recording Neural Spike Signals From Regenerated Peripheral Nerve Fibers’. In: *IEEE Sensors Journal* 8.11 (Nov. 2008). Conference Name: IEEE Sensors Journal, pp. 1830–1836. ISSN: 1558-1748. DOI: 10.1109/JSEN.2008.2006261.

[104] Krishnamurthy V. Nemani et al. ‘In vitro and in vivo evaluation of SU-8 biocompatibility’. In: *Materials Science and Engineering: C* 33.7 (1st Oct. 2013), pp. 4453–4459. ISSN: 0928-4931. DOI: 10.1016/j.msec.2013.07.001. URL: https://www.sciencedirect.com/science/article/pii/S0928493113004049.

[105] Gergely Márton et al. ‘The neural tissue around SU-8 implants: A quantitative in vivo biocompatibility study’. In: *Materials Science and Engineering: C* 112 (1st July 2020), p. 110870. ISSN: 0928-4931. DOI: 10.1016/j.msec.2020.110870. URL: https://www.sciencedirect.com/science/article/pii/S0928493119346661.

[106] Dong Sup Lee et al. ‘Comparison of in vivo biocompatibilities between parylene-C and polydimethylsiloxane for implantable microelectronic devices’. In: *Bulletin of Materials Science* 36.6 (Nov. 2013), pp. 1127–1132. ISSN: 0250-4707, 0973-7669. DOI: 10.1007/s12034-013-0570-0. URL: http://link.springer.com/10.1007/s12034-013-0570-0.

[107] Jui-Mei Hsu et al. ‘Encapsulation of an Integrated Neural Interface Device With Parylene C’. In: *IEEE Transactions on Biomedical Engineering* 56.1 (Jan. 2009). Conference Name: IEEE Transactions on Biomedical Engineering, pp. 23–29. ISSN: 1558-2531. DOI: 10.1109/TBME.2008.2002155.

[108] Su-Jin Kim et al. ‘Evaluation of the biocompatibility of a coating material for an implantable bladder volume sensor’. In: *The Kaohsiung Journal of Medical Sciences* 28.3 (1st Mar. 2012), pp. 123–129. ISSN: 1607-551X. DOI: 10.1016/j.kjms.2011.10.016. URL: https://www.sciencedirect.com/science/article/pii/S1607551X11002397.

[109] Tracy Y. Chang et al. ‘Cell and Protein Compatibility of Parylene-C Surfaces’. In: *Langmuir* 23.23 (1st Nov. 2007), pp. 11718–11725. ISSN: 0743-7463, 1520-5827. DOI: 10.1021/la7017049. URL: https://pubs.acs.org/doi/10.1021/la7017049.

[110] Brian J. Kim and Ellis Meng. ‘Micromachining of Parylene C for bioMEMS’. In: *Polymers for Advanced Technologies* 27.5 (2016), pp. 564–576. ISSN: 1099-1581. DOI: 10.1002/pat.3729. URL: https://onlinelibrary.wiley.com/doi/abs/10.1002/pat.3729.

[111] Breanne P Christie et al. ‘Approaches to a cortical vision prosthesis: implications of electrode size and placement’. In: *Journal of Neural Engineering* 13.2 (1st Apr. 2016), p. 025003. ISSN: 1741-2560, 1741-2552. DOI: 10.1088/1741-2560/13/2/025003. URL: https://iopscience.iop.org/article/10.1088/1741-2560/13/2/025003.

[112] Abhishek Prasad et al. ‘Abiotic-biotic characterization of Pt/Ir microelectrode arrays in chronic implants’. In: *Frontiers in Neuroengineering* 7 (2014). ISSN: 1662-6443. URL: https://www.frontiersin.org/articles/10.3389/fneng.2014.00002.

[113] E. M. Schmidt, J. S. Mcintosh and M. J. Bak. ‘Long-term implants of Parylene-C coated microelectrodes’. In: *Medical & Biological Engineering & Computing* 26.1 (Jan. 1988), pp. 96–101. ISSN: 0140-0118, 1741-0444. DOI: 10.1007/BF02441836. URL: http://link.springer.com/10.1007/BF02441836.

[114] Jui-Mei Hsu et al. ‘Characterization of Parylene-C film as an encapsulation material for neural interface devices’. In: (6th Dec. 2022).

[115] Micha E. Spira and Aviad Hai. ‘Multi-electrode array technologies for neuroscience and cardiology’. In: *Nature Nanotechnology* 8.2 (Feb. 2013). Publisher: Nature Publishing Group, pp. 83–94. ISSN: 1748-3395. DOI: 10.1038/nnano.2012.265. URL: https://www.nature.com/articles/nnano.2012.265.

[116] Guenter W. Gross, Walter Y. Wen and Jacob W. Lin. ‘Transparent indium-tin oxide electrode patterns for extracellular, multisite recording in neuronal cultures’. In: *Journal of Neuroscience Methods* 15.3 (1st Nov. 1985), pp. 243–252. ISSN: 0165-0270. DOI: 10.1016/0165-0270(85)90105-0. URL: https://www.sciencedirect.com/science/article/pii/0165027085901050.

[117] Guenter W. Gross. ‘Simultaneous Single Unit Recording in vitro with a Photoetched Laser Deinsulated Gold Multimicroelectrode Surface’. In: *IEEE Transactions on Biomedical Engineering* BME-26.5 (May 1979). Conference Name: IEEE Transactions on Biomedical Engineering, pp. 273–279. ISSN: 1558-2531. DOI: 10.1109/TBME.1979.326402.

[118] S. K. Gollapudi, J. J. Michael and M. Chandra. 'Striated Muscle Dynamics'. In: *Reference Module in Biomedical Sciences*. Elsevier, 1st Jan. 2014. ISBN: 978-0-12-801238-3. DOI: 10.1016/B978-0-12-801238-3.00251-8. URL: https://www.sciencedirect.com/science/article/pii/B9780128012383002518.

[119] Sebastian Kreß et al. '3D Printing of Cell Culture Devices: Assessment and Prevention of the Cytotoxicity of Photopolymers for Stereolithography'. In: *Materials* 13.13 (Jan. 2020). Publisher: Multidisciplinary Digital Publishing Institute, p. 3011. ISSN: 1996-1944. DOI: 10.3390/ma13133011. URL: https://www.mdpi.com/1996-1944/13/13/3011.

[120] Johann Wulff, Helmut Schweikl and Martin Rosentritt. 'Cytotoxicity of printed resin-based splint materials'. In: *Journal of Dentistry* 120 (1st May 2022), p. 104097. ISSN: 0300-5712. DOI: 10.1016/j.jdent.2022.104097. URL: https://www.sciencedirect.com/science/article/pii/S0300571222001543.

[121] Niels Harlaar et al. 'Conditional immortalization of human atrial myocytes for the generation of in vitro models of atrial fibrillation'. In: *Nature Biomedical Engineering* 6.4 (Apr. 2022). Publisher: Nature Publishing Group, pp. 389–402. ISSN: 2157-846X. DOI: 10.1038/s41551-021-00827-5. URL: https://www.nature.com/articles/s41551-021-00827-5.

[122] B.A. Avelar-Freitas et al. 'Trypan blue exclusion assay by flow cytometry'. In: *Brazilian Journal of Medical and Biological Research* 47.4 (18th Mar. 2014), pp. 307–3015. ISSN: 0100-879X. DOI: 10.1590/1414-431X20143437. URL: https://www.ncbi.nlm.nih.gov/pmc/articles/PMC4075294/.

[123] Judith R. Tennant. 'EVALUATION OF THE TRYPAN BLUE TECHNIQUE FOR DETERMINATION OF CELL VIABILITY'. In: *Transplantation* 2.6 (Nov. 1964), p. 685. ISSN: 0041-1337. URL: https://journals.lww.com/transplantjournal/Abstract/1964/11000/EVALUATION_OF_THE_TRYPAN_BLUE_TECHNIQUE_FOR.1.aspx.

[124] Marcelo Larramendy and Sonia Soloneski. *Genotoxicity: A Predictable Risk to Our Actual World*. BoD – Books on Demand, 11th July 2018. 124 pp. ISBN: 978-1-78923-418-3.

[125] K H Jones and J A Senft. 'An improved method to determine cell viability by simultaneous staining with fluorescein diacetate-propidium iodide.' In: *Journal of Histochemistry & Cytochemistry* 33.1 (1st Jan. 1985). Publisher: Journal of Histochemistry & Cytochemistry, pp. 77–79. ISSN: 0022-1554. DOI: 10.1177/33.1.2578146. URL: https://doi.org/10.1177/33.1.2578146.

[126] Sara Martínez Dopico. 'Estudio del efecto citotóxico ejercido por el diclofenaco sobre las microalgas Chlamydomonas reinhardtii y Phaeodactylum tricornutum'. PhD thesis. UNIVERSIDAD DE A CORUÑA, Feb. 2018.

[127] Tomas M. Díaz et al. 'FDA/PI flow cytometry assay of complement-mediated cytotoxicity of antibodies generated during xenotransplantation'. In: *Cytometry Part A* 62A.1 (2004), pp. 54–60. ISSN: 1552-4930. DOI: 10.1002/cyto.a.20076. URL: https://onlinelibrary.wiley.com/doi/abs/10.1002/cyto.a.20076.

[128] H. L. Bank. 'Assessment of islet cell viability using fluorescent dyes'. In: *Diabetologia* 30.10 (1st Oct. 1987), pp. 812–816. ISSN: 1432-0428. DOI: 10.1007/BF00275748. URL: https://doi.org/10.1007/BF00275748.

[129] Julián Iglesias Rodrígez. 'Estudio funcional de los dominios del receptor apoptótico DR6. Señalización y procesamiento.' PhD thesis. Universidad de Oviedo, July 2016.

[130] Jean-Pierre Aubry et al. 'Annexin V used for measuring apoptosis in the early events of cellular cytotoxicity'. In: *Cytometry* 37.3 (1999), pp. 197–204. ISSN: 1097-0320. DOI: 10.1002/(SICI)1097-0320(19991101)37:3<197::AID-CYTO6>3.0.CO;2-L. URL: https://onlinelibrary.wiley.com/doi/abs/10.1002/%28SICI%291097-0320%2819991101%2937%3A3%3C197%3A%3AAID-CYTO6%3E3.0.CO%3B2-L.

[131] Yi Shounan, Ximin Feng and Philip J. O'Connell. 'Apoptosis detection by annexin V binding: a novel method for the quantitation of cell-mediated cytotoxicity'. In: *Journal of Immunological Methods* 217.1 (1st Aug. 1998), pp. 61–70. ISSN: 0022-1759. DOI: 10.1016/S0022-1759(98)00090-8. URL: https://www.sciencedirect.com/science/article/pii/S0022175998000908.

[132] S. Vollebregt et al. 'Influence of the growth temperature on the first and second-order Raman band ratios and widths of carbon nanotubes and fibers'. In: *Carbon* 50.10 (1st Aug. 2012), pp. 3542–3554. ISSN: 0008-6223. DOI: 10.1016/j.carbon.2012.03.026. URL: https://www.sciencedirect.com/science/article/pii/S0008622312002746.

[133] Samantha June Rice. 'Graphene with Platinum Nanoparticles for Neural Recording and Stimulation'. Delft University of Technology, Jan. 2023. 103 pp.

[134] Sabine Weiskirchen et al. 'A Beginner's Guide to Cell Culture: Practical Advice for Preventing Needless Problems'. In: *Cells* 12.5 (21st Feb. 2023), p. 682. ISSN: 2073-4409. DOI: 10.3390/cells12050682. URL: https://www.ncbi.nlm.nih.gov/pmc/articles/PMC10000895/.

[135] Bo Tang, Hu Guoxin and Hanyang Gao. 'Raman Spectroscopic Characterization of Graphene'. In: *Applied Spectroscopy Reviews* 45.5 (17th Sept. 2010). Publisher: Taylor & Francis, pp. 369–407. ISSN: 0570-4928. DOI: 10.1080/05704928.2010.483886. URL: https://doi.org/10.1080/05704928.2010.483886.

[136] A. C. Ferrari et al. 'Raman Spectrum of Graphene and Graphene Layers'. In: *Physical Review Letters* 97.18 (30th Oct. 2006). Publisher: American Physical Society, p. 187401. DOI: 10.1103/PhysRevLett.97.187401. URL: https://link.aps.org/doi/10.1103/PhysRevLett.97.187401.

[137] Joseph A. Garlow et al. 'Large-Area Growth of Turbostratic Graphene on Ni(111) via Physical Vapor Deposition'. In: *Scientific Reports* 6.1 (29th Jan. 2016). Publisher: Nature Publishing Group, p. 19804. ISSN: 2045-2322. DOI: 10.1038/srep19804. URL: https://www.nature.com/articles/srep19804.

[138] Guangyong Zhu et al. 'Raman spectra of amino acids and their aqueous solutions'. In: *Spectrochimica Acta Part A: Molecular and Biomolecular Spectroscopy* 78.3 (1st Mar. 2011), pp. 1187–1195. ISSN: 1386-1425. DOI: 10.1016/j.saa.2010.12.079. URL: https://www.sciencedirect.com/science/article/pii/S1386142510007043.

[139] Tatyana Teslova et al. 'Raman and surface-enhanced Raman spectra of flavone and several hydroxy derivatives'. In: *Journal of Raman Spectroscopy* 38.7 (2007), pp. 802–818. ISSN: 1097-4555. DOI: 10.1002/jrs.1695. URL: https://onlinelibrary.wiley.com/doi/abs/10.1002/jrs.1695.

[140] Matthew W. Smith et al. 'Structural analysis of char by Raman spectroscopy: Improving band assignments through computational calculations from first principles'. In: *Carbon* 100 (1st Apr. 2016), pp. 678–692. ISSN: 0008-6223. DOI: 10.1016/j.carbon.2016.01.031. URL: https://www.sciencedirect.com/science/article/pii/S0008622316300318.

[141] M. A. Strehle et al. 'A Raman spectroscopic study of the adsorption of fibronectin and fibrinogen on titanium dioxide nanoparticles'. In: *Physical Chemistry Chemical Physics* 6.22 (2004). Publisher: Royal Society of Chemistry, pp. 5232–5236. DOI: 10.1039/B406524G. URL: https://pubs-rsc-org.tudelft.idm.oclc.org/en/content/articlelanding/2004/cp/b406524g.

[142] Christian Redlich et al. 'Molybdenum – A biodegradable implant material for structural applications?' In: *Acta Biomaterialia* 104 (1st Mar. 2020), pp. 241–251. ISSN: 1742-7061. DOI: 10.1016/j.actbio.2019.12.031. URL: https://www.sciencedirect.com/science/article/pii/S1742706119308694.

[143] Christian Redlich et al. 'In Vitro Degradation Behavior and Biocompatibility of Bioresorbable Molybdenum'. In: *Metals* 11.5 (May 2021). Publisher: Multidisciplinary Digital Publishing Institute, p. 761. ISSN: 2075-4701. DOI: 10.3390/met11050761. URL: https://www.mdpi.com/2075-4701/11/5/761.

[144] Philip C. H. Mitchell et al. 'Molybdenum and Molybdenum Compounds'. In: *Ullmann's Encyclopedia of Industrial Chemistry*. John Wiley & Sons, Ltd, 2020, pp. 1–63. ISBN: 978-3-527-30673-2. DOI: 10.1002/14356007.a16_655.pub2. URL: https://onlinelibrary.wiley.com/doi/abs/10.1002/14356007.a16_655.pub2.

[145] Franz Selbmann et al. 'Impact of Non-Accelerated Aging on the Properties of Parylene C'. In: *Polymers* 14.23 (Jan. 2022). Publisher: Multidisciplinary Digital Publishing Institute, p. 5246. ISSN: 2073-4360. DOI: 10.3390/polym14235246. URL: https://www.mdpi.com/2073-4360/14/23/5246.

[146] Irfan et al. ‘Energy level evolution of air and oxygen exposed molybdenum trioxide films’. In: *Applied Physics Letters* 96.24 (16th June 2010), p. 243307. ISSN: 0003-6951. DOI: 10.1063/1.3454779. URL: https://doi.org/10.1063/1.3454779.

[147] Fujun Zhang et al. ‘Effect of an Ultra-thin Molybdenum Trioxide Layer and Illumination Intensity on the Performance of Organic Photovoltaic Devices’. In: *Energy & Fuels* 24.7 (15th July 2010). Publisher: American Chemical Society, pp. 3739–3742. ISSN: 0887-0624. DOI: 10.1021/ef901325e. URL: https://doi.org/10.1021/ef901325e.

[148] Jessica Ortigoza-Diaz et al. ‘Techniques and Considerations in the Microfabrication of Parylene C Microelectromechanical Systems’. In: *Micromachines* 9.9 (22nd Aug. 2018), p. 422. ISSN: 2072-666X. DOI: 10.3390/mi9090422. URL: https://www.ncbi.nlm.nih.gov/pmc/articles/PMC6187609/.

[149] Serhiy Cherevko et al. ‘Gold dissolution: towards understanding of noble metal corrosion’. In: *RSC Advances* 3.37 (28th Aug. 2013). Publisher: The Royal Society of Chemistry, pp. 16516–16527. ISSN: 2046-2069. DOI: 10.1039/C3RA42684J. URL: https://pubs.rsc.org/en/content/articlelanding/2013/ra/c3ra42684j.

[150] Stefan J. Raaijman, Nakkiran Arulmozhi and Marc T. M. Koper. ‘Anisotropic Cathodic Corrosion of Gold Electrodes in the Absence and Presence of Carbon Monoxide’. In: *The Journal of Physical Chemistry C* 124.52 (31st Dec. 2020). Publisher: American Chemical Society, pp. 28539–28554. ISSN: 1932-7447. DOI: 10.1021/acs.jpcc.0c08574. URL: https://doi.org/10.1021/acs.jpcc.0c08574.

A

Microfabrication Flowchart

Graphene microelectrode array on quartz substrate

Flow chart

Version
25 July 2023
Gonzalo León González

Process engineer: Gonzalo León González
Mentor: Sten Vollebregt
Start: October 2022
Contamination: Yes
Labs: CR100, CR10000, MEMS, Polymer, Biosonics

EKL(Else Kooi Laboratory)
DELFT UNIVERSITY OF TECHNOLOGY

Address	Feldmannweg 17, 2628 CT Delft, The
P.O. Box	5053, 2600 GB Delft, The Netherlands
Phone :	+31 - (0)15 - 2783868
Fax :	+31 - (0)15 - 2622163
Website	http://ekl.tudelft.nl/EKL/Home.php

Detailed information about possible contamination:

Place/Clean Rooms used in the process:

- Write the sequence of used labs from start to finish.
- Which (Non-standard) materials or process steps
- Process step number
- What kind of process or machine was used?
- The other materials or wafers that contain non-green metals that are also processed in this machine

Lab/ Clean Room	Non-standard materials	Process step	Machine-process	Other materials used in machine
CR100	none	none	none	none
CR10000	Yes, graphene	20	BlackMagic	Cu, Pt, Ni
MEMS	none	none	none	none
Polymer	none	none	none	none
Biosonics	none	none	none	none

If other labs are used:
Write the steps number: Possible contamination issues/materials.
None

If there are custom steps in a standard process or possible cross contamination materials are used: Write down the

- **Step number**
- **Material**
- **Machine/tool where the process is done**
- **Pre and past process step numbers that are used to prevent cross contamination.**

Step number	Material	Machine/Tool/lab	Process steps to prevent cross contamination
13	Cu	Trikon Sigma	Use the cassette for contaminated wafers. Use transport wafers for red metals for each of the test wafers. Use non-contaminated tweezers for the transport wafers and contaminated tweezers for the test wafers.

STARTING MATERIAL

Use **15 double side polished 4" fused silica (SiO2) wafer**, with the following specifications:

Type:	NA
Orientation:	NA
Resistivity:	NA
Thickness:	500 μm
Diameter:	100.0 mm

Wafers taken out of an already opened box must be cleaned before processing, according to the standard procedure.
Wafers taken out of an unopened wafer box do not have to be cleaned before processing**.**

Part 1: Cleaning step

1. Cleaning Procedure: HNO3 99% and 69.5% @100

Wafers taken out of an unopened wafer box do not have to be cleaned before processing.
Cleaning:
10 minutes in fuming nitric acid (Merck: HNO3 99%) at ambient temperature. Use wet bench "HNO3 (99%)" and the carrier with the white dot.
QDR:
Rinse in the Quick Dump Rinser with the standard program until the resistivity is 5 MΩ.
Cleaning:
10 minutes in concentrated nitric acid (Merck: HNO3 69.5%) at 110 °C. Use wet bench "HNO3 (69.5%)" and the carrier with the white dot.
QDR:
Rinse in the Quick Dump Rinser with the standard program until the resistivity is 5 MΩ. Drying:
Use the Semitool "rinser/dryer" with the standard program, and the white carrier with a red dot.

Part 2: Mo deposition

2. Wafer Numbering @100

Use a diamond tip scriber to indent the quartz wafers at the front side at the bottom end.
This helps identify each wafer and prevent miss-positioning of the wafer.

Perform a cleaning step afterwards to remove the particles created with the scriber.
Rinse with the DI water hose and spin dry.

3. Catalyst Deposition @100

Use the **TRIKON SIGMA** sputter coater for the deposition of the catalyst metal Mo layer on the process wafers.
Follow the operating instructions from the manual when using this machine.

In order to coat transparent wafers, the sensors must be off!
Alternatively use carrier wafers, however this carries issues of the wafer moving above the carrier wafer.

If necessary, perform a target clean with recipe **'_TrgtCln_Mo_50C'**. This step will require the use of a dummy wafer.

Mo: 50 nm, recipe '**Mo_50nm_50C**'

Visual inspection: the metal layer must look shiny.

4. Backside layer deposition @100

Use the **TRIKON SIGMA** sputter coater for the deposition of a 50nm Ti layer on the backside of the process wafers.
Follow the operating instructions from the manual when using this machine.

In order to coat transparent wafers, the sensors must be off! The Mo layer may be too thin or not cover the edges leading to errors.
Alternatively use carrier wafers, however this carries issues of the wafer moving above the carrier wafer.

If necessary, perform a target clean with recipe **'_Trgt_Cln_Ti_50C'.** This step will require the use of a dummy wafer.

Ti: 50 nm, recipe '**Ti_50nm_50C**'

Visual inspection: the metal layer must look shiny.

5. Coating and Baking @100

Use the **EVG 120** wafertrack to coat the wafers with resist, and follow the instructions specified for this equipment.
The process consists of a treatment with HMDS (hexamethyldisilazane) vapor with nitrogen as a carrier gas, spin coating with Shipley SPR3012 positive photoresist, and a soft bake at 95degC for 90 seconds.
Always check the temperature of the hotplate and the relative humidity (48 ± 2 %) in the room first.

Use coating recipe **'SpeCo – 3012 – 1.4 µm-glass-noEBR-SB2'15"'**

6. Alignment and Exposure @100

Processing will be performed on the **SUSS MicroTec MA/BA8** mask aligner.

Follow the operating instructions from the manual when using this machine.

Use **G-MEA-2023 mask**, **layer GRAPHENE**,
Use recipe: **'1_FSA_Soft_Contact'**
Calculate the exposure time by consulting the mask aligner exposure energy data log.
Assume Mo is opaque, so 140mJ/cm^2 for all wafers (add 15% more time to compensate for not being able to do hard contact).

7. Development @100

Use the **EVG 120** wafertrack to develop the wafers and follow the instructions specified for this equipment.
The process consists of a post-exposure bake at 115**°C** for 90 seconds, followed by a development step using Shipley MF322 developer (single puddle process), and a hard bake at 100**°C** for 90 seconds.
Always check the temperature of the hotplates first.

Use development program '**Dev – SP**'

8. Inspection: Linewidth @100

Visually inspect the wafers through a microscope and check the linewidth. No resist residues are allowed.

If resist remains are found attempt rinsing the wafers with a DI water gun and spin drying them. If it persists review your exposure settings as they might be off.

In case of misalignment or defects in the photoresist pattern remove the photoresist layer as described in step **10**, and then continue from step **5**.

9. Plasma Etching of Molybdenum @100

Use the **Trikon Ωmega 201** plasma etcher.
Follow the operating instructions from the manual when using this machine.
The process conditions of the etch program may not be changed!

Use sequence '**Mo_test5**' and set the platen temperature to **16 °C**. Check the time is set for 50 nm (~30 sec).

10. Cleaning Procedure: Spray Coater @100

Acetone photoresist cleaning programme.
Use the non-contaminated wafer carrier.
During the first 10 seconds spray acetone, followed by another 10 seconds of IPA. Allow the last 10 seconds to dry the wafer.

Visual inspection: the frontside metal layer must look shiny (only the alignment markers will be visible).

In case the Spray Coater is not available, photoresist may also be removed in the Etching line. Place the wafers in the 40ºC Acetone bath for 5min and then perform a Rinser Drier programe in the rinser (green metals).

11. Ti layer etching: @100 - Etching line

Perform a wet etching step using HF 0.55%. Etch until you can no longer see metal + 30 secs overetch. It should take around **1min** for the 50nm layer of Ti.

Rinse in the **rinser** and finish with the **Rinser Drier program**.

Part 3: Graphene Growth

12. Graphene growth @ 10000

Use the **AIXTRON BlackMagic Pro** to grow graphene using CVD
Use recipe: **'Mo_NEW_915C_20minCH4'**

Use graphene reactor interior (Cu contaminated)!

USE RED BOX, OR WHITE BLISTER WITH CU WIRTTEN ON IT

The process wafers are now considered Cu contaminated on the front and back sides. Beware of which tweezers to use when handling the wafers. Put the wafers in a process box dedicated for Cu contaminated processes.

Part 4: Electrode Metal Deposition and Patterning

13. Metal Deposition @100

Use the cassette for contaminated wafers. Use carrier wafers for red metals for each of the test wafers. Use non-contaminated tweezers for the carrier wafers and contaminated tweezers for the test wafers.

Use the **TRIKON SIGMA** Sputter coater for the deposition of metal interface Ti+pAl layer on the wafers.
If necessary, perform a target clean with recipes '**_Trgt_Cln_Ti_50C**' and '**_TrgtCln_pAl50_DepC'**. This step will require the use of two dummy wafers.

Use recipe '**Ti_50nm_Al_100nm_50C**' for titanium and aluminium

Visual inspection: the metal layer must look shiny.

14. Coating and Baking @Polymer lab

Prepare the brewer **manual spinner** with aluminum foil
Keep gloves clean when using the screen. Use chuck for contaminated wafers!

HMDS treatment	Treat wafers with HMDS (hexamethyldisilazane) vapor with nitrogen as a carrier gas for **10 mins**. Use cassette for contaminated wafers.
Photoresist coating	Use photoresist AZ3027. Do a test run with a dummy wafer without photoresist before starting.
Soft Bake	Soft bake the wafer on a hot plate for contaminated wafers at **95 deg. C for 2 mins**. Use carrier wafers for contaminated wafers

Use coating **'AZ_ECI_3027_3100nm'** (resist thickness: 3.10µm).

15. Alignment and Exposure @100

Use the **SUSS MicroTec MA/BA8** mask aligner to expose the photoresist.
Use **mask** for device **G-MEA-2023**, layer **METAL ELECTRODES**. Use the contaminated chuck for this step.

Use recipe **'1_FSA_Soft_Contact'**
Calculate the exposure time by consulting the contact aligner exposure energy data log [**420mJ/cm^2**] (don't add 15% of extra time).

16. Manual Development @Polymer lab

Post-exposure baking	Bake at 115 deg. C for **2 mins.** Use the hot plate for contaminated wafers.
Photoresist development	Use Shipley MF322 developer for **40 seconds**. Make sure to rinse immediately to stop the development from delaminating the metal layer.
Dry	Spin dry the wafer spin. Use the contaminated chuck for the spin dryer.
Inspection	Visually inspect the wafers through a microscope and check the openings. If major defects are found remove the photoresist layer as described in step **18**, and then continue from step **14**.
Hard baking	Bake **100 deg. C for 2 min.** Use the hot plate for contaminated wafers.
Inspection	Visually inspect the wafers through a microscope and check openings. If major defects are found remove the photoresist layer as described in step **18**, and then continue from step **14**.

17. Etching of Ti+pAl @Wet bench 10000

Make your own 0.55% HF bath in the wetbench of the CR10000.
Perform a wet etching step using HF 0.55% for about **2min**. (Etch until you can no longer see metal + 30 secs overetch)
Rinse in DI water for **5min**.

18. Photoresist removal @Polymer Lab

Carefully coat the dies in acetone for **3 min**.
Then rinse **3 min** with IPA and **3 min** with DI water.
Allow the dies to air dry.

Part 5: Contact Pads Metal Deposition and Patterning

19. Backside Metal Deposition @10000

Use the **CHA Solutions Std**. for the deposition of the Ti backside metal layer on the wafers.

Make sure to allow the machine to reach vacuum overnight to ensure a better-quality metal layer.

Deposit **200nm** of **Ti** on the **backside**.

Be aware – Ti deposition takes very long and has very irregular deposition rates.

Due to the duration of the deposition, in order to avoid overbaking the photoresist, if the temperature gets to 75ºC, stop the recipe, wait 20 mins and resume it.

Visual inspection: the metal layer must look shiny.

20. Coating and Baking @Polymer lab

Prepare the brewer manual spinner with aluminum foil
Keep gloves clean when using the screen. Use chuck for contaminated wafers!

HMDS treatment	Treat wafers with HMDS (hexamethyldisilazane) vapor with nitrogen as a carrier gas for **10 mins**. Use cassette for contaminated wafers.
Photoresist coating	Use **NEGATIVE** photoresist **NLOF-2020**. Do a test run with a dummy wafer without photoresist before starting.
Soft Bake	Soft bake the wafer on a hot plate for contaminated wafers at **95 deg. C for 3 min.** Use carrier wafers for contaminated wafers

Use coating **'AZ-Nlof-3500nm'** (resist thickness: 3.50µm)

Be aware – Negative photoresists are difficult to remove. To reduce number of residues left, remove photoresist before development by following step 24, and start again with step 20. THERE WILL ALWAYS BE RESIDUES FROM NEGATIVE PHOTORESIST REMOVAL.

21. Alignment and Exposure @100

Use the **SUSS MicroTec MA/BA8** mask aligner to expose the photoresist.
Use **mask** for device **G-MEA-2023**, layer **METAL PADS**. Use the contaminated chuck for this step.

Use recipe **'1_FSA_Soft_Contact'**
Calculate the exposure time by consulting the contact aligner exposure energy data log. Use **80mJ/cm2**.

22. Manual Development @Polymer lab

X-Link bake	Bake at 115 deg. C for **3 min**.
Photoresist development	Use **MF322** developer for **1 min** twice. You can also develop for 2 mins straight. Overdeveloping is not a major problem in negative photoresist.
Dry	Air dry the wafer. Use the contaminated chuck for the spin dryer.
Inspection	Visually inspect the wafers through a microscope and check the openings. If major defects are found remove the photoresist layer as described in step **24**, and then continue from step **20**.
Hard baking	Bake **100 deg. C for 4 min.** Use the hot plate for contaminated wafers.
Inspection	Visually inspect the wafers through a microscope and check openings. If major defects are found remove the photoresist layer as described in step **24**, and then continue from step **20**.

23. Metal Deposition @10000

Use the CHA Solution Std. for Ti/Au evaporator to deposit **10 nm** of **Ti** and **200 nm** of **Au**. **Make sure the Au dome and shutters have been installed**, if not ask a trained senior user to do change them.
Ensure the vacuum is not lost between layer depositions.

Allow the machine to reach vacuum overnight to ensure a better-quality metal layer.

Due to the thickness of the gold layer, in order to avoid overbaking the photoresist, if the temperature gets to 75ºC, stop the recipe, wait 20 mins and resume it.

Visual inspection: the metal layer must look shiny.

24. Liftoff @10000 - Wetbench

Fill a beaker with **NI555**.
Use a metallic scriber to **scratch the gold** on areas where there are no structures. This will increase the surface of the exposed photoresist to the **NI555** accelerating the process.
Place the wafers in a holder and submerge it in the beaker with **NI555**.

Leave the wafers in **NI555** overnight.

Rinse in DI water and allow to air dry.

Be aware – **NI555** can be reused multiple times, however, etch rate will drop drastically when saturated with photoresist. Good photoresist removal is necessary! Ensure etch rate of **NI555** does not go too low and replace when necessary.

Part 6: Parylene Encapsulation

25. Parylene C Deposition @MEMS lab

Deposit 1 µm of Parylene C in MEMS lab using the **LABCOATER 2 (PDS 2010)**. For this purpose, use 2 g of dimer. Follow the instruction for Parylene C deposition.

Place the wafters on a glass slide with the front side facing up to protect the backside from Parylene C deposition.

Check the layer thickness by using an additional quartz dummy wafer. This will serve to check if the amount of dimmer is correct for a 1µm layer, to measure the approximate layer thickness for the lot of wafers on which Paryelene C was deposited (differences will be found between depositions), and to measure the etch rate at a later step.

To measure the layer thickness:

- Remove a section of the Parylene C layer from the edge of the wafer using a sharp knife (DO NOT cut the substrate). Then measure the height difference using the **Dektak 8 Surface Profilometer**.
- Alternatively, you can also create a model using the refractive index of Parylene C and use the **reflectometer**.

Do not forget to use the contaminated carrier and carrier wafers!

Part 7: Parylene Etching

26. Coating and baking @Polymer Lab

Prepare the brewer manual spinner with aluminum foil
Keep gloves clean when using the screen. Use chuck for contaminated wafers!

HMDS treatment	Treat wafers with HMDS (hexamethyldisilazane) vapor with nitrogen as a carrier gas for **10 mins**. Use cassette for contaminated wafers.
Photoresist coating	Use photoresist AZ3027 Do a test run with a dummy wafer without photoresist before starting.
Soft Bake	Soft bake the wafer on a hot plate for contaminated wafers at **80 deg. C for 8 min.** The glass transition temperature of Parylene C is around 90ºC. DO NOT USE HIGHER TEMPERATURE THAN INDICATED. Use carrier wafers for contaminated wafers.

Use coating **'AZ_ECI-3027-4000nm'** (resist thickness: 4µm).

Coat the extra dummy wafer coated with Parylene C to calculate the etching rate at a later step.

27. Alignment and Exposure @100

Use the **SUSS MicroTec MA/BA8** mask aligner to expose the photoresist.
Use **mask** for device **G-MEA-2023**, layer **OPENINGS**. Use the contaminated chuck for this step.

Use recipe **'1_FSA_Soft_Contact'**
Calculate the exposure time by consulting the contact aligner exposure energy data log. Use **400mJ/cm2** and no extra time.

28. Development @Polymer Lab

Post-exposure baking	Bake at **80 deg. C for 128 min** in the **Memmert Oven**
Photoresist development	Use Shipley MF322 developer for 50 sec. Make sure not to overdevelop.
Dry	Spin dry the wafer. Use the contaminated chuck for the spin dryer.
Inspection	Visually inspect the wafers through a microscope and check the openings. If major defects are found remove the photoresist layer as described in step **30**, and then continue from step **26**.
Hard baking	Bake at **80 deg. C for 16 min**. Use the **Memmert Oven**.
Inspection	Visually inspect the wafers through a microscope and check the openings. If major defects are found remove the photoresist layer as described in step **30**, and then continue from step **26**.

29. Etching of Parylene @100

Use the **AMS110** plasma etcher to etch Parylene C
Use the **Par_etch** recipe.

Use the silicon dummy wafer first to calculate the etching rate, etching for one minute at a time.
Even so, the time might not be the same for all wafers.

A change in colour is observed when the metal layer is reached, which can be used as an indicator of when the etch is complete.

Etch time will be slightly different for every wafer, based on how much Parylene C was deposited. Aim at 2min etch-time but be aware that this might over-etch some wafers and under-etch some others. Over-etched wafers are useless as the Graphene electrode is cut by the plasma. For under-etched wafers try adding etching steps as small as 10-15s.

30. Cleaning Procedure: Spray Coater

Acetone photoresist cleaning programme.
Use the non-contaminated wafer carrier.
During the first 10 seconds spray acetone, followed by another 10 seconds of IPA. Allow the last 10 seconds to dry the wafer.
Due to the plasma, there will be photoresist residues after acetone. Use a cotton bud soaked in IPA to carefully swipe the wafer in order to remove the photoresist residues. Be careful not to scratch the Parylene C. Perform circular motions around the electrode openings and back and forward movements along the contact pad openings and dicing tracks.

If the Spray Coater is not available, you might be able to remove the photoresist by submerging the wafers in acetone for 3min, then in IPA for 3min, and rinse in DI water for another 3min. (@Polymer Lab)
Then spin dry the wafers (using the contaminated chuck).

Another alternative if photoresist residues are very present is to dip the wafers in NI555 overnight. (@Wetbench 10000)

Part 8: Wafer Dicing

31. Coating and baking @Polymer Lab

Prepare the brewer manual spinner with aluminum foil
Keep gloves clean when using the screen. Use chuck for contaminated wafers!

HMDS treatment	Treat wafers with HMDS (hexamethyldisilazane) vapor with nitrogen as a carrier gas for **10 mins**. Use cassette for contaminated wafers.
Photoresist coating	Use photoresist AZ3027 Do a test run with a dummy wafer without photoresist before starting.
Soft Bake	Soft bake the wafer on a hot plate for contaminated wafers at **80 deg. C for 8 min**. The glass transition temperature of Parylene C is around 90ºC. DO NOT USE HIGHER TEMPERATURE THAN INDICATED. Use carrier wafers for contaminated wafers

Use coating **'AZ_ECI-3027-4000nm'** (resist thickness: 4µm).

32. Development @Polymer Lab

There will be no exposure step as the intent is to protect the whole surface from the dicing procedure.

Post-exposure baking	Bake at **80 deg. C for 128 min** in the **Memmert Oven**.
Photoresist development	Use Shipley MF322 developer for 1 min. Make sure not to overdevelop.
Dry	Spin dry the wafer. Use the contaminated chuck for the spin dryer.
Inspection	Visually inspect the wafers and ensure photoresist coats the entire surface.
Hard baking	Bake at **80 deg. C for 16 min**. Use the **Memmert Oven**.

33. Wafer Dicing @Biosonics

Wafers should be diced using the **Disco Dicer (DAD3240).**
Die size 2x2 cm (50um less on each side but approx. 2x2cm)
Dice the Fused Silica wafers with the same blade as for glass.

Part 9: Mo etching

34. Photoresist removal @Polymer Lab

Carefully coat the dies in acetone for 3 min.
Then rinse 3 minutes with IPA and 3 minutes with DI water.
Allow the dies to air dry.

35. Inspection @100

Visually inspect the wafers through a microscope to check the openings and that all photoresist has been removed (and there are few to no residues).
If resist remains are found attempt removing them by carefully rubbing the surface with cotton bud soaked in IPA (step **30**).

36. Etching of Ti+pAl @Wet bench 10000

Make your own 0.55% HF bath in the CR 10000.
Perform a wet etching step using HF 0.55% for about 2.5 - 3min. (Etch until you can no longer see metal + 30 secs overetch)
Estimate the etching time with a dummy die before etching the real dies.
Rinse in DI water for 5min.

37. Inspection @100

Visually inspect the wafers through a microscope to check the metal pads and backside Ti have been removed.
If metal pads have not been fully removed, consider etching for a bit longer.
Mo tracks should be visible.

38. Mo Etching @ Wetbench 10000

Remove the Mo carefully (without creating large fluid movements).
Add one drop of Triton solution (1 drop in 0.5L of DI water) with a pipette on the electrode openings, and then cover the die surface with H_2O_2 (slowly one drop at a time with a pipette) and allow it to etch for about 2min.
Estimate the etching time with a dummy die before etching the real dies.
Rinse with DI water for 5 min (using a pipette to cover the surface and overflowing it repeatedly).

39. Inspection @100

Visually inspect the wafers through a microscope to check the Mo under the graphene in the electrode openings has been removed.
If metal residues are still present in the electrodes consider rinsing in DI water for a bit longer and if that does not work etch the Mo a bit more.
Mo under electrodes should not be visible, but Mo tracks should be visible! Over-etching of Mo will result in removal of Mo from the tracks, which is not desired.
Once result is satisfactory, allow to air dry for 24h.

40. Baking step

After air drying the dies for 24h, use the **Memmert Oven** to perform an extra baking step to ensure all water between the substrate and the graphene has evaporated.
Use the carrier for contaminated wafers.
Bake at 80C for 3h.

Part 10: Bond dies to PCBs

41. Bonding dies to PCBs @Biosonics Lab

Using superglue adhesive, bond the dies to the PCBs.
Set up the PCB on a rigid metal plate with a quartz wafer fragment in the center (so that the die is at the same height level as the PCB). Place the die to be adhered in the opening (in the correct direction), and bond it by adding a drop of superglue to each corner with the help of a needle.
Be careful not to cover any contact pads with superglue.
Once the adhesive has been added, move the metal plate with the parts, to a hot plate and cure at **80ºC for 15min.**

Use a protective metal plate over the hot plate to prevent superglue from curing on the hot plate. Consider placing a cleanroom tissue over the metal plate to absorb any superglue that drips down the edges and prevent the dies from adhering to the metal plate.

Part 11: Wire bonding to contact pads

42. Ball wirebonding dies to PCB @EWI building (HB14.320)

Ball wirebond Au wires between the die contact pads and the PCB contact pads using the **TPT HB05** Au bonder.

Part 12: Adding wells

43. Bonding wells to dies @Biosonics Lab

Using the epoxy **"EPO-TEK 301-2FL"** dye adhesive, bond the wells to the dies using the epoxy dispenser.
Be careful not to move the well when adding epoxy.
Set up the devices on a metal plate.
Coat the wire bonds with epoxy as well to protect them and prevent short circuits.
Move the metal plate to a hot plate and cure at **80ºC for 7h.**
Perform two rounds of epoxy coating; to prevent adding too much and to replace the epoxy lost due to leaking between the die and the PCB in the first round.

Consider using painting tape strips to keep the well in place (tape from side to side over the well in two directions).
Consider placing a cleanroom tissue over the metal plate to absorb any epoxy that drips down the PCB-die interface onto the metal plate and to prevent the device from adhering to the metal plate.
If epoxy falls on an incorrect area, be fast to remove. Complete removal by rubbing with IPA.

B

Script for Displaying Recorded Data From Amplifier

```
%File to analyse
file_analyse = 'pulse'; %Update name based on the file you want to analyse

%Ask wether or not to display graphs
gDisp = input('Display pulse map (p), graph display (g), or both (very
    slow) (b) ', 's');
if gDisp == 'p'
    gDisp = 1;
elseif gDisp == 'g'
    gDisp = 2;
elseif gDisp == 'b'
    gDisp = 3;
else
    gDisp = 0;
    errordlg('Character not recognised');
end

%extract the data and the range of values
data = extrct(file_analyse);

if gDisp == 1 || gDisp == 3
    %create figure and axes
    hFig = figure;
    hAx = axes;

    %set colormap
    colormap('turbo');

    %Initial Plot
    layot = data(:,:,1);
    layot(abs(layot)>=0) = 1;
    layot(isnan(layot)) = 0;
    hImage = imagesc(data(:,:,1), 'AlphaData', layot);
    colorbar;

    %Set title
    title('Electro-stimulation of MEA');
```

```
37
38      % Text annotation for trial index
39      hText = text(1.05, 0.98, sprintf('Trial: %d', 1), 'HorizontalAlignment
            ', 'left', 'VerticalAlignment', 'middle', 'Units', 'normalized', '
           FontSize', 12);
40  end
41
42  if gDisp == 1 || gDisp == 3
43      %Loop to update the plot for each trial
44      trialIdx = 1;
45      h = 1;
46      while ishandle(hFig) % Continue until the figure is closed
47
48          % Update the image data
49          set(hImage, 'CData', data(:,:,trialIdx));
50
51          % Set signal amplitude limits of the recorded signal
52          caxis([-1.706670000000000e+03, 1.705830000000000e+03]);
53
54          % Update trial index in text annotation
55          set(hText, 'String', sprintf('Trial: %d', trialIdx));
56
57          % Refresh the plot
58          drawnow;
59
60          % Create graph display
61          if gDisp == 3
62              if trialIdx == 500
63                  figure;
64                  tLayout = tiledlayout(8,8);
65                  AmpApp(data, trialIdx, tLayout);
66                  h = h + 1;
67              elseif trialIdx > 500
68                  if h == 10 % Update to adjust the step size.
69                      % The larger, the more data points will be added
70                      % in every iteration to the plots (faster progression)
71                      AmpApp(data, trialIdx, tLayout);
72                      h = 0;
73                  end
74                  h = h + 1;
75              end
76          end
77
78          % Pause between updates
79          pause(0.01);
80
81          % Move to the next trial (or start over if at the end)
82          trialIdx = mod(trialIdx, size(data, 3)) + 1;
83      end
84  end
85  if gDisp == 2
86      %Loop to update the plot for each trial
87      trialIdx = 500;
88      h = 1;
89      j = true;
90      while j == true % Continue until the figure is closed
```

```
91
92          % Create graph display
93          if trialIdx == 500
94              figure;
95              tLayout = tiledlayout(8,8);
96              AmpApp(data, trialIdx, tLayout);
97              h = h + 1;
98          elseif trialIdx > 500
99              if h == 10 % Update to adjust the step size.
100                 % The larger, the more data points will be added
101                 % in every iteration to the plots (faster progression)
102                 AmpApp(data, trialIdx, tLayout);
103                 h = 0;
104             end
105             h = h + 1;
106         end
107
108         % Pause between updates
109         pause(0.01);
110
111         % Move to the next trial (or start over if at the end)
112         trialIdx = mod(trialIdx, size(data, 3)) + 1;
113     end
114 end
115
116
117 %Extraction for files from amplifier: FM60-AMP Rev.B SerNo. 047, at LUMC
118 function out = extrct(file_analyse)
119 data = importdata([file_analyse, '.txt']);
120 out = NaN(8,8,length(data.data));
121 out(1,[2:7],:) = transpose(data.data(:,[2:7]));
122 out(2,:,:) = transpose(data.data(:,[8:15]));
123 out(3,:,:) = transpose(data.data(:,[16:23]));
124 out(4,:,:) = transpose(data.data(:,[24:31]));
125 out(5,[2:8],:) = transpose(data.data(:,[33:39]));
126 out(6,:,:) = transpose(data.data(:,[40:47]));
127 out(7,:,:) = transpose(data.data(:,[48:55]));
128 out(8,[2:7],:) = transpose(data.data(:,[56:61]));
129 end
130
131 %Plot and update function
132 function AmpApp(data, trial, tLayout)
133 t = (trial-499:1:trial);
134 i = 1;
135 for row = 1:8
136     for col = 1:8
137         if (row == 1 && col == 1) || (row == 1 && col == 8) || (row == 5
              && col == 1) || (row == 8 && col == 1) || (row == 8 && col ==
              8)
138             nexttile(tLayout,i);
139         else
140             nexttile(tLayout,i);
141             plot(t,squeeze(data(row,col,[trial-499:trial])*10^-3));
142             ylim([-1.71,1.71]);
143         end
144         i = i + 1;
```

```
145     end
146 end
147 end
```

Listing B.1: Script for displaying recorded data from amplifier. Enables visualisation of the data from all the electrodes in the MEA in the form of a colormap or plot.

C

Script for Calculating SNR From Recorded Data

```
1
2  %Files to assess:
3  rec_n = 'baseline';
4  rec_s = 'sine';
5  rec_ss = 's sine';
6  rec_vss = 'vs sine';
7  rec_p = 'pulse';
8  rec_sp = 's pulse';
9  rec_vsp = 'vs pulse';
10
11 %Load the data
12 data_n = extrct(rec_n);
13 data_s = extrct(rec_s);
14 data_ss = extrct(rec_ss);
15 data_vss = extrct(rec_vss);
16 data_p = extrct(rec_p);
17 data_sp = extrct(rec_sp);
18 data_vsp = extrct(rec_vsp);
19
20 %Call the electrode selector GUI
21 electrode_selector(data_n, data_s, data_ss, data_vss, data_p, data_sp,
       data_vsp);
22
23 %Ask for the name of the device
24 deviceName = input('Enter the name of the device: ', 's');
25
26 %Define the output directory
27 outputDir = fullfile(pwd, 'results');
28 if ~exist(outputDir, 'dir')
29     mkdir(outputDir);
30 end
31
32 %Save figures
33 figHandles = findall(groot, 'Type', 'figure');
34 figureNames = {'_SNR_elec', '_SNR_plots'};
35 for i = 1:length(figHandles)
36     filenameBase = [deviceName, figureNames{i}];
```

```
    saveas(figHandles(i), fullfile(outputDir, [filenameBase, '.png']));
    savefig(figHandles(i), fullfile(outputDir, [filenameBase, '.fig']));
end

%Save 'RMS_var' with multiple excel sheets
fieldsRMSvar = fieldnames(RMS_var);
filenameRMS = fullfile(outputDir, [deviceName, '_RMS_var.xlsx']);
for i = 1:length(fieldsRMSvar)
    arrayData = RMS_var.(fieldsRMSvar{i});
    arrayTable = array2table(arrayData);
    writetable(arrayTable, filenameRMS, 'Sheet', fieldsRMSvar{i});
end

%Save 'SNR_elec' with multiple excel sheets
fieldsSNRElec = fieldnames(SNR_elec);
filenameElec = fullfile(outputDir, [deviceName, '_SNR_elec.xlsx']);
for i = 1:length(fieldsSNRElec)
    arrayData = SNR_elec.(fieldsSNRElec{i});
    arrayTable = array2table(arrayData);
    writetable(arrayTable, filenameElec, 'Sheet', fieldsSNRElec{i});
end

%Save 'SNR_av' and 'SNR_dB' in their own single excel sheets
structsToSave = {'SNR_av', 'SNR_dB'};
for i = 1:length(structsToSave)
    structName = structsToSave{i};
    if exist(structName, 'var')
        structData = eval(structName);
        dataTable = struct2table(structData);
        filename = fullfile(outputDir, [deviceName, '_', structName, '.
            xlsx']);
        writetable(dataTable, filename);
    else
        warning(['Struct ', structName, ' does not exist.']);
    end
end

%Extraction for files from amplifier: FM60-AMP Rev.B SerNo. 047, at LUMC
function out = extrct(FileName)
fullFileName = [FileName, '.txt'];

%Check if the file exists
if ~exist(fullFileName, 'file')
    out = NaN(8,8,2000);
    return;
end

data = importdata(fullFileName);

%Check that the data field exists and has the expected size
if isfield(data, 'data') && size(data.data, 2) >= 61
    out = NaN(8,8,length(data.data));
    out(1,[2:7],:) = transpose(data.data(:,[2:7]));
    out(2,:,:) = transpose(data.data(:,[8:15]));
    out(3,:,:) = transpose(data.data(:,[16:23]));
    out(4,:,:) = transpose(data.data(:,[24:31]));
```

```
    out(5,[2:8],:) = transpose(data.data(:,[33:39]));
    out(6,:,:) = transpose(data.data(:,[40:47]));
    out(7,:,:) = transpose(data.data(:,[48:55]));
    out(8,[2:7],:) = transpose(data.data(:,[56:61]));
else
    out = NaN(8,8,10);
end
end

%Electrode Selector Function
function electrode_selector(dn, ds, dss, dvss, dp, dsp, dvsp)
%Create a figure window
f = figure('Name', 'Electrode Selector', 'NumberTitle', 'off');

%Initialize matrix to track selected electrodes
selected_electrodes = ones(8, 8); %1 means included, 0 means excluded
selected_electrodes([1, 8], [1, 8]) = 0; %Corners
selected_electrodes(5, 1) = 0; %First on the left in the 5th row
%Button size and spacing
buttonSize = 30; %Size of the buttons
spacing = 5; % Space between buttons

%Create 8x8 matrix of push buttons
for i = 1:8
    for j = 1:8
        %Skip buttons at specified locations
        if (i == 1 || i == 8) && (j == 1 || j == 8)
            continue;
        end
        if i == 5 && j == 1
            continue;
        end

        %Calculate position
        xPos = (j-1) * (buttonSize + spacing) + 10;
        yPos = (8-i) * (buttonSize + spacing) + 50;

        %Create button
        uicontrol('Style', 'pushbutton','String', '', ...
            'BackgroundColor', 'green', ...
            'Position', [xPos, yPos, buttonSize, buttonSize], ...
            'Callback', {@electrode_callback, i, j});
    end
end

%Add a button to start calculation
uicontrol('Style', 'pushbutton', ...
    'String', 'Calculate SNR', ...
    'Position', [10, 10, 150, 30], ...
    'Callback', @calculate_snr);

%Callback function for electrode selection
    function electrode_callback(src, ~, i, j)
        if selected_electrodes(i, j) == 1
            src.BackgroundColor = 'red';
            selected_electrodes(i, j) = 0;
```

```
148         else
149             src.BackgroundColor = 'green';
150             selected_electrodes(i, j) = 1;
151         end
152     end
153 
154 %Callback function for SNR calculation
155     function calculate_snr(~,~)
156         close(f); %Close the electrode selector window
157         %Calculate the RMS of all recordings
158         for k = 1:8
159             for l = 1:8
160                 if selected_electrodes(k,l) == 1
161                     RMS_n(k,l) = rms(dn(k,l,:));
162                     RMS_s(k,l) = rms(ds(k,l,:));
163                     RMS_ss(k,l) = rms(dss(k,l,:));
164                     RMS_vss(k,l) = rms(dvss(k,l,:));
165 
166                 elseif selected_electrodes(k,l) == 0
167                     RMS_n(k,l) = NaN;
168                     RMS_s(k,l) = NaN;
169                     RMS_ss(k,l) = NaN;
170                     RMS_vss(k,l) = NaN;
171                 end
172             end
173         end
174 
175         %Calculate peak RMS
176         %Declare variables to store collected data
177         RMS_p = [];
178         RMS_sp = [];
179         RMS_vsp = [];
180         %Boolean to check if peaks were assessed
181         AsP = false;
182         AsSP = false;
183         AsVSP = false;
184 
185         %Peak selection function
186         [RMS_p,AsP] = analysePeaks(dp, selected_electrodes);
187         [RMS_sp,AsSP] = analysePeaks(dsp, selected_electrodes);
188         [RMS_vsp,AsVSP] = analysePeaks(dvsp, selected_electrodes);
189 
190         %Create struct for RMS values
191         RMS_var = struct('noise', RMS_n, 'sine', RMS_s, 'small_sine',
                RMS_ss, 'very_small_sine', RMS_vss, 'pulse', RMS_p , '
                small_pulse', RMS_sp, 'very_small_pulse', RMS_vsp);
192 
193         %Calculate SNR for sine recordings
194         SNR_s = RMS_s./RMS_n;
195         SNR_ss = RMS_ss./RMS_n;
196         SNR_vss = RMS_vss./RMS_n;
197 
198         %Create struct for SNR values of electrodes
199         SNR_elec = struct('sine', SNR_s, 'small_sine', SNR_ss, '
                very_small_sine', SNR_vss);
200 
```

```
201         %Calculate average SNR for sine recordings
202         avSNR_s = sum(SNR_s(~isnan(SNR_s)))/sum(selected_electrodes(:));
203         avSNR_ss = sum(SNR_ss(~isnan(SNR_ss)))/sum(selected_electrodes(:))
                ;
204         avSNR_vss = sum(SNR_vss(~isnan(SNR_vss)))/sum(selected_electrodes
                (:));
205
206         %Create struct for average SNR values
207         SNR_av = struct('sine', avSNR_s, 'small_sine', avSNR_ss, '
                very_small_sine', avSNR_vss);
208
209         %Calculate dB of SNR for sine recordings
210         dB_SNR_s = 20*log10(avSNR_s);
211         dB_SNR_ss = 20*log10(avSNR_ss);
212         dB_SNR_vss = 20*log10(avSNR_vss);
213
214         %Create struct for dB SNR values
215         SNR_dB = struct('sine', dB_SNR_s, 'small_sine', dB_SNR_ss, '
                very_small_sine', dB_SNR_vss);
216
217         %Calculate SNR for pulse recordings if they were assessed
218         if AsP == true
219             SNR_p = RMS_p./RMS_n;
220             avSNR_p = sum(SNR_p(~isnan(SNR_p)))/sum(selected_electrodes(:)
                    );
221             dB_SNR_p = 20*log10(avSNR_p);
222             %Store values in structs
223             SNR_elec.pulse = SNR_p;
224             SNR_av.pulse = avSNR_p;
225             SNR_dB.pulse = dB_SNR_p;
226         else
227             SNR_p = NaN(8,8);
228             avSNR_p = 0;
229             dB_SNR_p = 0;
230         end
231         if AsSP == true
232             SNR_sp = RMS_sp./RMS_n;
233             avSNR_sp = sum(SNR_sp(~isnan(SNR_sp)))/sum(selected_electrodes
                    (:));
234             dB_SNR_sp = 20*log10(avSNR_sp);
235             %Store values in structs
236             SNR_elec.small_pulse = SNR_sp;
237             SNR_av.small_pulse = avSNR_sp;
238             SNR_dB.small_pulse = dB_SNR_sp;
239         else
240             SNR_sp = NaN(8,8);
241             avSNR_sp = 0;
242             dB_SNR_sp = 0;
243         end
244         if AsVSP == true
245             SNR_vsp = RMS_vsp./RMS_n;
246             avSNR_vsp = sum(SNR_vsp(~isnan(SNR_vsp)))/sum(
                    selected_electrodes(:));
247             dB_SNR_vsp = 20*log10(avSNR_vsp);
248             %Store values in structs
249             SNR_elec.very_small_pulse = SNR_vsp;
```

```
250             SNR_av.very_small_pulse = avSNR_vsp;
251             SNR_dB.very_small_pulse = dB_SNR_vsp;
252         else
253             SNR_vsp = NaN(8,8);
254             avSNR_vsp = 0;
255             dB_SNR_vsp = 0;
256         end
257 
258         %Assign variables to the base workspace
259         assignin('base', 'RMS_var', RMS_var);
260         assignin('base', 'SNR_elec', SNR_elec);
261         assignin('base', 'SNR_av', SNR_av);
262         assignin('base', 'SNR_dB', SNR_dB);
263 
264         %Display Individual Electrode SNRs
265         display_individual_snr(SNR_s, SNR_ss, SNR_vss, SNR_p, SNR_sp,
               SNR_vsp);
266 
267         %Display Bar Graphs
268         display_bar_graphs(avSNR_s, avSNR_ss, avSNR_vss, avSNR_p, avSNR_sp
               , avSNR_vsp, dB_SNR_s, dB_SNR_ss, dB_SNR_vss, dB_SNR_p,
               dB_SNR_sp, dB_SNR_vsp, SNR_s, SNR_ss, SNR_vss, SNR_p, SNR_sp,
               SNR_vsp);
269 
270     end
271 end
272 
273 function display_individual_snr(SNR_s, SNR_ss, SNR_vss, SNR_p, SNR_sp,
        SNR_vsp)
274 fig1 = figure;
275 ax1 = subplot(1,2,1);
276 hold(ax1, 'on');
277 
278 %Plotting dummy lines for legend
279 h1 = plot(ax1, NaN, NaN, 'b'); % Blue line for 'Sine 1V'
280 h2 = plot(ax1, NaN, NaN, 'Color', 'r'); % Red line for 'Sine 100mV'
281 h3 = plot(ax1, NaN, NaN, 'm'); % Magenta line for 'Sine 10mV'
282 
283 for i = 1:8
284     for j = 1:8
285         yPos = 9 - i;
286         %Draw squares and assign colors
287         if isnan(SNR_s(i,j))
288             rectangle(ax1, 'Position', [j-0.5, yPos-0.5, 1, 1], 'FaceColor
                    ', 'red');
289         else
290             rectangle(ax1, 'Position', [j-0.5, yPos-0.5, 1, 1], 'FaceColor
                    ', 'green');
291             text(j, yPos+0.3, num2str(SNR_s(i,j), '%.2f'), 'Color', 'b', '
                    HorizontalAlignment', 'center');
292             text(j, yPos, num2str(SNR_ss(i,j), '%.2f'), 'Color', 'r', '
                    HorizontalAlignment', 'center');
293             text(j, yPos-0.3, num2str(SNR_vss(i,j), '%.2f'), 'Color', 'm',
                     'HorizontalAlignment', 'center');
294         end
295     end
```

```
end

axis(ax1, [0.5 8.5 0.5 8.5]);
title(ax1, 'SNR for Each Electrode');

%Right subplot for Peak recordings
ax2 = subplot(1, 2, 2);
hold(ax2, 'on');

%Plotting dummy lines for legend
h4 = plot(ax2, NaN, NaN, 'k'); %Black line for 'Pulse 1V'
h5 = plot(ax2, NaN, NaN, 'y'); %Yellow line for 'Pulse 100mV'
h6 = plot(ax2, NaN, NaN, 'w'); %White line for 'Pulse 10mV'

%Plot for Peak recordings
for i = 8:-1:1
    for j = 1:8
        yPos = 9 - i;
        %Draw squares and assign colors
        if isnan(SNR_s(i,j))
            rectangle(ax2, 'Position', [j-0.5, yPos-0.5, 1, 1], 'FaceColor', 'red');
        else
            rectangle(ax2, 'Position', [j-0.5, yPos-0.5, 1, 1], 'FaceColor', 'green');
            text(j, yPos+0.3, num2str(SNR_p(i,j), '%.2f'), 'Color', 'k', 'HorizontalAlignment', 'center');
            text(j, yPos, num2str(SNR_sp(i,j), '%.2f'), 'Color', 'y', 'HorizontalAlignment', 'center');
            text(j, yPos-0.3, num2str(SNR_vsp(i,j), '%.2f'), 'Color', 'w', 'HorizontalAlignment', 'center');
        end
    end
end

axis(ax2, [0.5 8.5 0.5 8.5]);
title(ax2, 'SNR for Peak Electrodes');

%Custom legend
legend([h1, h2, h3, h4, h5, h6], {'Sine 1V', 'Sine 100mV', 'Sine 10mV', 'Pulse 1V', 'Pulse 100mV', 'Pulse 10mV'}, ...
    'Location', 'eastoutside', 'Orientation', 'vertical');
hold(ax1, 'off');
hold(ax2, 'off');
end

function display_bar_graphs(avSNR_s, avSNR_ss, avSNR_vss, avSNR_p, avSNR_sp, avSNR_vsp, dB_SNR_s, dB_SNR_ss, dB_SNR_vss, dB_SNR_p, dB_SNR_sp, dB_SNR_vsp, SNR_s, SNR_ss, SNR_vss, SNR_p, SNR_sp, SNR_vsp)
fig2 = figure;

%Top graph with error bars
ax2_1 = subplot(2,1,1);
barValues = [avSNR_s, avSNR_p, avSNR_ss, avSNR_sp, avSNR_vss, avSNR_vsp];
errorValues = [std(SNR_s(:), 'omitnan'), std(SNR_p(:), 'omitnan'), std(SNR_ss(:), 'omitnan'), std(SNR_sp(:), 'omitnan'), std(SNR_vss(:), '
```

```
    omitnan'), std(SNR_vsp(:), 'omitnan')];
bar(ax2_1, barValues);
hold(ax2_1, 'on');
errorbar(ax2_1, 1:6, barValues, errorValues, 'k', 'linestyle', 'none', '
    Color', 'red');
hold(ax2_1, 'off');
set(gca, 'xticklabel', {'Sine 1V', 'Pulse 1V', 'Sine 100mV', 'Pulse 100mV'
    , 'Sine 10mV', 'Pulse 10mV'});
ylabel('SNR');
title('Average SNR Values');

%Bottom graph for SNR in dB
ax2_2 = subplot(2,1,2);
bar(ax2_2, [dB_SNR_s, dB_SNR_p, dB_SNR_ss, dB_SNR_sp, dB_SNR_vss,
    dB_SNR_vsp]);
set(gca, 'xticklabel', {'Sine 1V', 'Pulse 1V', 'Sine 100mV', 'Pulse 100mV'
    , 'Sine 10mV', 'Pulse 10mV'});
ylabel('SNR dB');
title('Average SNR in dB');
end

function [RMS_data, wasAssessed] = analysePeaks(data, selected_electrodes)
%Initialize output variables
RMS_data = [];  %This will store the matrix to be returned
wasAssessed = false; %Boolean to indicate if 'Assess' button was clicked
selectedElectrodesMatrix = zeros(8, 8);  %This will store the selected
    electrodes

%Create figure for plots
f1 = figure('Name', 'Electrode Data Plots', 'NumberTitle', 'off', '
    Position', [100, 100, 600, 800]);

%Left side: 8x8 matrix of plots
t = 1:1:1999;
for i = 1:8
    for j = 1:8
        if selected_electrodes(i, j) == 1
            %Calculate position for each subplot
            subplotIdx = (i-1)*8 + j;
            subplot(8, 8, subplotIdx);
            pl = data(i,j,[1:1999]);
            plot(t,pl(:));
        end
    end
end

%Initialize a matrix to keep track of selected electrodes for peak
    analysis
peak_selected_electrodes = ones(8, 8); %1 means included initially
peak_selected_electrodes([1, 8], [1, 8]) = 0; %Modify this to exclude
    certain electrodes
peak_selected_electrodes(5, 1) = 0;
peak_selected_electrodes = peak_selected_electrodes & selected_electrodes;
    %Apply previous selections

%Create separate figure for electrode selection
```

```
f2 = figure('Name', 'Electrode Selection for Peak Analysis - Pick ONLY 3', 'NumberTitle', ...
    'off', 'Position', [720, 100, 480, 800], 'WindowStyle', 'modal');


%Right side: Electrode selection for peak analysis
for i = 1:8
    for j = 1:8
        if selected_electrodes(i, j) == 1
            %Calculate position for each button
            xPos = (mod(j-1, 8) * 60) + 10;
            yPos = (800 - i * 60) - 30;
            uicontrol('Style', 'pushbutton', ...
                'String', '', ...
                'BackgroundColor', 'red', ...
                'Position', [xPos, yPos, 50, 50], ...
                'Callback', {@peakSelectCallback, i, j});
        end
    end
end

uicontrol(f2, 'Style', 'pushbutton', 'String', 'Skip Step', 'Position', ...
    [20, 20, 100, 30], 'Callback', @skipStep);
uicontrol(f2, 'Style', 'pushbutton', 'String', 'Assess', 'Position', ...
    [140, 20, 100, 30], 'Callback', @assessPeaks);

%Pause execution of the function until UI interaction
uiwait(f2);

    function peakSelectCallback(src, ~, i, j)
        if peak_selected_electrodes(i, j) == 1
            src.BackgroundColor = 'green';
            peak_selected_electrodes(i, j) = 0;
            selectedElectrodesMatrix(i, j) = 1;  %Update selected electrodes matrix
        else
            src.BackgroundColor = 'red';
            peak_selected_electrodes(i, j) = 1;
            selectedElectrodesMatrix(i, j) = 0;  %Update selected electrodes matrix
        end
    end

    function skipStep(~, ~)
        %Assign empty data or handle skip logic
        RMS_data = NaN(8,8);
        wasAssessed = false; %Indicate that 'Skip' was clicked
        resumeExecution();
    end

    function assessPeaks(~, ~)
        %Assign the result to outputMatrix
        RMS_data = peak_assess(data, selected_electrodes, selectedElectrodesMatrix); %Call the peak assessment function
        wasAssessed = true; %Indicate that 'Assess' was clicked
```

```
440         resumeExecution();
441     end
442     function resumeExecution()
443         uiresume(f2); %Resume execution of the function
444         close(f1); %Close the plot figure
445         close(f2); %Close the selection figure
446     end
447 end
448 
449 function RMS_data = peak_assess(data, selected_electrodes,
        selectedElectrodesMatrix)
450 
451 %Put selected electrode data into row format
452 
453 FindPeakData = [];
454 counter = 0;
455 
456 %Determine the length of the recordings
457 dataLength = size(data, 3); %The third dimension is the length of the
        recordings
458 
459 %Initialize peakIndicatorArray with zeros
460 peakIndicatorArray = zeros(1, dataLength);
461 
462 %Flag to check if 'Submit' has been pressed
463 isSubmitted = false;
464 
465 
466 for i = 1:8
467     for j = 1:8
468         if selectedElectrodesMatrix(i,j) == 1
469             counter = counter + 1;
470             Temp_elecData = data(i,j,:);
471             FindPeakData(counter,:) = Temp_elecData(:)';
472         end
473     end
474 end
475 
476 %Electrodes for manual peak selection
477 electrode1 = FindPeakData(1,:);
478 electrode2 = FindPeakData(2,:);
479 electrode3 = FindPeakData(3,:);
480 
481 %Determine the length of the recordings
482 dataLength = size(electrode1, 2); %Assuming all electrodes have the same
        length
483 
484 %Create a figure
485 f = figure;
486 
487 %Create subplots for the three electrodes
488 ax1 = subplot(3,1,1);
489 plot(1:dataLength, electrode1);
490 title('Electrode 1');
491 
492 ax2 = subplot(3,1,2);
```

```
493 plot(1:dataLength, electrode2);
494 title('Electrode 2');
495
496 ax3 = subplot(3,1,3);
497 plot(1:dataLength, electrode3);
498 title('Electrode 3');
499
500 %Shared variables
501 clicks = 0;
502 times = [];
503 lines = [];
504 autofillEnabled = true;
505 suggestedTimes = [];
506 suggestedLines = [];
507
508 %Set up the callback
509 set(f, 'WindowButtonDownFcn', @mouse_click);
510
511 %Function to update the GUI elements
512     function update_gui()
513         %Add or remove the submit button based on number of clicks
514         if mod(clicks, 2) == 0 && clicks > 0
515             uicontrol('Style', 'pushbutton', 'String', 'Submit',...
516                 'Position', [20 60 100 20],...
517                 'Callback', @submit_selection);
518         else
519             delete(findobj(f, 'String', 'Submit'));
520         end
521
522         %Add the back button
523         uicontrol('Style', 'pushbutton', 'String', 'Back',...
524             'Position', [20 40 100 20],...
525             'Callback', @back_selection);
526
527         %Toggle auto-fill button
528         if autofillEnabled
529             uicontrol('Style', 'pushbutton', 'String', 'Deactivate Auto-
                fill',...
530                 'Position', [20 20 100 20],...
531                 'Callback', @toggle_autofill);
532         else
533             uicontrol('Style', 'pushbutton', 'String', 'Activate Auto-fill
                ',...
534                 'Position', [20 20 100 20],...
535                 'Callback', @toggle_autofill);
536         end
537
538         %Auto-fill accept/reject buttons
539         if ~isempty(suggestedTimes)
540             uicontrol('Style', 'pushbutton', 'String', 'Accept Auto-fill'
                ,...
541                 'Position', [130 40 100 20],...
542                 'Callback', @accept_autofill);
543
544             uicontrol('Style', 'pushbutton', 'String', 'Reject Auto-fill'
                ,...
```

```
                'Position', [130 20 100 20],...
                'Callback', @reject_autofill);
        end
    end

%Callback function for mouse click
    function mouse_click(~, ~)
        clicks = clicks + 1;
        cp = get(gca, 'CurrentPoint');
        x = round(cp(1,1));
        x = max(1, min(x, dataLength)); %Ensure x is within the data range
        times = [times, x];
        lines(end+1) = line([x x], ylim, 'Color', 'red', 'Parent', ax1);
        lines(end+1) = line([x x], ylim, 'Color', 'red', 'Parent', ax2);
        lines(end+1) = line([x x], ylim, 'Color', 'red', 'Parent', ax3);

        %Auto-fill suggestion
        if autofillEnabled && mod(clicks, 2) == 0
            suggestedTimes = [times(end-1) + 1000, times(end) + 1000];
            %Ensure suggested times are within the data range
            suggestedTimes = min(suggestedTimes, dataLength);

            suggestedLines(end+1) = line([suggestedTimes(1) suggestedTimes
                (1)], ylim, 'Color', 'green', 'Parent', ax1);
            suggestedLines(end+1) = line([suggestedTimes(1) suggestedTimes
                (1)], ylim, 'Color', 'green', 'Parent', ax2);
            suggestedLines(end+1) = line([suggestedTimes(1) suggestedTimes
                (1)], ylim, 'Color', 'green', 'Parent', ax3);
            suggestedLines(end+1) = line([suggestedTimes(2) suggestedTimes
                (2)], ylim, 'Color', 'green', 'Parent', ax1);
            suggestedLines(end+1) = line([suggestedTimes(2) suggestedTimes
                (2)], ylim, 'Color', 'green', 'Parent', ax2);
            suggestedLines(end+1) = line([suggestedTimes(2) suggestedTimes
                (2)], ylim, 'Color', 'green', 'Parent', ax3);
        end

        update_gui();
    end

%Callback function for the back button
    function back_selection(~, ~)
        if clicks > 0
            clicks = clicks - 1;
            %Remove the last time and the last set of red lines
            times(end) = [];
            delete(lines(end-2:end));
            lines(end-2:end) = [];

            %Remove any existing auto-fill suggestions
            delete(suggestedLines);
            suggestedLines = [];
            suggestedTimes = [];

            %If we have an even number of clicks, create a new auto-fill
                suggestion
            if autofillEnabled && mod(clicks, 2) == 0 && clicks >= 2
```

```
                suggestedTimes = [times(end-1) + 1000, times(end) + 1000];
                %Ensure suggested times are within the data range
                suggestedTimes = min(suggestedTimes, dataLength);
                suggestedLines(end+1) = line([suggestedTimes(1)
                    suggestedTimes(1)], ylim, 'Color', 'green', 'Parent',
                    ax1);
                suggestedLines(end+1) = line([suggestedTimes(1)
                    suggestedTimes(1)], ylim, 'Color', 'green', 'Parent',
                    ax2);
                suggestedLines(end+1) = line([suggestedTimes(1)
                    suggestedTimes(1)], ylim, 'Color', 'green', 'Parent',
                    ax3);
                suggestedLines(end+1) = line([suggestedTimes(2)
                    suggestedTimes(2)], ylim, 'Color', 'green', 'Parent',
                    ax1);
                suggestedLines(end+1) = line([suggestedTimes(2)
                    suggestedTimes(2)], ylim, 'Color', 'green', 'Parent',
                    ax2);
                suggestedLines(end+1) = line([suggestedTimes(2)
                    suggestedTimes(2)], ylim, 'Color', 'green', 'Parent',
                    ax3);
            end
        end
        update_gui();
    end

%Callback function for submit button
    function submit_selection(~, ~)
        %Reset peakIndicatorArray to all zeros
        peakIndicatorArray(:) = 0;

        %Loop through each selected region and set values to 1s
        for k = 1:2:length(times)
            startIdx = times(k);
            endIdx = times(k+1);
            peakIndicatorArray(startIdx:endIdx) = 1;
        end

        %Set the flag to true
        isSubmitted = true;

        %Close the figure
        close(f);
    end

%Wait for the 'Submit' button to be pressed
while ~isSubmitted
    pause(1); %Pause for a short while to prevent overwhelming the CPU
end

%Callback function to toggle auto-fill feature
    function toggle_autofill(~, ~)
        autofillEnabled = ~autofillEnabled;

        %Clear any existing auto-fill suggestions
        delete(suggestedLines);
```

```
638         suggestedLines = [];
639         suggestedTimes = [];
640 
641         %Generate new auto-fill suggestion if enabled and an even number
                of points are selected
642         if autofillEnabled && mod(clicks, 2) == 0 && clicks >= 2
643             suggestedTimes = [times(end-1) + 1000, times(end) + 1000];
644             %Ensure suggested times are within the data range
645             suggestedTimes = min(suggestedTimes, dataLength);
646             suggestedLines(end+1) = line([suggestedTimes(1) suggestedTimes
                    (1)], ylim, 'Color', 'green', 'Parent', ax1);
647             suggestedLines(end+1) = line([suggestedTimes(1) suggestedTimes
                    (1)], ylim, 'Color', 'green', 'Parent', ax2);
648             suggestedLines(end+1) = line([suggestedTimes(1) suggestedTimes
                    (1)], ylim, 'Color', 'green', 'Parent', ax3);
649             suggestedLines(end+1) = line([suggestedTimes(2) suggestedTimes
                    (2)], ylim, 'Color', 'green', 'Parent', ax1);
650             suggestedLines(end+1) = line([suggestedTimes(2) suggestedTimes
                    (2)], ylim, 'Color', 'green', 'Parent', ax2);
651             suggestedLines(end+1) = line([suggestedTimes(2) suggestedTimes
                    (2)], ylim, 'Color', 'green', 'Parent', ax3);
652         end
653 
654         update_gui();
655     end
656 
657 
658 %Callback function to accept auto-fill suggestion
659     function accept_autofill(~, ~)
660         %Add suggested times to the selected times and increment clicks
661         times = [times, suggestedTimes];
662         clicks = clicks + 2;
663 
664         %Replace green lines with red lines
665         delete(suggestedLines);
666         lines(end+1) = line([suggestedTimes(1) suggestedTimes(1)], ylim, '
                Color', 'red', 'Parent', ax1);
667         lines(end+1) = line([suggestedTimes(1) suggestedTimes(1)], ylim, '
                Color', 'red', 'Parent', ax2);
668         lines(end+1) = line([suggestedTimes(1) suggestedTimes(1)], ylim, '
                Color', 'red', 'Parent', ax3);
669         lines(end+1) = line([suggestedTimes(2) suggestedTimes(2)], ylim, '
                Color', 'red', 'Parent', ax1);
670         lines(end+1) = line([suggestedTimes(2) suggestedTimes(2)], ylim, '
                Color', 'red', 'Parent', ax2);
671         lines(end+1) = line([suggestedTimes(2) suggestedTimes(2)], ylim, '
                Color', 'red', 'Parent', ax3);
672 
673         %Clear current suggested times and lines
674         suggestedTimes = [];
675         suggestedLines = [];
676 
677         %Generate new auto-fill suggestion if enabled
678         if autofillEnabled && clicks >= 2
679             suggestedTimes = [times(end-1) + 1000, times(end) + 1000];
680             %Ensure suggested times are within the data range
```

```
681             suggestedTimes = min(suggestedTimes, dataLength);
682             suggestedLines(end+1) = line([suggestedTimes(1) suggestedTimes
                    (1)], ylim, 'Color', 'green', 'Parent', ax1);
683             suggestedLines(end+1) = line([suggestedTimes(1) suggestedTimes
                    (1)], ylim, 'Color', 'green', 'Parent', ax2);
684             suggestedLines(end+1) = line([suggestedTimes(1) suggestedTimes
                    (1)], ylim, 'Color', 'green', 'Parent', ax3);
685             suggestedLines(end+1) = line([suggestedTimes(2) suggestedTimes
                    (2)], ylim, 'Color', 'green', 'Parent', ax1);
686             suggestedLines(end+1) = line([suggestedTimes(2) suggestedTimes
                    (2)], ylim, 'Color', 'green', 'Parent', ax2);
687             suggestedLines(end+1) = line([suggestedTimes(2) suggestedTimes
                    (2)], ylim, 'Color', 'green', 'Parent', ax3);
688         end
689
690         update_gui();
691     end
692
693
694 %Callback function to reject auto-fill suggestion
695     function reject_autofill(~, ~)
696         delete(suggestedLines);
697         suggestedLines = [];
698         suggestedTimes = [];
699         update_gui();
700     end
701
702 %Calculate RMS of every every electrode in analysis
703 for i = 1:8
704     for j = 1:8
705         if selected_electrodes(i,j) == 1
706             temp_data = data(i,j,:);
707             temp_data = temp_data(:)';
708             RMS_data(i,j) = AvPeakRMS(peakIndicatorArray,temp_data);
709         elseif selected_electrodes(i,j) == 0
710             RMS_data(i,j) = NaN;
711         end
712     end
713 end
714
715     function finalRMS = AvPeakRMS(dataPeaks, data)
716         n = length(dataPeaks);
717         starts = [];
718         ends = [];
719         storeRMS = []; %Initialize storeRMS as an empty array
720
721         %Find start and end indices of non-zero sections
722         g = 2;  %Start from second element to ensure sections are
                surrounded by zeros
723         while g < n  %Go up to the second-to-last element
724             if dataPeaks(g) ~= 0 && dataPeaks(g-1) == 0
725                 startIdx = g;
726                 endIdx = find(dataPeaks(g:end) == 0, 1, 'first') + g - 2;
727                 if ~isempty(endIdx) && dataPeaks(endIdx + 1) == 0
728                     starts = [starts, startIdx];
729                     ends = [ends, endIdx];
```

```
730                     g = endIdx;
731                 end
732             end
733             g = g + 1;
734         end
735 
736         %Extract sections and store in matrix
737         numSections = length(starts);
738 
739         for g = 1:numSections
740             storeRMS(g) = rms(data(starts(g):ends(g)));
741         end
742 
743         %Calculate average RMS for all the peaks
744         finalRMS = mean(storeRMS);
745     end
746 
747 end
```

Listing C.1: Script for calculating SNR from recorded data. The code enables the user to select the electrodes to be included in the calculation. The user will be prompted to manually select the events of the square waveform stimulation recordings. The analysed data will be displayed in a matrix, representing the value of each electrode, and as a bar plot with the average SNR for each stimulation used. Lastly, the analysed data and displayed figures will be saved as excel and png files.